**Abstract** Over the past three decades a new spectroscopic technique with unique possibilities has emerged. Based on coherent and time-resolved detection of the electric field of ultrashort radiation bursts in the far-infrared, this technique has become known as terahertz time-domain spectroscopy (THz-TDS). In this review article the authors describe the technique in its various implementations for static and time-resolved spectroscopy, and illustrate the performance of the technique with recent examples from solid-state physics and physical chemistry as well as aqueous chemistry. Examples from other fields of research, where THz spectroscopic techniques have proven to be useful research tools, and the potential for industrial applications of THz spectroscopic and imaging techniques are discussed.
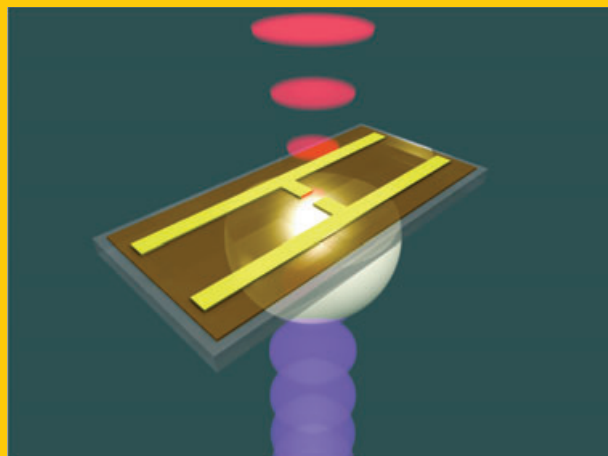
Terahertz spectroscopy and imaging – Modern techniques and applications

Peter Uhd Jepsen[1,*] **, David G. Cooke**[1] **, and Martin Koch**[2]

1. Introduction

The far-infrared, or terahertz (THz) region of the electromagnetic spectrum hosts a wealth of intriguing and highly complex interactions between radiation and matter in physical, chemical and biological systems. With photon energies in the millielectronvolt (meV) range, electromagnetic radiation at THz frequencies interacts strongly with systems that have characteristic lifetimes in the picosecond range and energetic transitions in the meV range. Examples of such systems include bound electrical charges [1], free charge plasmas [2–4], strongly confined charge plasma [5], excitons [6–9], transient molecular dipoles [10], phonons in crystalline solids [11], weakly bonded molecular crystals [12–15], relaxational dynamics in aqueous liquids [16–18], and hydrated biological matter [19–21].

Furthermore, THz spectroscopy allows for the characterization of THz devices including modulators [22–26], filters [27, 28], dielectric mirrors [26, 29–32] and waveguides [33–37] and artificial THz materials such as photonic crystals [38–42] as well as metamaterials [43, 44]. Therefore, it may not be surprising that a technology that can detect the amplitude and phase of coherently generated electromagnetic radiation in the THz range is an invaluable spectroscopic tool for research in physics, chemistry and biology.

In addition, numerous practical applications for optoelectronic THz systems are presently discussed, ranging from medical diagnostics and security applications to industrial control processes. In these application fields THz imaging techniques stand at the focus of current interest. Nevertheless, one can identify applications where single-point measurements provide sufficient information.

The THz frequency range corresponds loosely to photon energies between 1 and 100 meV. Therefore, low-energy interactions in a wide range of materials can be studied with spectroscopy in the THz range. Spectroscopy in the far-infrared has been pursued since it became technically feasible in the 1950s with the development of Fourier transform infrared (FTIR) spectroscopy. FTIR spectroscopy was described in an early review by Loewenstein [45], containing a discussion of both the technique and the history of its development. A detailed discussion of FTIR spectroscopy was also included in the textbook by Möller and Rothschild in 1971 [46].

The development of the femtosecond laser in the 1980s enabled an alternative method for spectroscopy in the THz range, with completely new functionalities. This method, which was first described in 1989 by Grischkowsky et al. [47], relies on the optical excitation of photoconductive dipole antennas and is now known as terahertz time-domain spectroscopy (THz-TDS). The subsequent development of THz-TDS has been closely linked to the more general development of ultrafast laser technology, most notably the development of the Ti:sapphire femtosecond laser [48]. At the same time, the principles behind THz-TDS are heav-

[1] DTU Fotonik – Department of Photonics Engineering, Technical University of Denmark, 2800 Kongens Lyngby, Denmark
[2] Fachbereich Physik, Philipps-Universität Marburg, Renthof 5, 35032 Marburg, Germany
* Corresponding author: puje@fotonik.dtu.dk

ily related to microwave technology as well as methods developed for FTIR.

Alternatively, photoconductive antennas can be driven by the emission of two independent single-color lasers [49–52] or a single two-color laser [53–56]. In this case, the photoconductive structures are referred to as photomixers and emit continuous-wave (cw) radiation with a frequency determined by the difference frequency between the laser lines. THz radiation can be detected either by slow thermal detectors [53, 57] or coherently, using a second photomixer [51, 54, 58]. Only the latter room-temperature scheme is fast enough for many practical applications.

Recently, an intermediate technique that bridges THz-TDS and photomixing setups was introduced. It is based on multimode semiconductor laser diodes (MMSLDs) with which the Hangyo group did pioneering work already ten years ago [59–61]. Recently, however, it was pointed out that if MMSLDs with equidistant frequency spacing of the emitted modes are used to operate a photomixing setup, periodic pulse-like THz signals are obtained [62]. Hence, this cost-efficient excitation scheme leads to waveforms that are similar to those in a THz-TDS setup and exhibit high signal-to-noise ratios. Consequently, all data-extraction schemes developed for THz-TDS can be applied.

In this review we will discuss THz-TDS and give selected examples of its widespread applications. In Sect. 2.1 we will discuss the widely used photoconductive method for generation and detection of pulsed, broadband, coherent light in the THz region. Section 2.2 describes the complementary method for photoconductive generation and detection of continuous-wave THz radiation, tunable across the low-THz region. Finally, Sect. 2.3 discusses methods based on frequency conversion in nonlinear crystals for the generation and detection of broadband THz signals.

In Sect. 3 we will discuss THz-TDS systems, with a focus on its basic implementations in transmission and reflection modes, and briefly discuss other implementations such as attenuated total internal reflection spectroscopy, and recent developments in waveguide spectroscopy. In connection with the different experimental techniques we will discuss the application of THz-TDS for investigations of solid-state materials and liquids.

Section 4 discusses methods for time-resolved THz-TDS, outlining the experimental apparatus and considerations in Sect. 4.1 and data acquisition and analysis in Sect. 4.2. The classic standard for a time-resolved THz-TDS measurement, photoconductivity of bulk gallium arsenide, is discussed in Sect. 4.3 to illustrate the power of the technique in determining ultrafast transport parameters. We give recent examples of THz-TDS on solid-state and liquid systems, with examples from static spectroscopy on solid-state materials in Sect. 5.1 and on liquids in Sect. 5.2 and examples from time-resolved THz-TDS of semiconductor nanostructures in Sects. 5.3 and 5.4.

THz radiation will, because of its long wavelength, penetrate many materials such as clothing, packing materials, and certain construction materials. Therefore, there is significant interest in the development of imaging methods that can combine this 'see-through' capability with the spectroscopic

information that materials such as explosives, pharmaceutical, and narcotic materials contains in the THz range. In Sect. 6 we will review the recent development in application of THz spectroscopic and imaging techniques in other areas of science, for example art conservation, and discuss the applicability of THz sensing in contact-free inspection in security applications, in the polymer industry, and in the food industry.

Finally, we will conclude the review with our view on future trends of optoelectronic THz technology.

2. Generation and detection of broadband THz radiation

Broadband, coherent THz radiation can be generated in a photoconductive switch on a semiconductor substrate excited by a femtosecond laser pulse or in an electrooptic crystal by difference-frequency mixing of the frequency components of a femtosecond laser pulse. Generally speaking, the several THz bandwidth of a femtosecond laser pulse can be used for the generation of broadband THz radiation with comparable bandwidth.

When driven by a train of femtosecond laser pulses synchronized to the laser pulses used for THz generation, photoconductive switches and electrooptic crystals can also be used for a field-resolved detection of the THz field.

2.1. Photoconductive broadband THz generation and detection

The electric field from a electric dipole oscillating at a frequency $\nu = \omega/2\pi$ can be expressed as [63]

$$E = \tag{1}$$

$$\frac{1}{4\pi\varepsilon_0}\left[k^2(\vec{n}\times\vec{p})\times\vec{n}\frac{\mathrm{e}^{\mathrm{i}kr}}{r} + [3\vec{n}(\vec{n}\cdot\vec{p}) - \vec{p}]\left(\frac{1}{r^3} - \frac{\mathrm{i}k}{r^2}\right)\mathrm{e}^{\mathrm{i}kr}\right],$$

where $\vec{p} = \int\rho(\vec{x})\vec{x}\,\mathrm{d}V$ is the electric dipole moment, $\vec{n}$ is the unit vector in the direction of observation, r is the distance between the dipole and the observation point, and $k = \omega/c$ is the propagation constant of the electric field in free space.

If we assume that the temporal evolution of the electric dipole moment can be found by a Fourier analysis of its frequency components then the electric field component perpendicular to the direction of observation from an electric dipole can be expressed in the time domain in the following form by a Fourier transformation of Eq. (1),

$$E_\theta(\mathrm{r},\theta,t) = \frac{1}{4\pi\varepsilon_0}\left[\frac{1}{r^3}\vec{p}(t_\mathrm{r}) + \frac{1}{cr^2}\dot{\vec{p}}(t_\mathrm{r}) + \frac{1}{c^2r}\ddot{\vec{p}}(t_\mathrm{r})\right]\sin\theta, \tag{2}$$

where θ is the angle between the electric dipole moment vector and the direction of observation and $t_\mathrm{r} = t - r/c$ is the retarded time. In the far field ($r \gg \lambda \gg d$, where d is the size of the electric dipole) only the last term in Eq. (2) survives, and hence the radiated electric field is proportional
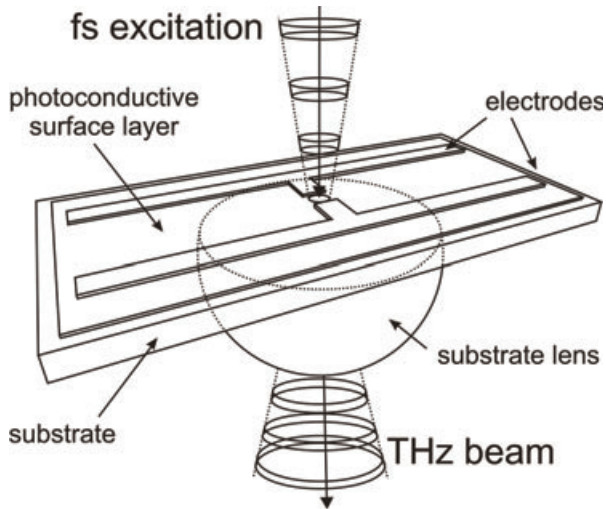
Figure 1 Photoconductive switch for generation of ultrashort THz transients that are collimated into a free-space beam by a substrate lens attached to the antenna structure.

to the second temporal derivative of the dipole moment, or, the first temporal derivative of the current density $j(t)$.

This fundamental principle can be exploited for the generation of ultrabroadband electromagnetic transients with frequencies in the THz range. The frequency content of the electromagnetic field is closely linked to the dynamics of the transient current that generated the field. Consequently, a current transient that evolves on the time scale of a few hundred femtoseconds to a few picoseconds will generate a characteristic radiation signature with frequencies in the terahertz range.

Such ultrafast current impulses can be generated by impinging an ultrafast laser pulse onto a biased semiconductor surface. Photons with sufficiently high energy can excite electrons across the electronic bandgap of the semiconductor into the conduction band, and the bias field then accelerates the free charges that finally recombine with the characteristic recombination time of the material. Using femtosecond laser pulses, current impulses with bandwidths well into the THz range can be generated in this manner. A photoconductive switch for generation of ultrashort THz pulses is illustrated in Fig. 1.

The metallic electrodes supply the bias field to the photoconductive gap between the electrodes. This gap is excited by femtosecond laser pulses, and the resulting current transients generate the THz pulses that are emitted into the substrate by a THz dipole antenna structure, which in the simplest case is formed by the metallized bridge between the two electrodes. The THz radiation is collected into a collimated beam by a substrate lens attached to the structure.

A simple one-dimensional set of rate equations based on the phenomenological Drude model is able to describe the main features of the motion of charges during and after photoexcitation of a biased semiconductor [64], and here we briefly discuss this model.

For simplicity, we assume that electrons near the bottom of the conduction band of the semiconductor material are the

main contributors to the kinetics, due to their low effective mass compared to that of the holes. For a given density n_f of free electrons, the current density is given by

$$\theta\, j(t) = -en_f(t)v(t)\,, \tag{3}$$

where $v(t)$ is the velocity of the electrons. With a capture time τ_c of the electrons into for instance mid-bandgap trap sites, and a generation rate $G(t)$ due to optical excitation, the creation rate of the electrons can be expressed as

$$\frac{dn_f}{dt} = -\frac{n_f}{\tau_c} + G(t)\,. \tag{4}$$

The velocity of the electrons is damped by scattering processes, in the Drude picture described by a single characteristic scattering time τ_s, and increased by the local electric field strength E_{loc},

$$\frac{dv}{dt} = -\frac{v}{\tau_s} + \frac{e}{m^*}E_{loc}\,. \tag{5}$$

The local bias field is determined by the external, static bias field E_{bias} and the screening field set up by the polarization P_{sc} of electrons and holes by the electric field,

$$E_{loc}(t) = E_{bias} - \frac{P_{sc}(t)}{\eta\varepsilon}\,, \tag{6}$$

where η is a phenomenological screening factor and ε is the permittivity of the semiconductor material. The strength of the applied bias field influences both the amplitude and the temporal profile of the generated THz transient. In a photoconductive switch the bias field is enhanced significantly near the positive electrode [65]. Hence, tightly focused excitation near the positive electrode results in a stronger and faster THz transient than excitation with the same power over a larger region of the photoconductive gap.

The kinetics of the polarization field is given by

$$\frac{dP_{sc}}{dt} = -\frac{P_{sc}}{\tau_r} + j(t)\,. \tag{7}$$

Solving this set of first-order differential equations to find the kinetics of $j(t)$ allows us to calculate the shape of the generated THz transient,

$$E_{THz}(t) \propto \frac{d\,j(t)}{dt}\,. \tag{8}$$

In spite of its simplicity this model predicts many of the observed features of THz transients generated by femtosecond optical excitation of a photoconductive switch, as illustrated in Fig. 2, where panel (a) shows the calculated THz transients, panel (b) shows the dynamics of the screening of the local bias field E_{loc} owing to the spatial separation of the photoexcited charges, and panel (c) shows the corresponding amplitude spectra for the two excitation intensities 10^{17} cm^{-3} (blue curves) and 10^{18} cm^{-3} (red curves).

This simulation was carried out using an excitation pulse width of 100 fs, a trapping time $\tau_c = 1$ ps, a scattering time
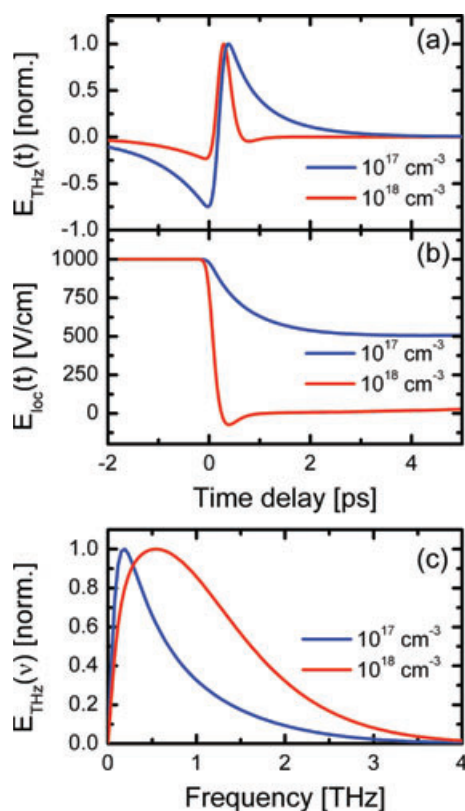
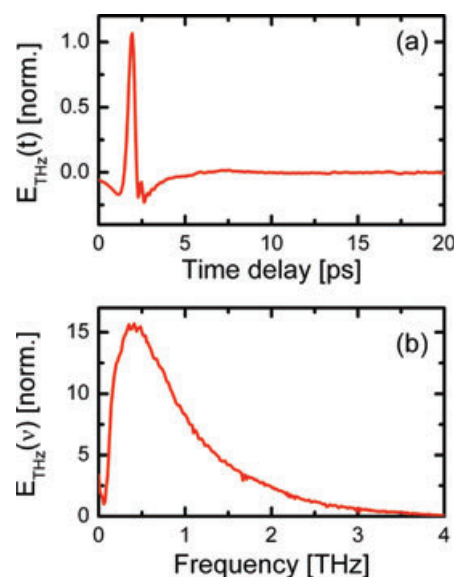**Figure 2** (online color at: www.lpr-journal.org) (a) Simulated THz pulse shapes, (b) dynamics of the local electric field, and (c) frequency spectra of the pulses at excitation levels 10^{17} cm^{-3} (blue curves) and 10^{18} cm^{-3} (red curves).

$\tau_{\mathrm{s}} = 0.1$ ps, and a recombination time $\tau_{\mathrm{r}} = 100$ ps, representative of semiconductor materials with ultrafast trapping times, and an effective electron mass $m^* = 0.067 m_e$, representative of conduction band electrons in gallium arsenide.

The intensity-dependent temporal evolution of the local electric field plays a central role for the shape of the generated THz transient. At low excitation intensities the bias field is only slightly screened by the polarization field, whereas at high intensities the bias field can be screened completely on a subpicosecond time scale, resulting in an equally fast deceleration of the electrons. This effect is responsible for the intensity dependence of the generated THz pulse shape, and is seen as an increase in the bandwidth of the THz transient in Fig. 2 at high excitation intensities. The ultrafast screening has been measured directly in a photoconductive switch [66].

The screening process can take place on a subpicosecond time scale, and thus it can strongly influence the acceleration of photogenerated charges. Recent Monte Carlo simulations [67, 68] have confirmed this phenomenological model, and additionally provided a deeper insight into the underlying dynamics of the photoexcited carriers in the conduction band of the semiconductor during the THz generation process.

Figure 3a shows a measurement of a THz transient generated in a low-temperature-grown gallium arsenide antenna.

Figure 3 (online color at: www.lpr-journal.org) (a) THz-bandwidth transient recorded in the time domain and (b) its corresponding amplitude spectrum.

The THz signal generated by the transient current in a biased semiconductor is coupled into free space by integrating the photoconductive region in a suitable antenna structure. For efficient coupling of broadband THz radiation into free space, a simple dipole structure like the one shown in Fig. 1 is rather efficient and straightforward to fabricate using standard UV lithography. It should be noted that also the shape and length of the antenna has an impact on the emitted THz pulse and its spectrum [69–71].

Detection of the THz pulses generated in a broadband THz antenna can be done by photoconductive sampling in an antenna structure identical to the THz emitter structure. A portion of the femtosecond laser pulse train, synchronized to the femtosecond pulse train used for the THz generation, is split off and used to excite, or gate the detector structure. In contrast to the THz emitter antenna, the detector antenna is not biased by an external circuit. The electric field required to drive a photocurrent in the antenna is supplied by the THz pulses, which arrive in synchronism with the gate pulses. The photocurrent in the antenna circuit is then a convolution of the electric field picked up by the antenna and the transient photoconductivity induced by the gate pulse,

$$J(\tau) \propto \int_{-\infty}^{\infty} E_{\mathrm{THz}}(t) g(t - \tau) \, \mathrm{d}t . \tag{9}$$

The transient photoconductivity of the detector can be described by the same kinetics as discussed above for the generation of THz radiation. In the limit of a transient photoconductivity response $g(t)$ much faster than the duration of the THz field, the detected current is directly proportional to the THz field strength, corresponding to a frequency response $J(\omega) \propto E_{\mathrm{THz}}(\omega)$. In the opposite limit, with long-lived photoconductivity, the measured current is proportional to the

temporal integral of the THz field, corresponding to a frequency response $J(\omega) \propto E_{\mathrm{THz}}(\omega)/\omega$. In the intermediate case, which is the normal case, the detected photocurrent will have a frequency response that can be described as [72]

$$J(\omega) \propto I(\omega)R(\omega)E_{\mathrm{THz}}(\omega), \qquad (10)$$

where $I(\omega)$ is the spectrum of the excitation laser pulse, and $R(\omega)$ is the frequency response of the photoexcited carriers in the semiconductor switch.

Hence, the bandwidth of the detector is limited by the trapping and recombination time of the photoinduced carriers and the transient photoconductivity can be seen as a low-pass filter function that is applied to the frequency spectrum of the THz pulse incident on the detector.

The ultrafast carrier lifetime of both the emitter and the detector semiconductor material is advantageous for a high bandwidth of the detected THz signal. Historically, radiation-damaged silicon-on-sapphire (RDSOS) has been used as photoconductive material [73]. Currently, materials such as low-temperature-grown (LTG) GaAs with carrier lifetimes as low as a few hundred fs are used as the active material [74–77]. Recently, other materials with smaller bandgaps such as LTG-GaAsSb [78], LTG-InGaAs [79], superlattice structures with LTG-InGaAs/InAlAs [80–82] and ion-implanted InGaAs [83–85] have also been employed.

While the detection bandwidth in most systems described in the literature are in the low THz range, it was recently demonstrated that by removing all absorbing elements in the THz beam path and using the shortest possible laser pulses, photoconductive detection of frequencies approaching 100 THz has been reported [72], and by using extremely broadband THz pulses generated in the organic crystal DAST (4-dimethylamino-N-methyl-4-stilbazollium tosylate) by optical rectification of 5-fs laser pulses, frequencies in the 100–150 THz range were detected using a LTG GaAs photoconductive antenna [86].

It has been noted that materials with long-lived photoconductivity can also be used for detection of high-bandwidth THz signals, although with higher noise levels than in materials with ultrafast response time [87].

A complete setup for photoconductive generation and detection of THz pulses is shown in Fig. 5a in the following section.

2.2. Continuous-wave THz generation and detection

Here, we will discuss a method related to femtosecond excitation for optoelectronic generation and detection of coherent, narrow-band THz radiation. This method is based on beating of two laser wavelengths λ_1 and λ_2 in a biased semiconductor photomixer [88]. If the response of the photoconductive material is faster than the beat frequency of the two laser lines then the photocurrent will be modulated at the beat frequency $\nu_{\mathrm{THz}} = c|1/\lambda_1 - 1/\lambda_2|$, which can fall in the THz range with a suitable choice of laser sources. If the photomixer is connected to a properly designed antenna, THz radiation will be emitted into free space. The

continuous-wave (CW) THz radiation can be collimated and guided in much the same manner as described in the previous section.

In the small-signal limit the output power at the difference frequency $\omega = 2\pi\nu_{\mathrm{THz}}$ is [88, 89]

$$P(\omega) \approx \frac{R_L}{2}\eta^2\lambda_1\lambda_2\left(\frac{\mathrm{e}}{hc}\right)^2\frac{P_1P_2}{(1+\omega^2\tau^2)(1+\omega^2R_L^2C^2)},$$
$$(11)$$

where P_1 and P_2 are the pump powers of the laser wavelengths λ_1 and λ_2, respectively, η is the external quantum efficiency (assumed to be equal for the two excitation wavelengths), R_L is the load resistance of the THz antenna circuit attached to the photoconductive region, C is the photomixer capacity, and τ is the lifetime of the photoexcited carriers. In the high-frequency limit the expression for $P(\omega)$ rolls off with a $\omega^{-4}\tau^{-2}C^{-2}$ frequency dependence (-12 dB/octave), indicating that a small photomixer capacitance C and ultra-short carrier lifetime τ is key for high-frequency operation.

The active region of the photomixer is normally designed with interdigitated electrodes with a spacing in the range of 0.1–1 µm and widths in the range of 0.2–0.5 µm. The capacitance of the active region is typically in the range of a few fF, depending on the detailed layout of the electrode region [90]. With such small design dimensions, electron-beam lithography is required for the definition of the electrode pattern on the semiconductor material.

The antenna load resistance R_L can be optimized by careful design of the antenna geometry. Resonant increase of the antenna load resistance at a specific design frequency, for instance with slot [90, 91], dipole [91, 92], or double-dipole [90] geometry, results in significant enhancement of the THz photomixer output compared to a broadband log-spiral antenna. The steep frequency roll-off of 12 dB/octave of the broadband log-spiral antenna can be reduced to -6 dB/octave by incorporation of resonant designs such as the dual-dipole antenna [90] where the antenna capacitance can be removed at the resonance frequency by inductive tuning.

The strong dependence of the output power on the external quantum efficiency may be exploited to design highly efficient emitters by applying an antireflection coating to the photomixer area, incorporating a high-dielectric reflector below the photomixer material, and optimizing the thickness of the photoconductive layer for cavity-enhanced absorption of the incident pump photons in the top layer of the photomixer material. Designs with this strategy indicate that it is possible to obtain several µW of output power from the photomixer at near-THz frequencies [89].

The small active area of a photomixer limits the output power due to saturation and eventually optical damage of the photomixer. Several more advanced photomixer designs that all aim at generation of as high a coherent THz output power as possible, have been published. Matsuura et al. [93] demonstrated a design with distributed excitation of a coplanar stripline structure fabricated on LTG-GaAs. A high optical-to-THz conversion efficiency was obtained by matching the propagation speed of the generated THz wave on the coplanar stripline with the sweep speed of the

optical interference fringes generated by the two optical excitation beams, incident at an angle with respect to each other. The output power of this device was lower than predicted, reaching the 0.1 μW level at 1 THz, applying a CW optical power of 300 mW. Shi et al. demonstrated an optimized waveguide design based on a metal-semiconductor-metal traveling-wave photodetector [94]. They employed femtosecond laser pulses transmitted through an etalon filter and hence converted into short bursts of high-repetition-rate (up to 1.6 THz) pulse trains. With an average optical power of only 0.66 mW of their 82-MHz repetition-rate femtosecond laser, they reported an average output power of 0.135 μW at 1.6 THz, corresponding to a peak THz power of 1.6 mW.

Another approach to generation of high power at THz frequencies is to use a high-speed photodiode structure such as the uni-traveling-carrier photodiode (UTC-PD) which uses only low-mass electrons as active charge carriers and achieves an output power of 2.6 μW at 1.04 THz using a log-spiral antenna [95–97] and 10.9 μW at 1.04 THz, using a resonant twin-dipole planar antenna [97,98].

Another advanced structure is the superlattice nanodiode n-i-p-n-i-p structure [99] which uses a cascaded series of nanodiodes to overcome the tradeoff between the RC time constant and the transit time limitations in simple photomixer and pin-diode designs. With a two-period design an output power of 0.032 μW at 1 THz was obtained [100], with a scaling to higher powers predicted by increasing the number of nanodiodes in the design.

The amplitude and the phase of the CW THz wave can be detected coherently with a homodyne detection scheme [51,58]. Here, the same two wavelengths of laser light λ_1 and λ_2 are mixed in a second photomixer, again creating a carrier density that oscillates at the beat frequency ν_{THz}. The THz field, generated by the same laser sources, has a high degree of coherence with this beat frequency, and hence the amplitude and phase of the THz field can be measured by scanning the phase of the carrier beat frequency with respect to the phase of the THz field, while monitoring the induced photocurrent.

The generation and detection principles here described for CW THz generation by photomixing are in very close analogy to the generation and detection principles involved in the pulsed technique of THz-TDS described in Sect. 2.1. In the broadband THz-TDS technique the transient photocurrent can be seen as a superposition of all beat frequencies of laser modes within the bandwidth of the femtosecond laser source, and the resulting THz pulse is created by the coherent superposition of all the generated beat frequencies. Hence, a system optimized for CW generation and detection over a wide frequency range will also work in pulsed mode, by replacing the dual-color laser source by a femtosecond laser source. As an intermediate state between the CW mode of operation and the broadband, pulsed mode of operation, the simultaneous generation and coherent detection of multiple THz frequencies was demonstrated using multimode laser diodes [59–62,101].

Broadband spectroscopy can be carried out with a CW THz system by tuning the frequency difference ν_{THz} be-tween the two laser lines. The bandwidth of such a CW THz spectroscopy system is determined by similar factors as in THz-TDS; the open aperture of the THz optics determines the lower frequency cutoff, whereas the high-frequency response of the emitter and detector determines the upper frequency cutoff. Using a helium-cooled bolometer for incoherent detection of the CW THz radiation generated from a log-spiral antenna, a CW system operating up to 3.5 THz has been applied for high-resolution spectroscopy of biomolecular samples [14]. Systems also employing a photomixer for coherent detection typically display a high-frequency limit of operation in the range below 1.5 THz [54], with a dynamic range of 60 dB at 0.53 THz demonstrated by Gregory et al. [52].

The frequency resolution of the CW THz spectroscopy system is determined by the linewidth and stability of the two laser lines, and hence also on the stability of the beat frequency between the two laser lines. The spectrum with the highest spectral resolution obtained with a CW THz spectroscopy system based on the photomixing principle showed a spectral resolution better than 4 MHz [102]. A spectral resolution in the low MHz range was also demonstrated using a combination of an amplified diode laser and a Ti:sapphire ring oscillator [14], and a dual-color Ti:sapphire laser was used for THz imaging with a spectral resolution better than 150 MHz [54,103]. Thus, the frequency resolution offered by CW THz spectroscopy is significantly higher than that available with other spectroscopic techniques in the THz range. A complete setup for coherent generation and detection of CW THz radiation by photomixing is shown in Fig. 5b in the following section.

2.3. Nonlinear generation and detection of THz pulses

Here, we discuss the method of generation of broadband THz pulses by intense excitation of nonlinear crystals and detection of the THz pulses in electro-optic crystals. Generation of sub-THz and THz radiation by nonlinear frequency mixing of laser beams was first demonstrated by Shen and his group. Specifically, Faries et al. demonstrated the generation of 1.2–8.1 cm^{-1} (36–243 GHz) radiation by mixing in LiNbO$_3$ and quartz [104]. The frequency range of the difference-frequency generation was later extended to the 20–38 cm^{-1} (0.6–1.14 THz) range by using different laser lines of two ruby lasers [105]. By using modelocked pulses of 5-ps duration from a Nd:glass laser, it was then demonstrated that single laser pulses also could be used for generation of far-infrared radiation, covering the 3–16 cm^{-1} (0.1–0.5 THz) range [106].

The generation of THz radiation by short laser pulses relies on efficient difference-frequency mixing of all the frequency components within the spectrum of the laser pulse. The result of this process is a distribution of difference frequencies that in the time domain appears as an electric field transient with a shape similar to the envelope of the laser pulse. For this reason, the process was later referred to as optical rectification. Two factors influence the bandwidth and

the temporal shape of the generated THz transient, namely the bandwidth of the excitation pulse and the phase matching between the near-infrared pump beam and the generated THz field.

Xu et al. used photoconductive sampling to characterize the temporal pulse shape of electromagnetic transients with THz-frequency content, generated by femtosecond excitation of $LiNbO_3$ and $LiTaO_3$ [107] and Rice et al. demonstrated THz emission from GaAs and CdTe [108], originating from optical rectification of the excitation pulse.

Field-resolved detection of freely propagating THz pulses can be achieved by electro-optic sampling, which can be seen as the complementary process of THz generation by difference-frequency mixing, and was first demonstrated in 1995 by three independent groups, using $LiTaO_3$ [109, 110] and a poled polymer [111] as electro-optic media, respectively. The subsequent introduction of ZnTe in free-space electro-optic sampling [112] addressed initial challenges with poor phase matching. ZnTe is well phase matched for generation of THz radiation with laser pulses near 800 nm, the preferred wavelength range for Ti:sapphire lasers.

In this wavelength range, ZnTe displays good phase matching up to a few THz [113] for generation and detection of near-single-cycle THz transients, limited by absorption due to difference-frequency modes and the strong absorption and dispersion of the phonon at 5.3 THz [114–116]. One method to overcome this limitation is to choose a nonlinear crystal with higher phonon resonance frequency, most notably GaP that has a broadband response to 7–8 THz [117]. For the generation and detection of THz transients with still higher bandwidth, the nonlinear crystal must be thin in order to maintain approximate phase matching over a wide bandwidth. This thinning down of the crystal leads to a smaller electro-optic response that is proportional to crystal thickness and complications due to multiple reflections of the THz pulse inside the crystal. In order to operate at frequencies above the TO phonon, thin ($< 30 \, \mu m$) ZnTe was used for generation and detection of THz transients with bandwidth exceeding 30 THz [118], and later, detection to beyond 41 THz was demonstrated [119]. The combination of thinnest possible nonlinear crystals with optimized phase-matching conditions and the shortest possible laser pulses ($< 10 \, fs$) was used to demonstrate generation and detection of frequencies higher than 100 THz and thus approaching the near-IR region [120]. The applications made possible with such a unique light source are discussed in Sect. 5.4.

The mathematical description of the generation and detection process is based on solving the wave equation under the conditions of the propagating waves in a nonlinear crystal, as described for instance in Boyd [121]. Bakker et al. [122] discussed distortion of the electro-optic sampling signal, and included the frequency-dependent phase matching between the probe beam and the THz beam, the frequency-dependent reflection coefficient at the detector crystal interfaces, and the dispersion and absorption of the THz pulse in the crystal. Leitenstorfer et al. [123] included the dispersion of the second-order nonlinearity in the generation and detection process. Gallot and Grischkowsky [124] included the dispersion of the probe beam in the description
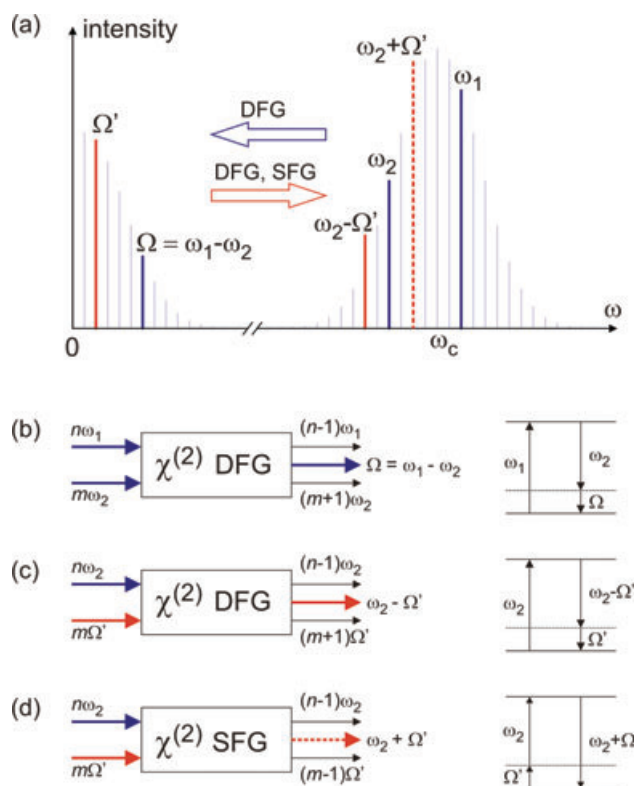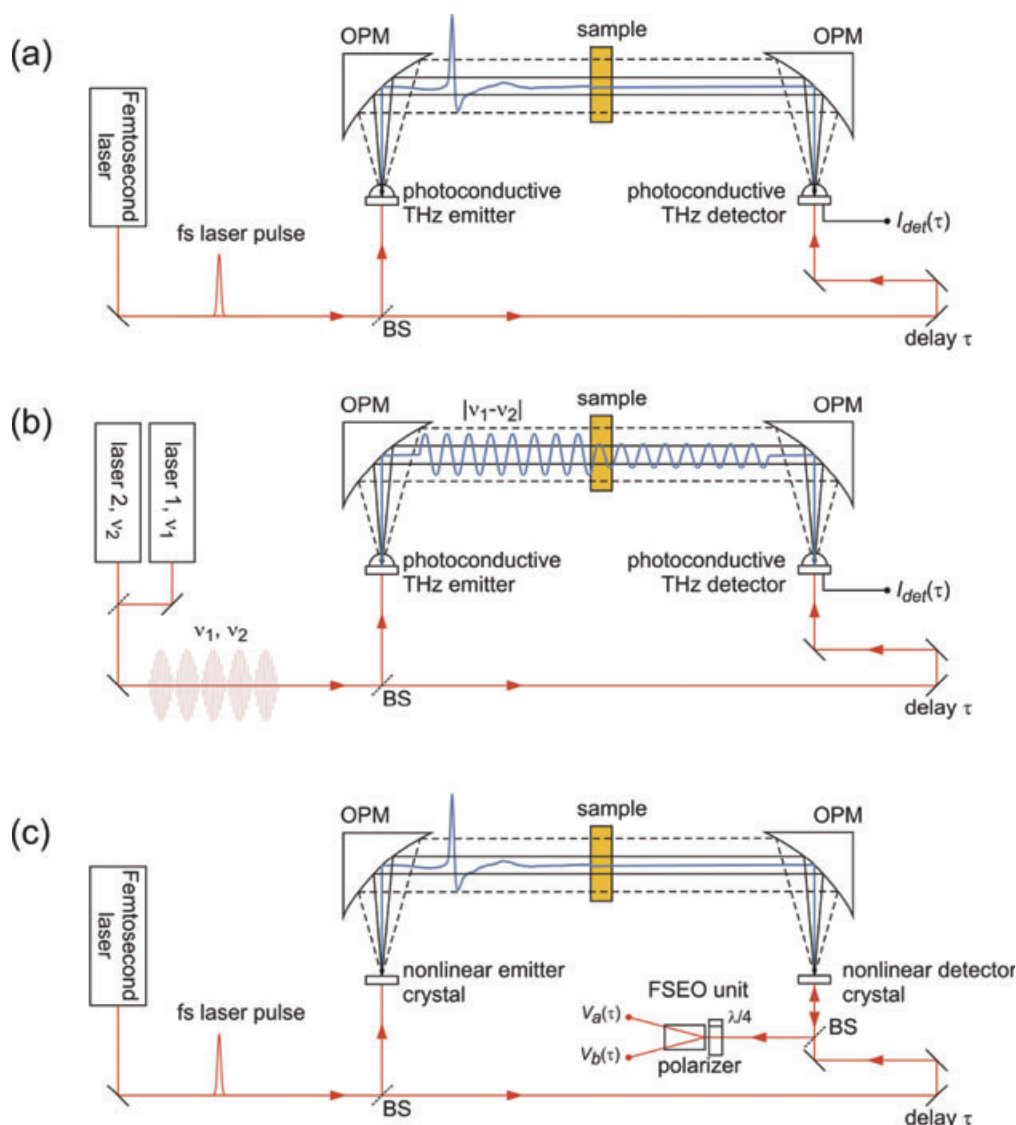

Figure 4　(online color at: www.lpr-journal.org)　(a) Schematic representation of difference-frequency generation (DFG) of THz frequencies and DFG and sum-frequency generation (SFG) of sidebands to the pump frequencies. (b)–(d) Illustration of the DFG of THz generation, DFG of redshifted sidebands and SFG of blueshifted sidebands to the laser frequencies.

of free-space electro-optic sampling, and Kaindl et al. [125] included dispersion of the pump beam in the generation crystal. Based on these theoretical considerations, there is now a clear picture of the full nonlinear generation and detection process in thin crystals.

Figure 4 illustrates the nonlinear processes involved in generation and detection of THz radiation in nonlinear crystals. A femtosecond laser pulse with a spectrum centered at ω_c contains a comb of equidistant frequencies, spaced by $\Delta\omega$ due to the constant repetition rate of the laser. Each possible combination of two of these frequencies, here illustrated as ω_1 and ω_2, will be able to mix in the nonlinear medium, which then generates the difference frequency $\Omega = \omega_1 - \omega_2$. This process, together with the involved frequencies, is illustrated with blue color in Fig. 4.

In the nonlinear crystal the THz photons interact with the pump photons and create sidebands to the pump frequencies, as indicated with red color in Fig. 4 where the nonlinear interaction between a THz photon at frequency Ω' and a photon at ω_2 generates the frequencies $\omega_2 - \Omega'$ and $\omega_2 + \Omega'$ by difference- and sum-frequency generation (DFG and SFG), respectively. The diagrams (b)–(d) in Fig. 4 further illustrate these three processes.

As will be discussed below, the SFG process is the physical mechanism that leads to the electro-optic effect, which

Figure 5 (online color at: www.lpr-journal.org) Schematic configuration of a full THz-TDS system for transmission spectroscopy, using (a) broadband THz antennas driven by femtosecond laser pulses and (b) continuous-wave THz photomixers and two single-color lasers and (c) nonlinear electro-optic crystals.

is widely used for optical detection of the THz field. The electro-optic effect leads to phase retardation between the two polarization components of a probe beam, proportional to the applied electric field, which for zincblende crystals has the form

$$\Delta\varphi = \frac{\omega_{\mathrm{opt}} n_0^3 r_{\mathrm{eff}} E_{\mathrm{THz}}}{c}, \qquad (12)$$

where n_0 is the static index of refraction of the crystal at the near-IR probe wavelength and r_{eff} is the effective electro-optic coefficient. Thus, an optical setup that can detect the phase retardation between two polarization components of the near-IR probe beam can be used for detection of the field strength of the THz beam. A complete setup for nonlinear generation and detection of THz pulses is illustrated in Fig. 5c.

Here we describe the electric field of the laser in the frequency domain as $E(\omega, z) = A(\omega)\, \mathrm{e}^{\mathrm{i}k(\omega)z}$, where the time dependence $\mathrm{e}^{-\mathrm{i}\omega t}$ has been omitted, and $A(\omega)$ is the slowly varying complex spectral amplitude, decoupled from the acquired phase.

Solving the nonlinear wave equation for the difference-frequency generation (DFG) process in the slowly varying amplitude approximation then yields [121, 125]

$$E(\Omega, z) = \qquad (13)$$

$$\frac{\Omega^2\, \mathrm{e}^{\mathrm{i}k(\omega)z}}{k(\Omega)c^2} \int_{-\infty}^{\infty} \chi_{\mathrm{eff}}^{(2)}(\Omega) A(\omega + \Omega) A^*(\omega) \frac{\mathrm{e}^{\mathrm{i}\Delta k(\omega,\Omega)z} - 1}{\Delta k(\omega, \Omega)}\, \mathrm{d}\omega,$$

where z is the length of the nonlinear crystal, $\chi_{\mathrm{eff}}^{(2)}$ is the effective second-order susceptibility, and Ω is the difference frequency in the THz range. As noted by Kaindl et al., Eq. (13) includes the effect of dispersion of the pump pulse as it propagates through the generation crystal. Thus, this equation is of general applicability, as long as the pump field is not significantly depleted or modified by the generated THz field.

Phase matching is required in order for the generation process to be efficient. The phase mismatch between the two frequencies $\omega + \Omega$ and ω of the optical beam and the

generated THz frequency Ω is [126]

$$\Delta k(\omega, \Omega) = \frac{1}{c}\left(n(\omega+\Omega)(\omega+\Omega) - n(\omega)\omega - n(\Omega)\Omega\right)$$
$$(14)$$

$$\approx \frac{\Omega}{c}\left(n(\omega) + \omega\frac{dn(\omega)}{d\omega} - n(\Omega)\right)$$

$$\approx \frac{\Omega}{c}\left(n_{\mathrm{g}}(\omega_0) - n(\Omega)\right), \qquad (15)$$

where n and n_{g} are the phase and group index of refraction, respectively. The group velocity approximation (last half of Eq. (15)) is valid when $\Delta\omega \ll \omega_0$. Within this approximation, the generation of THz radiation can be described as

$$E(\Omega, z) = \frac{\Omega^2\,\mathrm{e}^{\mathrm{i}k(\Omega)z}}{k(\Omega)c^2}\chi_{\mathrm{eff}}^{(2)}(\Omega)\frac{\mathrm{e}^{\mathrm{i}\Delta k(\omega_0,\Omega)z}-1}{\Delta k(\omega_0,\Omega)}C(\Omega), \quad (16)$$

where $C(\Omega) = \int A(\omega+\Omega)A^*(\omega)\,\mathrm{d}\omega$ is the autocorrelation of the spectrum of the laser pulse.

The detection of THz radiation by free-space electro-optic sampling has been described in a generally applicable way by Gallot and Grischkowsky [124], who formulated the detection mechanism as phase modulation of the probe beam by sum-frequency generation by mixing of THz photons and photons from the probe beam.

Following the treatment by Gallot and Grischkowsky [124], the electro-optic sampling signal at a relative time delay τ between the THz signal and the probe pulse can be expressed as the integral

$$S(\tau) = \frac{\pi\varepsilon_0}{c}\int_{-\infty}^{\infty} E(\Omega)f(\Omega)\,\mathrm{e}^{-\mathrm{i}\Omega\tau}\,\mathrm{d}\Omega, \qquad (17)$$

which is the inverse Fourier transformation of the product of the incident THz spectrum and a filter function $f(\Omega)$ that takes into account the dispersion of the probe beam in the detector crystal, the frequency-dependent phase mismatch between the THz field and the probe pulse, and the frequency dependence of the sum-frequency generation efficiency responsible for the phase retardation between the two orthogonal components of the probe beam polarization,

$$f(\Omega) = \int_{-\infty}^{\infty} \frac{\omega^2}{|k'(\omega)|}\mathrm{e}^{-2\beta(\omega)z}\chi_{\mathrm{eff}}^{(2)}(\omega)$$
$$\times \frac{\mathrm{e}^{\mathrm{i}\Delta k(\omega,\Omega)z}-1}{\mathrm{i}\Delta k(\omega,\Omega)}A^*(\omega)A(\omega-\Omega)\,\mathrm{d}\omega, \qquad (18)$$

where $k'(\omega)$ and $\beta(\omega)$ are the real and imaginary parts of the complex wave number $k = k' + \mathrm{i}\beta$, and thus β expresses the frequency-dependent loss at optical frequencies of the nonlinear crystal.

For laser fields with a small relative bandwidth, the group velocity approximation is valid, and Eq. (18) can be

approximated by

$$f(\Omega) \propto \frac{\mathrm{e}^{\mathrm{i}\Delta k(\omega_0,\Omega)z}-1}{\mathrm{i}\Delta k(\omega_0,\Omega)}\int_{-\infty}^{\infty} A^*(\omega)A(\omega-\Omega)\,\mathrm{d}\omega$$
$$= P(\Omega, \omega_0)C(\Omega), \qquad (19)$$

which is the product of the phase mismatch function $P(\Omega, \omega_0)$ and the autocorrelation of the laser spectrum $C(\Omega)$.

If the intensity of the generated THz frequencies is sufficiently high, the THz photons can interact with the pump photons in a cascaded process [127, 128] which leads to further generation of THz frequencies and a significant redshift of the pump spectrum [129].

Recently, there has been increased interest in generation and detection of ultrashort THz transients by four-wave mixing in the focal region of intense laser fields in air and other gases [130–132].

3. Static terahertz time-domain spectroscopy

The photoconductive and nonlinear THz emitters described in the previous sections are remarkably stable and reproducible with respect to the generated signal shape. Therefore, such emitters are well suited for spectroscopic measurements when combined with a similar THz detector. As illustrated in Fig. 5a the THz emitter and THz detector can be excited with fractions of the same, synchronized train of femtosecond pulses. For comparison, Fig. 5b shows the corresponding setup for CW THz generation and sampling using THz photomixers excited with fractions of the same two single-frequency laser sources. The close connection discussed in the previous section between the two techniques is evident from these schematic illustrations. Figure 5c shows a THz-TDS system based on nonlinear generation and detection of the THz pulses, where the main difference compared to a photoconductive system is the free-space electro-optic sampling unit.

The beam of THz pulses can be transported from the emitter to the detector with either reflective or transmissive optics. Mostly, the reflective optics used are off-axis paraboloidal mirrors with metallic reflectors, but elliptical mirrors can also be used, depending on the required focusing and imaging of the THz beam through the optical system. Reflective optics has little loss due to the high conductivity of most metals in the THz range, but may be difficult to align properly. On the other hand, transmissive optics can be aligned more easily than reflective optics, but usually suffers from frequency-dependent absorption that often leads to attenuation of the high frequency components of the THz radiation and thus hinders high-frequency operation of the spectroscopy system.

Transmissive optics is typically seen in the form of lenses with spherical or aspherical surfaces. Such lenses are typically manufactured from transparent polymer materials such as polyethylene (PE) or teflon, and recently more

transparent and low-dispersion materials based on cyclic olefin copolymers have been characterized [133] and used. Also high-resistivity silicon is widely used as lens material for THz applications due to its exceptionally low loss and low dispersion [134].
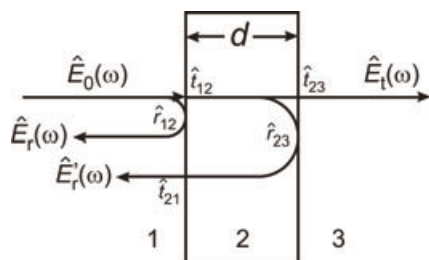
High-resistivity silicon hyperhemispherical lenses are often used to couple the THz radiation from the emitter antenna into free space, and to couple the THz radiation from free space and onto the detector antenna. Hyperhemispherical lenses were first introduced by Fattinger and Grischkowsky [135, 136]. The THz radiation patterns from hyperhemispherical silicon lenses have been characterized [64, 137] and found to be described, at least approximately, by a fundamental Gaussian beam with beam waist at the surface of the hyperhemispherical lens. Different lens shapes (collimating, hemispherical and hyperhemispherical shapes) have been thoroughly characterized by Rudd and Mittleman [138]. Reiten et al. performed careful measurements and simulations of the propagation of THz beams through hyperhemispherical lenses and the subsequent optical system of a THz-TDS setup [139, 140]. They showed that the THz beam profile emerging from a lens-coupled photoconductive emitter is accurately described by a superposition of Laguerre-Gauss modes, and also discussed the influence of spherical aberration and surface waves on the propagation. Recently, Lo and Leonhardt [141] devised aspheric lens designs with optimized focusing properties for high-resolution THz imaging applications.

3.1. Data analysis in transmission THz-TDS

Here, we describe the basic methods used in transmission and reflection spectroscopy, and discuss the influence of the dynamic range and the signal-to-noise ratio in a typical THz-TDS measurement. The first application of transmission THz-TDS was on water vapor in the ambient atmosphere [47] and subsequently the absorption coefficient and index of refraction of a range of dielectrics and semiconductors were reported [142].

In Fig. 6 the general geometries for transmission and reflection measurements are illustrated.

The incident THz pulse is characterized by its spectral amplitude and phase $\hat{E}_0(\omega)$, obtained by Fourier transfor-

mation of the raw experimental data, the time-domain representation of the pulse, as illustrated in Fig. 3. Ignoring, for the time being, multiple reflections in the sample, the transmitted and reflected signals are in this geometry given by

$$\hat{E}_t(\omega) = \hat{E}_0(\omega)\hat{t}_{12}\hat{t}_{23}\,e^{-\alpha d/2}\,e^{in\omega d/c},$$
$$\hat{E}_r(\omega) = \hat{E}_0\hat{r}_{12}, \qquad (20)$$
$$\hat{E}'_r(\omega) = \hat{E}_0\hat{t}_{12}\hat{r}_{23}\hat{t}_{21}\,e^{-\alpha d/2}\,e^{in\omega d/c},$$

where $\hat{t}_{12}, \hat{t}_{23}, \hat{r}_{12}$, and $\hat{r}_{23}$ are the various complex Fresnel field transmission and reflection coefficients as defined in Fig. 6.

Measurements carried out either in transmission or reflection can be used for the extraction of the complex index of refraction of the sample, $\hat{n}(\omega) = n(\omega) + i\,\kappa(\omega)$. Here, $\kappa(\omega)$ is the extinction coefficient, related to the absorption coefficient $\alpha(\omega)$ through $\kappa(\omega) = \alpha(\omega)c/2\omega$. In the simplest transmission experiment, two THz pulses, propagating through air and through the sample, respectively, are recorded and their spectral amplitudes and phases are compared as

$$\frac{\hat{E}_{\mathrm{sam}}(\omega)}{\hat{E}_{\mathrm{ref}}(\omega)} = T(\omega)\,e^{i\,\varphi(\omega)} = \hat{t}_{12}\hat{t}_{23}\,e^{-\alpha d/2}\,e^{i(n-1)\omega d/c}. \quad (21)$$

If we for now limit the analysis to sample materials with low absorption coefficient then the Fresnel transmission coefficients are real-valued, and at normal incidence we find
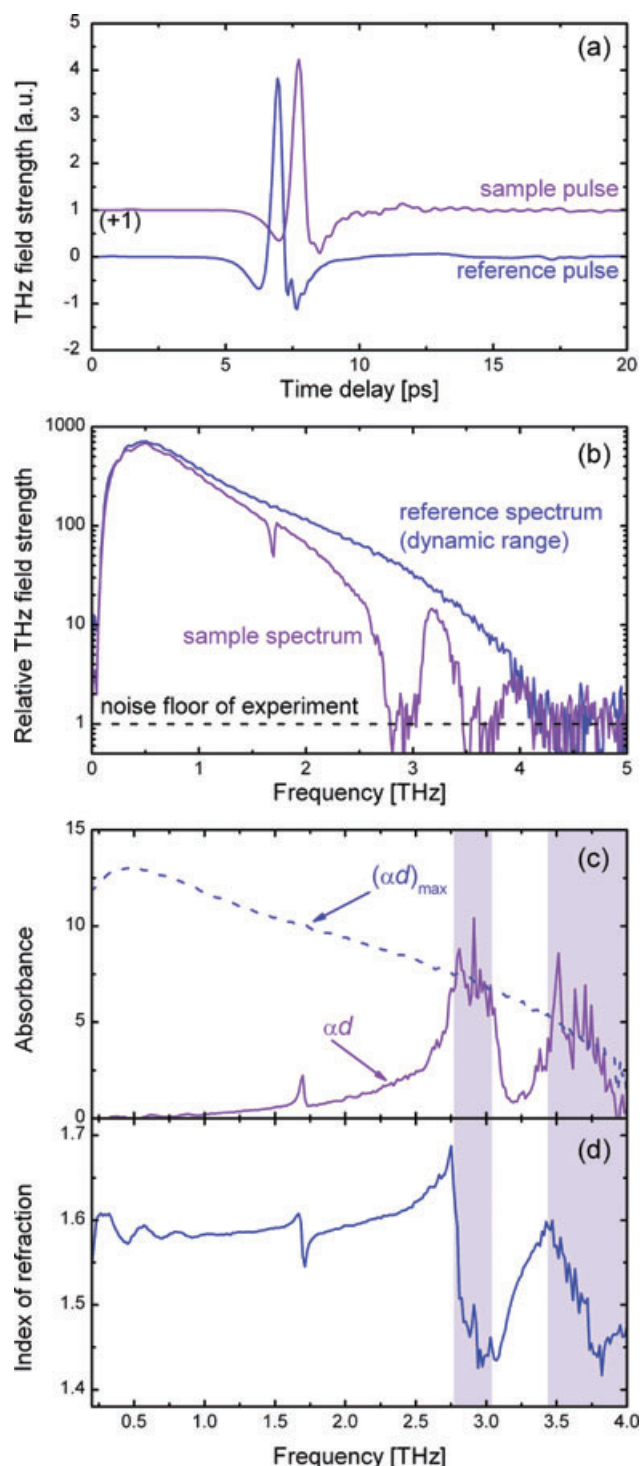
$$n(\omega) = 1 + \frac{\varphi(\omega)c}{\omega d}, \qquad (22)$$

$$\alpha(\omega) = -\frac{2}{d}\ln\left(\frac{(n+1)^2}{4n}T(\omega)\right). \qquad (23)$$

In Fig. 7 we show an example of a transmission THz-TDS measurement. The sample was a mixture of the pure DNA base cytosine and PE filler material, and the sample was placed in a cryostat and kept at a nominal temperature of 10 K during measurements [143].

Figure 7a shows the time traces of the reference and sample signals, recorded after transmission through dry air and the sample pellet, respectively. Both traces are truncated at the same position, slightly before the appearance of the first echo due to multiple reflection in the sample pellet. Figure 7b shows the frequency spectra of the two signals, and Fig. 7c shows the extracted absorbance (the product of absorption coefficient α and sample thickness d), together with a curve showing the highest detectable absorbance in the given experiment. Figure 7d shows the extracted index of refraction of the cytosine sample.

Figure 7b shows that the THz reference signal reaches the noise floor of the experiment at high frequencies, here at 4 THz. Obviously, at frequencies above this cutoff point no meaningful measurements are possible, but also at frequencies below the cutoff the results might be impeded by the limited frequency-dependent dynamic range of the experiment, defined as the strength of the reference signal with

Figure 6 Schematic illustration of the geometries for transmission and reflection spectroscopy. $\hat{E}_0(\omega)$ is the incident field, $\hat{E}_t(\omega)$ is the transmitted field, and $\hat{E}_r(\omega)$ and $E'_r(\omega)$ are the fields reflected from the first and second interface of the sample, respectively.

Figure 7 (online color at: www.lpr-journal.org) (a) Time traces of the reference and sample pulses in a transmission THz-TDS experiment, (b) frequency spectra of the reference and sample pulses with respect to the noise floor of the experiment, (c) the extracted absorbance αd and the highest detectable absorbance $(\alpha d)_{max}$, and (d) index of refraction of the sample material. The sample consisted of a mixture of cytosine and PE filler, and the measurement was carried out with a nominal sample temperature of 10 K.

respect to the noise floor of the experiment. The highest absorbance that can be measured with a given dynamic range DR corresponds to the situation where the sample signal is at the same level as the noise floor [144]. This can be expressed as

$$(\alpha d)_{max} = 2\ln\left(DR\frac{4n}{(n+1)^2}\right). \qquad (24)$$

The curve showing the largest detectable absorbance in the given experiment is shown together with the extracted absorption coefficient in Fig. 7c.

The strongest absorption lines in the measured spectrum are clearly saturated, as indicated by the shaded areas in Figs. 7c and d, and the roll-off of the absorption at high frequencies is a direct consequence of the limited dynamic range of the experiment.

The analysis outlined above gives analytical, closed-form solutions to the inversion of the equations linking the measured transmission amplitude and phase to the optical properties of the sample.

However, Eqs. (22) and (23) are only strictly valid for samples with vanishing absorption and infinite thickness. Finite absorption leads to additional phase shifts due to the complex-valued Fresnel transmission coefficients. For thin samples with high absorption (e. g. liquid water or highly doped semiconductors) the phase change due to the Fresnel coefficients becomes comparable to the accumulated phase change due to propagation through the sample. Hence, the separate calculation of the real part of the refractive index from the phase of the sample signal relative to the reference signal is no longer possible. In Fig. 8 the effect of the additional phase shift at the sample interfaces is demonstrated. The dielectric function of liquid water was measured using a transmission cell with a water layer thickness of $d = 76\,\mu$m. The dashed lines show the result of the simplified analysis
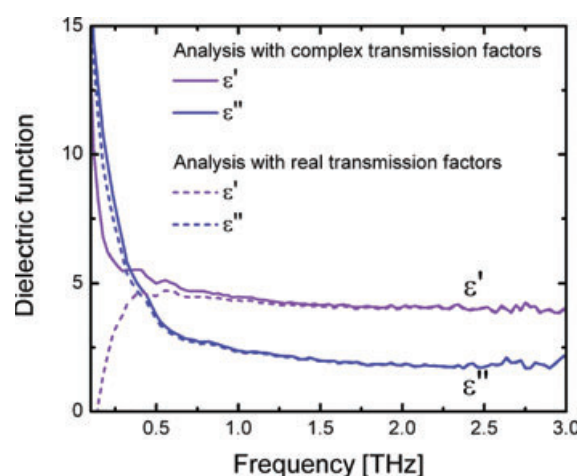
Figure 8 (online color at: www.lpr-journal.org) Real (ε') and imaginary (ε'') part of the dielectric function of pure water at room temperature, extracted from transmission THz-TDS data measured with a 76-μm thick water layer using complex-valued (solid lines) and real-valued (dashed lines) Fresnel transmission functions.

using Eqs. (22) and (23) to calculate the dielectric function $\varepsilon = \varepsilon' + i\varepsilon'' = (n + i\kappa)^2$, and the solid lines show the results of a full iterative analysis including the phase shift due to the imaginary part of the index of refraction in the Fresnel transmission coefficients.

The correct extraction of especially the real part of the dielectric function is in this example strongly dependent on the inclusion of the interfacial phase shifts. Whereas the full analysis correctly reproduces the known dielectric function of water [16, 145–149], the simpler analysis completely fails to reproduce the sharp increase of ε' towards its static value ε_{DC} at low frequencies.

Thin samples will result in multiple reflections of the signal inside the sample and consequently the time domain trace of the sample signal will contain a sequence of signal echoes following the main transmitted pulse. This general situation was considered in detail by Duvillaret et al. [150] who included a Fabry-Perot factor $FP(\omega)$ and complex-valued Fresnel transmission coefficients in their data analysis. For a sample in air the generalized transmission function $\hat{T}(\omega)$ is [150]

$$
\hat{T}(\omega) = \frac{\hat{E}_{\text{sam}}(\omega)}{\hat{E}_{\text{ref}}(\omega)}
$$

$$
= \frac{4\hat{n}}{(\hat{n}+1)^2} e^{-\alpha d/2} e^{in\omega d/c} FP(\omega), \qquad (25)
$$

where

$$
FP(\omega) = \frac{1}{1 - \left(\frac{\hat{n}-1}{\hat{n}+1}\right) e^{-\alpha d} e^{2in\omega d/c}}. \qquad (26)
$$

The solution of Eq. (25) requires an iterative procedure. Duvillaret et al. [150] devised methods for the extraction of the dielectric properties of optically thick samples that produces a well-separated sequence of Fabry-Perot echoes as well as optically thin samples where the Fabry-Perot echoes are overlaid in the time domain.

The presence of multiple echoes in the time-domain trace offers a method for the extraction of the sample thickness simultaneously with the determination of the index of refraction and the absorption coefficient of the sample. In a subsequent paper, Duvillaret et al. demonstrated a method applicable for any material with low absorption [151] that determines the thickness of a sample with great precision, and hence removes the uncertainty about the sample thickness. Precise knowledge about the sample thickness is a prerequisite for the precise determination of the index of refraction. A careful analysis of the echo sequence following the main transmitted signal through a sample allowed the same authors to analyze the influence of noise on the accuracy of the determination of the optical properties of samples [152].

Recently, the approach by Duvillaret was further refined by Pupeza et al. who introduced the spatially variant moving average filter [153]. This filter constitutes the core of an iterative algorithm yielding the physically most accurate modeled function out of a set of functions that have to satisfy certain boundaries. Scheller et al. introduced an

additional Fourier transform of the frequency dependent material parameters to a quasi-space regime [154]. In this quasi-space, periodic Fabry-Perot oscillations from the frequency domain, originating from multiple reflections inside the sample, lead to discrete peaks. By an iterative minimization of these peaks, the sample thickness, the refractive index and the absorption coefficient can be determined with high precision.

The selection of the optimal sample thickness for the best possible measurement of the optical properties of the material is a complicated procedure where the frequency-dependent dynamic range of the experiment must be taken into account together with the absorption coefficient at the specific frequencies. Different sample thicknesses may hence be required for a complete characterization of the absorption spectrum of a given sample. It was demonstrated [155] that for instance in PVC, a polar polymer with rather strong, frequency-dependent absorption in the THz range, the optimal sample thickness for minimal standard deviation of the complex index of refraction varies from 50 mm at 0.1 THz to 1 mm at 1 THz.

3.2. Line shape in transmission THz-TDS

Most spectroscopic results obtained on solid-state materials with THz-TDS focus on the line position and the relative intensity of the lines. Comparably few of the published studies deal with the detailed line shapes in the recorded spectra. However, if the spectral resolution of the THz-TDS measurement allows determination of the line profile then significant additional insight into the physical absorption mechanism can be obtained.

Korter and Plusquellic used a high-resolution continuous-wave THz spectrometer to observe asymmetric line shapes in the absorption spectrum of biotin [14]. They argued that vibrational modes in the THz region are particularly sensitive to anharmonicity of the vibrational potential since at room temperature the thermal energy of $k_B T = 25$ meV (or 6.2 THz) results in significant population of a wide range of the lowest levels of the vibrational potential. Anharmonicity of the vibrational potential will hence lead to a distribution of vibrational transition frequencies, typically shifted to the red for transitions between higher levels $v = n \rightarrow n - 1$ compared to the fundamental transition $v = 1 \rightarrow 0$. Using the Morse potential, an anharmonicity analysis could reproduce the asymmetric redshift of the absorption peaks of biotin when the temperature was increased from 4.2 K to room temperature.

Several published low-temperature spectra recorded on pellets of powder samples display a pronounced low-frequency absorption tail that is difficult to explain in terms of anharmonicity since only the lowest vibrational levels should be populated at low temperature. Franz et al. [156] discussed the origin of this asymmetric line shape, and demonstrated that a scattering phenomenon known in the literature as the Christiansen effect can be responsible for this asymmetric line shape. The Christiansen effect is observed in inhomogeneous samples where materials with different

dielectric properties are mixed. A typical example is the dilution of a sample material in a low-absorption filler material, and the effect is clearly visible in the data presented in Fig. 7. In THz-TDS the filler material is often polyethylene (PE) powder due to its favorable mechanical and sticking properties and its low absorption in the THz range. The sample material is ground to the desired particle size, and mixed with a suitable amount of PE. The mixture is then pressed to a mechanically stable pellet with a hydraulic press. If there is an index contrast between the filler material and the sample particles, THz light will be scattered away from the propagation axis when transmitting through the sample, and hence not be detected. The amount of scattering depends on the wavelength of the light, the particle size, and the index contrast between the filler material and the sample material. The index of refraction of a sample material with a strong and narrow resonance will change significantly near the resonance.
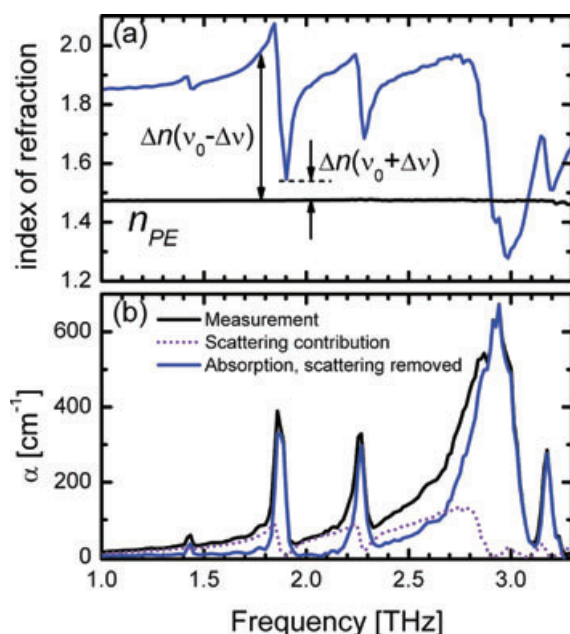
Figure 9a shows a measurement of the index of refraction of microcrystalline fructose, calculated from measurements on a ground sample diluted by PE filler [12]. The index of refraction of the PE material is also shown for comparison.

If a powder of the material with the narrow resonance is dispersed in a low-index filler matrix then the index contrast is larger on the low-frequency side than on the high-frequency side of the resonance, as indicated in Fig. 9a. Hence, the scattering probability can be significantly enhanced on the low-frequency side of a resonance due to the

increased dielectric contrast and the detected loss of THz signal will consequently have a contribution from scattering in addition to the contribution from absorption in the sample material. Franz et al. showed that analysis of the data recorded on an unground sample can separate the contributions from the material absorption and from scattering. The analysis requires independent knowledge of the index of refraction of the powder material and of the filler material. Once these quantities are known or can be estimated then the absorption can be corrected for the scattering contribution, according to the relation

$$\alpha' = \alpha + \alpha_s = \alpha + K^2 \frac{\omega^2}{c^2} (n - n_{PE})^2 \Delta. \qquad (27)$$

Here, n_{PE} is the refractive index of the filler material, here assumed to be PE, K and Δ are phenomenological model parameters introduced in a theoretical treatment of the Christiansen effect by Raman [157]. The parameter K is related to the shape, concentration and distribution of the particles and Δ is a model parameter describing the typical optical thickness of a single layer of particles. Franz et al. determined these parameters phenomenologically in the fitting procedure to produce a flat baseline between the absorption features in the corrected spectrum. The result of this procedure is illustrated in Fig. 9b where the black curve shows the apparent absorption coefficient of fructose, measured on finely ground microcrystalline powder mixed with PE filler. The purple curve shows the contribution from scattering, calculated by Eq. (27) with a suitable choice of the parameters K and Δ. The absorption coefficient of fructose, with the scattering contribution removed, is shown as the blue curve. The asymmetric shape of the measured absorption profiles are in most cases corrected to more symmetric line shapes, with less background absorption due to scattering.

3.3. Reflection THz-TDS

Spectroscopic information can also be obtained in reflection mode. In reflection mode the reference signal can be obtained either by replacing the sample with a known reflector such as a flat dielectric or metallic surface [158], or by placing a window in contact with the sample, and use the front surface reflection as reference signal and the reflection from the back surface of the window, in contact with the sample, as the sample signal [145].

The field reflection coefficient of a good metal far below the plasma frequency is $r_{metal} = -1$, independent of frequency. Using a metal surface as the reference reflector at normal incidence of the THz radiation the ratio of the sample reflection to the reference reflection is then

$$|r| e^{i\varphi} = \frac{\hat{n} - 1}{\hat{n} + 1} = \frac{n + i\kappa - 1}{n + i\kappa + 1}. \qquad (28)$$
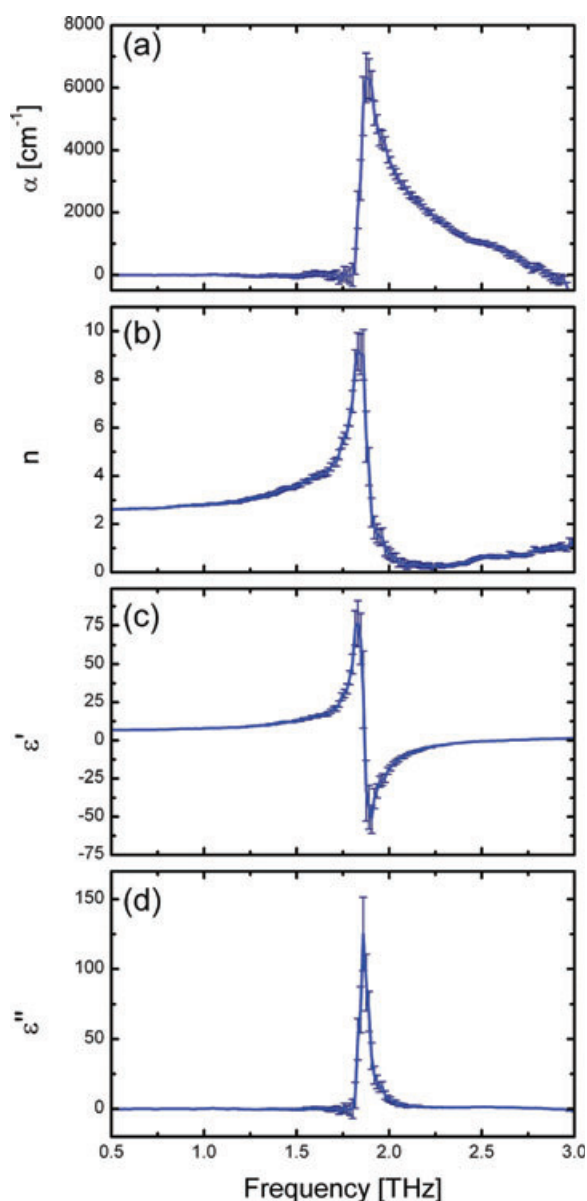
where $\hat{n} = n + i\kappa$ is the complex index of refraction of the sample material. This expression can be inverted to yield the index of refraction and the absorption coefficient of

Figure 9   (online color at: www.lpr-journal.org)   (a) index of refraction of fructose measured on a diluted powder sample, shown together with the index of refraction of PE. (b) Measured absorption coefficient (black curve) of fructose, contribution from scattering (purple, dotted curve) and absorption coefficient corrected for scattering (blue curve). Figure adapted from Franz et al. [156].

the sample,

$$n(\omega) = \frac{1 - |r|^2}{1 + |r|^2 - 2|r|\cos\varphi}, \qquad (29)$$

$$\alpha(\omega) = \frac{4\pi\nu}{c}\frac{2|r|\sin\varphi}{1 + |r|^2 - 2|r|\cos\varphi}. \qquad (30)$$

In Fig. 10 we show an example of a measurement of the phonon in cesium iodide (CsI), carried out using the reflection geometry with a metal reflector as reference. Fundamental phonons in ionic crystals show a very strong absorption coefficient, and thus transmission measurements are challenging [159]. The measurement shown in Fig. 10 is carried out on a bulk, microcrystalline disk of CsI [144], and the reflection geometry allows direct measurement of the dielectric spectrum of the phonon resonance at 1.84 THz without saturation of the dynamic range of the spectrometer.

While a reflection measurement circumvents the limitations on the highest detectable absorbance in a transmission experiment, there are still limitations to the highest absorbance that can be detected in a reflection measurement [144]. The largest absorption that can be measured is that of the reference metal, corresponding to unity reflection coefficient and the same phase shift of the sample reflection and of the reference reflection ($|r| \approx 1$ and $\varphi \approx 0$). In this limit the absorption coefficient can be approximated by

$$\alpha \approx \frac{4\pi\nu}{c}\frac{2\varphi}{(1 - |r|)^2 + \varphi^2}. \qquad (31)$$

Standard Gaussian error propagation then shows that the highest detectable absorption is determined by the noise of the experiment, in contrast to the dynamic range limitations imposed on the absorbance in a transmission experiment,

$$\alpha_{\max} \approx \frac{4\pi\nu}{c}\frac{2s_\varphi}{s_r^2 + s_\varphi^2}, \qquad (32)$$

where s_r is the experimental uncertainty on the measured value of $|r|$, and s_φ is the corresponding uncertainty on φ.

If we assume realistic values of $s_r = 0.01$ and $s_\varphi = 1°$ then we find $\alpha_{\max} \approx 3.7 \cdot 10^4\,\mathrm{cm}^{-1}$, well above the highest absorption coefficient in Fig. 10, and also well above the absorption coefficients normally encountered in most other nonmetallic materials.

A further complication of a reflection measurement where a separate metallic reflector is used to generate the reference signal is that the reference surface must be accurately positioned in comparison with the sample surface [158]. A small difference Δd between the position of the reference and sample reflection planes lead to an additional slope on the phase difference, $\Delta\varphi = 2\omega\Delta d/c$. In the experimental results shown in Fig. 10 this difference was found to be of the order of $20\,\mu m$, and was removed numerically before proceeding with the data analysis.

The uncertainty in the data analysis with regard to the position of the reflection planes can be somewhat reduced by introducing a second reflection interface in the experiment. This second reflection interface offers a built-in reference signal to the experiment, and hence this technique has been referred to as self-referenced reflection THz-TDS [148]. This implementation of reflection THz-TDS measurements has been extensively used for characterization of polar, and hence strongly absorbing liquids such as water [16, 145] and water-alcohol mixtures [148].

If the sample material is placed in intimate contact with a transparent window with a known index of refraction n_w, thickness d, and negligible absorption in front of the sample the ratio of the sample reflection (back side of the window) to the reference reflection (front side of the window) is

$$|r|e^{i\varphi} = \frac{t_{12}\hat{r}_{23}r_{21}}{r_{21}}e^{i2n_w d/c}, \qquad (33)$$

Figure 10 (online color at: www.lpr-journal.org) (a) Absorption coefficient, (b) index of refraction, (c) real and (d) imaginary part of the dielectric function of cesium iodide (CsI) as measured by reflection THz-TDS.

which at normal incidence can be inverted to find the index of refraction and the absorption coefficient of the sample,

$$n(\omega) = \frac{n_w \left(1 - |r'|^2\right)}{1 + |r'|^2 + 2|r'|\cos\varphi'} , \qquad (34)$$

$$\alpha(\omega) = \frac{4\pi \nu n_w}{c} \frac{-2|r'|\sin\varphi'}{1 + |r'|^2 + 2|r'|\cos\varphi'} , \qquad (35)$$

where $\varphi' = \varphi - 2n_w \omega d/c$ is the phase of the sample signal with respect to the reference signal, corrected for the accumulated phase due to propagation in the window material, and $|r'| = |r|(n_w^2 + 1)/4n_w$. Hence, a single measurement of the reflected pulse trace from the window is sufficient for a complete characterization of the complex index of refraction of the sample material. The uncertainty in the window thickness here plays the same role as the uncertainty in the reflection plane positions discussed above. The main advantage is that the window thickness can be measured independent of the experiment and with great accuracy.

3.4. Attenuated total reflection (ATR) THz-TDS

As an alternative to transmission or reflection measurements, Tanaka et al. have adapted the technique of attenuated total reflection (ATR) for use in the THz range [18, 160]. The ATR technique can be implemented conveniently with a Dove prism, cut for collinear input and output beams, as illustrated in Fig. 11. This particular geometry is from a practical viewpoint very useful since the ATR prism can be placed directly in the focal region of a transmission-type THz-TDS system, with minimal disturbance of the THz beam path.

This is obtained at the angle $\sin\theta = n_1 \sin(2\theta - \pi/2)$, where 2θ is the apex angle of the prism. In this geometry the Dove prism can be inserted in the focal region of a transmission THz-TDS system without altering the propagation direction of the incident THz beam, and thus the ATR unit can be inserted and used directly in a transmission THz-TDS system. For a silicon prism with $n_1 = 3.4177$, $\theta = 51.6°$ defines the optimum apex angle.

In this geometry the THz field is subject to total internal reflection at the upper interface of the prism. The evanescent field of the THz field penetrates into the space above the prism, and is thus sensitive to the dielectric environment in
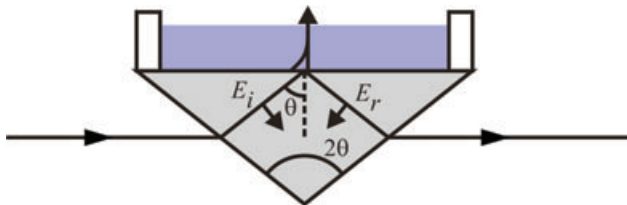
Figure 11 (online color at: www.lpr-journal.org) Silicon Dove prism for attenuated total reflection spectroscopy. The evanescent field of the *p*-polarized THz field penetrates into the liquid on top of the prism. Figure adapted from Nagai et al. [18].

this region. The ATR measurement is then carried out by measuring the reflected signal $E_r(\omega)$ from the interface in contact with the sample material and the reflected signal $E_{r'}(\omega)$ from the interface in contact with air,

$$ATR(\omega) = \left|\frac{E_r(\omega)}{E_{r'}(\omega)}\right| e^{i\Delta\varphi(\omega)} = \left|\frac{r}{r'}\right|, \qquad (36)$$

where

$$\Delta\varphi(\omega) = \arg\left(E_r(\omega)\right) - \arg\left(E_{r'}(\omega)\right) = \arg\left(\frac{r}{r'}\right) . \quad (37)$$

An example of an ATR measurement [161] performed in the Tanaka group is shown in Fig. 12 where the ATR prism has been loaded with distilled water. Figure 12a shows the reference and sample traces in the time domain, Figs. 12b and c show the phase and amplitude, respectively, of the ATR signal, and Fig. 12d shows the extracted absorption coefficient and index of refraction of water at a temperature of 293 K. The error bars indicate the standard deviation based on 5 consecutive scans.

The reference reflection coefficient r' is defined by the reflection angle and the index of refraction of the prism material, and the reflection coefficient of *p*-polarized light from the interface in contact with a sample with complex
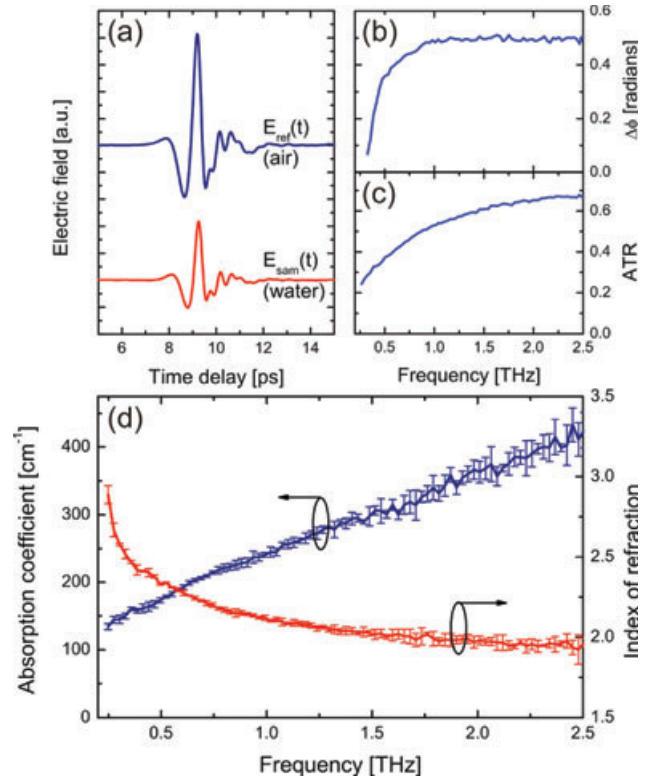
Figure 12 (online color at: www.lpr-journal.org) (a) Reference and sample pulses in an ATR measurement. Plot of (b) $\Delta\varphi(\omega)$ and (c) $ATR(\omega)$ for water at $T = 293$ K [161], and (d) the extracted absorption coefficient (blue curve) and index of refraction (red curve) of water.

index of refraction p is

$$r = \frac{n_1 \sqrt{1 - (n_1/\hat{n}_2)^2 \sin^2 \theta} - \hat{n}_2 \cos \theta}{n_1 \sqrt{1 - (n_1/\hat{n}_2)^2 \sin^2 \theta} + \hat{n}_2 \cos \theta} . \quad (38)$$

This equation has the solutions

$$\hat{n}_2^2 = \frac{B \pm \sqrt{B^2 - AB \sin^2 2\theta}}{2A \cos^2 \theta} \quad (39)$$

with $A = (r-1)^2$ and $B = (r+1)^2$. The solution with positive imaginary part is the physically meaningful one.

In the THz regime, ATR spectroscopy has been applied to studies of surface plasmons in doped semiconductor materials [162] as well as studies of liquid relaxation and vibrational dynamics, for instance water isotopes [163, 164], alcohol-water mixtures [149], and solutions of biomolecules in water [17, 165].

3.5. Comparison of sensitivity in transmission, reflection, and ATR spectroscopy

For refractive indices of the sample material lower than that of the prism material, thus still satisfying the total internal reflection condition, the sensitivity of the ATR technique can be significantly higher than that of transmission THz-TDS and reflection THz-TDS.

In Fig. 13 we show a polar plot of the measured complex quantity in different geometries for measurements on the weakly absorbing liquid heptane and the strongly absorbing liquid water. In the case of transmission we use Eq. (21), with the phase corrected for the average refractive index of the sample across the spectral range and assuming that the sample is placed between two silicon windows ($n_w = 3.4177$), for reflection we use Eq. (33), corrected for the phase acquired in a 2-mm thick silicon window and incidence angle 30 degrees [148], and Eq. (36) is used in the case of ATR with a silicon prism cut at $\theta = 51.6°$.

The different plots give an indication of the regimes where the different techniques discussed here are useful. The polar plots all show the measured quantity in the frequency range 0.1–3 THz. The small gray region near the origin in Fig. 13 indicates the minimal measurable signal, dependent on the dynamic range of the spectrometer, and the outer borderline in the diagram indicates that largest possible amplitude, depending on the window material. All measured quantities must lie within these two borders in the diagram in order to represent the optical properties of the sample. The extent of the traces in Fig. 13 gives an indication of the sensitivity of the method [18]. A large extent of the trace shows that a certain change in the optical properties of the sample leads to a large change in the measured signal. A small extent of the trace indicates that changes in the optical properties of the sample lead to a much smaller change in the measured signal.

The example of heptane in Fig. 13a shows that weakly absorbing liquids with low dispersion are best characterized with transmission THz-TDS. Here, both reflection and
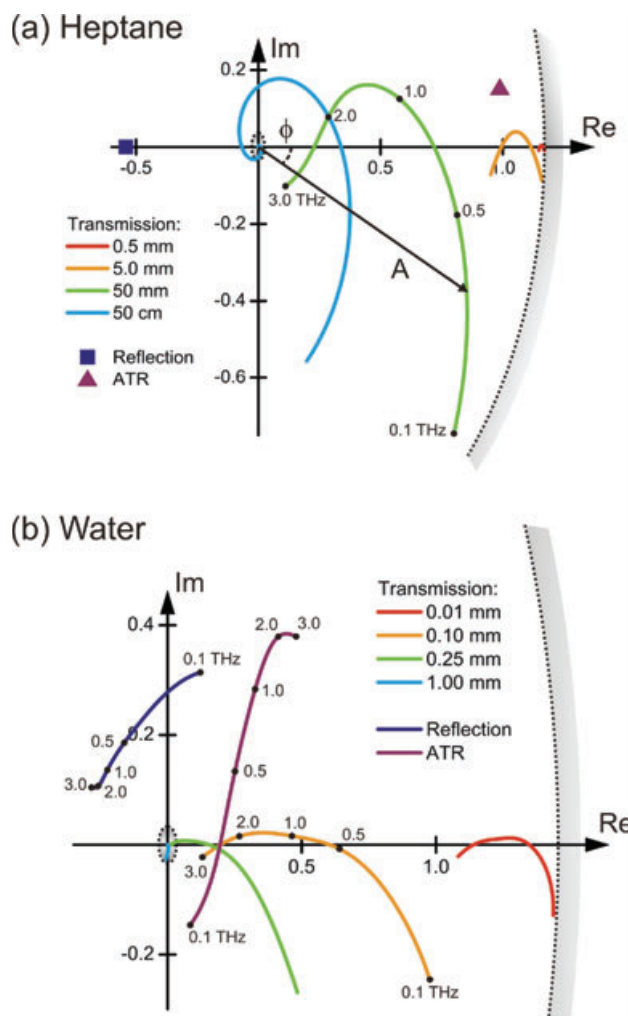
Figure 13 (online color at: www.lpr-journal.org) Polar plot of the measured transmission, ATR and reflection functions for (a) heptane (weak absorption) and (b) water (strong absorption). Figure adapted from U. Møller [161].

ATR measurements fail since the optical properties over the full spectral range result in a single point in the diagram. In contrast, strongly absorbing liquids such as water are best characterized with the ATR technique, as illustrated in Fig. 13b. It is seen that the ATR data throughout the spectral range are well separated in the diagram, whereas the high-frequency data of a reflection measurement are difficult to resolve. The diagram also indicates that the maximum thickness of a water film for transmission measurements should be somewhere near 100 μm.

4. Transient terahertz spectroscopy

It was realized quite early on that subpicosecond THz pulses that are perfectly synchronized to an optical fs pulse train open up the possibility of pump-probe measurement of nonequilibrium dynamics in the THz spectral range [166, 167]. This technique is most widely known as

time-resolved terahertz spectroscopy (TRTS) but has also been called transient THz spectroscopy, and is an extremely powerful technique for exploring the onset and evolution of ultrafast phenomena occuring at low energies on femtosecond to nanosecond time scales. This technique has recently been the subject of review on its own [167], and so we only wish to present the technique and supplement the thoroughness of this review with some recent results.

The first pioneering demonstration of TRTS technique was not quite the modern free-space technique we have today, however, many of the same principles were applied. In 1987, following over a decade of development of picosecond electrical pulses generated by femtosecond mode-locked lasers, Nuss, Auston and Capasso performed the first subpicosecond time-resolved probe of photocarriers in the semiconductor GaAs [166]. By overlaying an intrinsic GaAs sample with the electro-optic crystal, LiTaO$_3$, a subpicosecond duration electrical transient could be generated by the Cherenkov radiation induced by a portion of the fs pulse inside the LiTaO$_3$ crystal. This THz-bandwidth transient was subsequently used as a probe of the photoinduced conductivity that is perfectly synchronized to the fs excitation pulse. The field of the pulses could then be resolved by electro-optic sampling within the LiTaO$_3$ crystal for various pump-probe delay times, and so the first time-resolved full-field probe was demonstrated. With this method, the authors were able to observe directly the transfer of electrons from the low mobility L and X valleys in GaAs to the higher mobility Γ-valley on a 2–3 ps time scale following optical injection well above the bandgap.

4.1. Experiment

TRTS has since evolved into a free-space pump-probe technique, and has had a wide impact on our understanding of ultrafast phenomena, particularly in condensed matter systems such as bulk semiconductors [2, 5, 168–173] and their nanostructures [5, 7, 174–184], dielectrics [185], organic semiconductors [186–196] or semimetals [197] and correlated electron materials [7, 184, 198–200]. The power of the technique lies in mapping the dynamics of the broadband optical response functions, such as the complex optical conductivity, over THz frequencies as it evolves after photoexcitation.

The TRTS setup is much the same as the THz-TDS based on difference-frequency generation and electro-optic detection in nonlinear and electro-optic crystals, with the addition of a third pump beam to the THz generation and detection beams. Figure 14 shows a schematic of the TRTS system at DTU. The fundamental output of the laser system is split into three beams: an optical excitation beam, a THz source beam and a third sampling beam used in free-space electro-optic detection of the THz field transients. This requires two delay stages to vary the time delay between all three lines. The particular arrangement of the delay stages and their use in data acquisition has important consequences in the analysis of the data, which has been discussed in the literature [201].
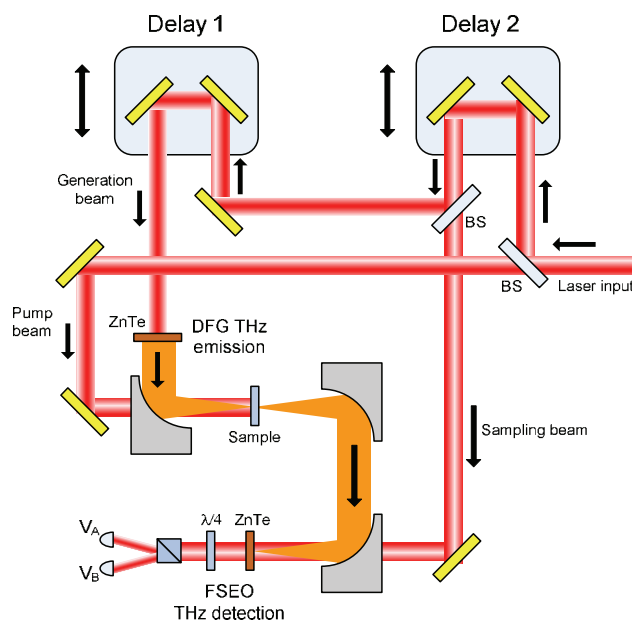
Figure 14 (online color at: www.lpr-journal.org) Schematic of the experimental setup for transient THz spectroscopy based on THz generation by optical rectification and free-space electro-optic detection.

The large diffraction-limited spot at THz frequencies (approximately 1 mm) at the sample position in the spectrometer places restrictions on the pump pulse spot size required to achieve a uniform photoexcitation, so as to avoid experimental artifacts due to spatial overlap with the frequency dependent THz spot size [168, 202]. This large spot size subsequently imposes a limit on the pulse energy for which a significant excitation can be observed in the THz response, given signal to noise considerations. Usually, this means that TRTS experiments are based on low repetition rate (kHz), femtosecond laser amplifiers providing mJ level pulse energies, although there are notable exceptions where fs oscillators are used and either sapphire lenses are used to focus to tighter spot sizes enabling a higher pump fluence [6] or the pump overlap with the THz pulse is taken into account in the data analysis [182]. These large pulse energies allow for the generation of THz pulses by difference-frequency generation in a nonlinear crystal, discussed in Sect. 2.3. For systems with long relaxation times approaching 10–100 μs, low repetition rates are required to allow the sample to relax to equilibrium before it is re-excited by the next pulse.

4.2. Data acquisition and analysis

There are two modes of data acquisition in a TRTS experiment: a 1D scan and a 2D scan so named after the number of time delays involved in the measurement. The 1D scan involves monitoring the transmission of the THz pulse electric field at only a single point in time on the THz waveform (Delay 1 fixed), usually the THz pulse peak because of signal strength, and varying the arrival time between the pump and THz pulse at the sample (Delay 2 scanned). When the

pump pulse and THz probe overlap in time at the sample, a change in transmission is observed due to pump-induced absorption or bleaching (i. e. in the case of a superconductor). This provides a detailed picture of the dynamics of the photoexcitations probed by the THz pulse averaged over the frequency bandwidth of the THz pulse, and so provides no spectral information. A full 2D scan varies both the pump-probe time delay, t_p, (Delay 2) and the delay between the THz pulse and the sampling beam (Delay 1), and so the entire THz waveform is recorded at a complete set of times surrounding the photoexcitation event. In the scheme shown in Fig. 14 where Delay 1 scans the THz source beam against the pump pulse as well as the sampling pulse, all points in the acquired THz waveform have experienced the same pump-probe time delay. If however, the pump beam was scanned in time with respect to both the sampling and the THz beams, then each point in the THz waveform would have experienced a slightly different pump-probe time delay. In this case, for subsequent Fourier analysis of the waveforms, a numerical projection is required onto a constant pump probe time axis.

This 2D data matrix provides the most information, both dynamic and spectral, but also takes much longer to acquire and so for practical reasons the dynamics are often described by 1D scans when applicable. Pump-beam modulation is typically used in both methods, where an optical chopper can be used to modulate the excitation beam so that either a differential transmission $-\Delta T(t_p) = T_{ref} - T_{pump}(t_p)$ or a differential waveform $-\Delta E(t, t_p) = E_{ref}(t) - E_{pump}(t, t_p)$ is recorded. This has the benefit of zero background detection and enhanced sensitivity. Recently, a double-modulation scheme was employed by Golde et al. [203] and Iwaszczuk et al. [204] so that both a reference and a differential THz waveform could be acquired simultaneously, eliminating the influence of slow drift of laser power and alignment. Usually, TRTS is performed in normal incidence transmission geometry, although there have been examples of reflection geometries as well where dense laser-heated Al plasma were recently investigated [205].

As mentioned previously, THz pulses are particularly sensitive probes to intraband transitions, for example photocarriers in the conduction (and valence) band of a semiconductor. For a thin (thickness $d \ll \lambda$) film sample on a nonconducting, semi-infinite substrate, which is a good approximation for a photoexcited layer in a bulk semiconductor or a photoactive film on a nonabsorbing substrate, there is a useful analytical approximation to extract the dynamic optical functions [206]. The complex transmission coefficient $\hat{T}(\omega, t_p)$ in this case is given by

$$\hat{T}(\omega, t_p) = |T| e^{i\varphi} = \frac{\hat{E}_p(\omega, t_p)}{\hat{E}_{ref}(\omega)}$$
$$= \frac{n+1}{n+1+Z_0 \hat{\sigma}(\omega, t_p) d}, \qquad (40)$$

where $E_p(\omega, t_p) = E_{ref}(\omega) + \Delta E(\omega, t_p)$ is the THz pulse with photoexcitation, Z_0 is the impedance of free space (377 Ω) and n is the index of refraction of the substrate at THz

wavelengths, assumed here to be frequency independent and purely real (absorption free). We note that this approximation is valid for a single conducting film, and in the case of a multilayer sample an alternative formulation can be found through a transfer matrix method [184]. Technically, the carrier distribution follows Beer's law as an exponential decay into the sample and so should the nonuniform carrier density should be taken into account. However, it has been shown that the slab approximation leads to $< 5\%$ error for skin depths less than 3 micrometers [168], which is often the case for strongly absorbing samples such as GaAs.

The real and imaginary conductivity can then be found by inversion of Eq. (40)

$$\sigma_1(\omega, t_p) = \frac{n+1}{Z_0 d} \left(\frac{1}{|T|} \cos\varphi + 1 \right), \qquad (41)$$

$$\sigma_2(\omega, t_p) = -\frac{n+1}{Z_0 d} \frac{1}{|T|} \sin\varphi. \qquad (42)$$

An example of a 2D differential THz transmission $-\Delta E(t, t_p)$ map is shown in Fig. 15a, for a bulk semi-insulating [100]-cut GaAs crystal photoexcited with a 400 nm, 45 fs pump pulse at a fluence of 30 μJ/cm^2. GaAs was the first bulk semiconductor to be characterized with TRTS, and has since been thoroughly examined by several groups [2, 7, 168, 173], and so it has become a standard for calibration of TRTS experiments. The differential transmission of THz radiation in a semiconductor is proportional to the product of the charge carrier density and the mobility of these carriers. It is important here to note that TRTS cannot distinguish between electrons or holes, however in GaAs the heavy hole effective mass ($m_h = 0.57m_0$) is approximately 10 times larger than the electron mass ($m_e = 0.067m_0$) and so the electronic contribution to the conductivity dominates. The 400 nm pump excites carriers high up in the band of GaAs, causing a significant carrier population in the side X- and L- valleys in the band structure. The effective masses of carriers occupying these valleys (m_X and $m_L = 0.85m_0$) are much larger than the central Γ valley, and so the electron mobilities are lower. This difference in electron mobility allows intervalley scattering to be observed directly with TRTS in a semiconductor by a delayed risetime in the differential THz transmission, and was shown in GaAs to take up to 2–3 ps at room temperature depending on the excess energy [166, 207].

In a bulk photoexcited semiconductor, the conceptually simple Drude model provides a good phenomenological understanding of the conduction mechanism. Here, the conductivity is given as

$$\tilde{\sigma}(\omega) = \frac{N e^2 \tau}{m^*} \frac{1}{1 - i \omega \tau}, \qquad (43)$$

where N is the carrier density, e is the unit charge, τ is the Drude momentum scattering time and m^* is the carrier effective mass. If the probe frequency is in the limit $\omega\tau \ll 1$, $\tilde{\sigma}(\omega) \approx \sigma_1 \gg \sigma_2$, and the differential transmission from a
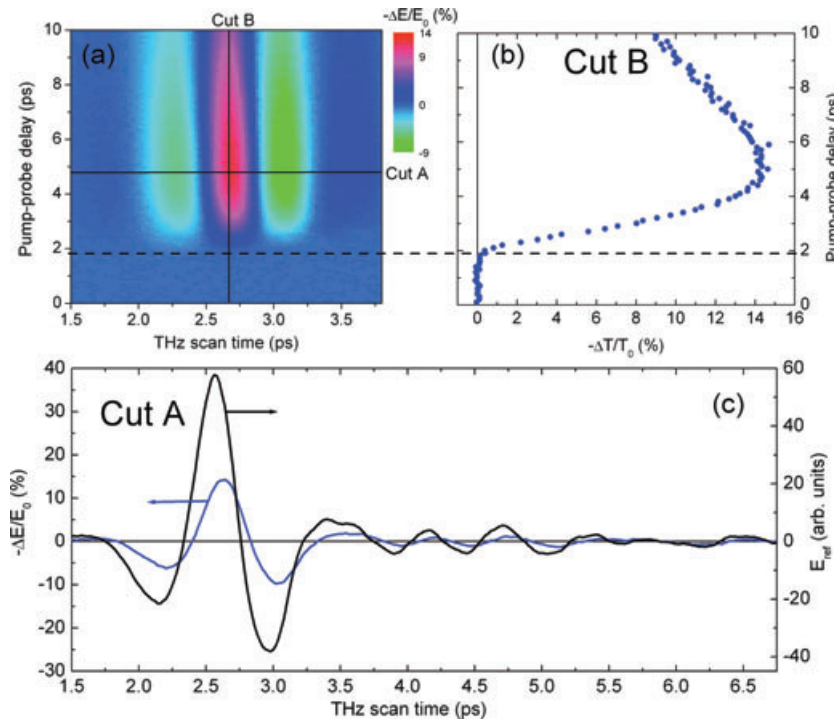
Figure 15 (online color at: www.lpr-journal.org) (a) Two-dimensional differential THz waveform map for GaAs under 400 nm photoexcitation at a fluence of $30\,\mu J/cm^2$. (b) Differential THz waveform slice corresponding to Cut B in (a). (c) Differential THz pulse $-\Delta E(t, t_p = 2.8\,\text{ps})$ (blue line) corresponding to Cut A in (a) and reference THz pulse $E_{\text{ref}}(t)$ (black line).

1D scan is related to the conductivity by

$$\sigma_1(t_p) = \frac{n+1}{Z_0 d}\left[-\Delta T(t_p)/T_0\right]\left[\frac{1}{1+\Delta T(t_p)/T_0}\right], \quad (44)$$

which in the limit of $-\Delta T(t_p)/T_0 \ll 1$ reduces to

$$\sigma_1(t_p) = N(t_p)e\mu(t_p) = \frac{n+1}{Z_0 d}\left[-\Delta T(t_p)/T_0\right]. \quad (45)$$

Within the above-mentioned assumptions, Eq. (45) provides a method of determining the carrier mobility μ of a material from the peak differential transmission provided the quantum efficiency and pump fluence F is known. The carrier density can be estimated from the pump fluence by

$$N = \frac{\eta(1-R)F\lambda_p}{dhc}, \quad (46)$$

where R is the reflection coefficient at the pump wavelength λ_p. In the case of organic systems where the quantum efficiency of mobile carrier production is a number of some controversy, it is the product $\eta\mu$ that is reported [187, 189]. We also note that this requires there to be no significant loss mechanisms for mobile charges occuring on time scales shorter than the risetime of the differential signal, typically 500 fs, otherwise the depletion of carriers is erroneously factored into the quantum efficiency.

In the limit of a pure amplitude change with no phase change of the pulse with respect to the reference pulse then $\varphi \approx 0$. Thus, by Eqs. (41) and (42), $\sigma_2 \approx 0$ and the response is purely real. As shown above, the one-dimensional scans can be quantitatively related to the conductivity dynamics, as monitoring the dynamics of any point in the THz waveform will provide equivalent information as any other point in the waveform. Such a scan is represented by Fig. 15b, shown as Cut B in the $-\Delta E(t, t_p)$ map in (a). However, if there is a significant phase change, then it is no longer sufficient to monitor one point in the THz waveform, and then one must be careful that a time-dependent phase change does not mimic a time-dependent amplitude change. For large dynamic phase changes, full 2D scans must be performed. Figure 15c shows both a horizontal Cut A in the $-\Delta E(t, t_p)$ map (blue), corresponding to a fixed pump-probe delay time, and the reference THz scan, $E_{\text{ref}}(t)$ taken in the absence of an excitation. The phase shift of the differential scan with respect to the reference scan is evident, meaning that there is a significant imaginary response to the complex conductivity and one cannot rely on 1D scans like that in Fig. 15b to represent true conductivity dynamics.

For full frequency-resolved analysis in the thin-film approximation, Eqns (41) and (42) can be used following Fourier transformation of the time domain traces. In the vicinity of $t_P = 0$, where the THz transmission changes rapidly, any single-variable Fourier transformation introduces artifacts that must be treated with more advanced time-domain numerical [208] or analytical [209] methods. These methods necessitate an *a priori* model of the electrodynamics for the system, for example the Drude model, which has parameters that can be varied to fit the experimental data. An alternative treatment has also been proposed using two-dimensional Fourier transforms, which can avoid frequency mixing effects provided $|\Delta E/E_{\text{ref}}|$ remains small [201]. For nonlinear behavior observed in high field THz experiments, numerical finite-difference time domain analysis is currently the only recourse.
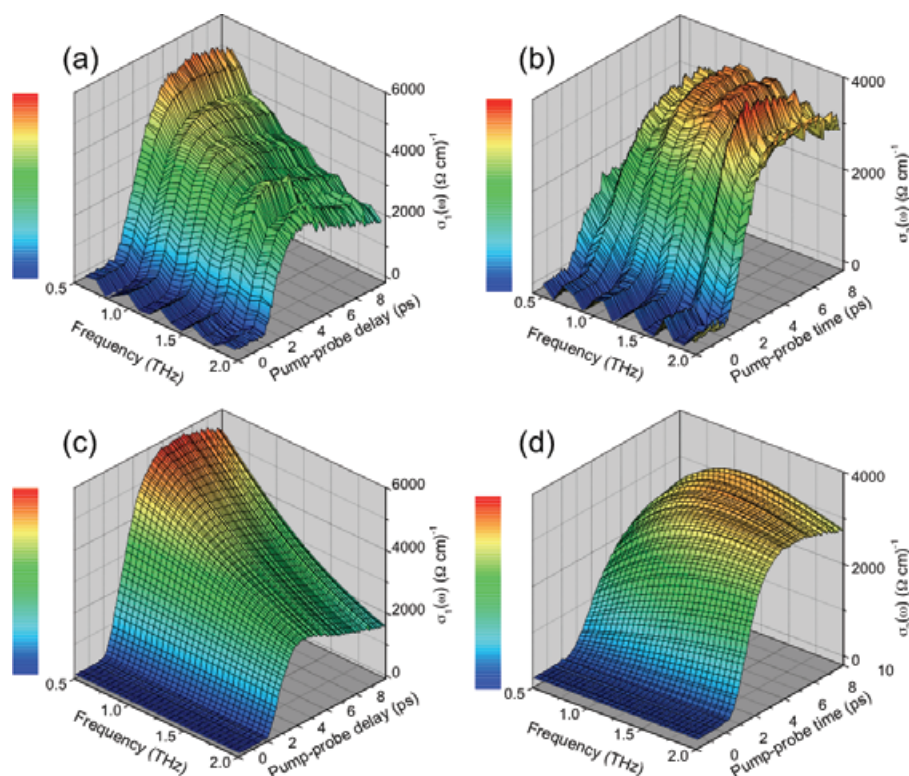
Figure 16 (online color at: www.lpr-journal.org) Two-dimensional evolution of the (a) real and (b) imaginary part of the frequency dependent complex conductivity of GaAs following 400 nm photoexcitation, extracted from the 2D differential plot in Fig. 13. Time-dependent Drude fits for (a) and (b) are shown in (c) and (d), respectively.

4.3. Transient photoconductivity in bulk GaAs

For the case of GaAs photoexcited with 400 nm light (well above its bandgap), intervalley scattering into low mobility satellite valleys delays the onset of the peak photoconductivity by several picoseconds. This slow onset al.lows Fourier transform methods to be used without concern for frequency mixing artifacts [168]. Figures 16a and b show the extracted real and imaginary components of the conductivity from the $-\Delta E(t, t_p)$ map shown in Fig. 15a and a reference pulse map (not shown) taken at negative pump-probe delay times. Equations (41) and (42) are used to relate the complex transmission function to the complex conductivity for all pump-probe delay times. Global fits to the Drude model of band conduction are shown in Fig. 16c and d, given by Eqn. (43) with plasma frequency, $\omega_p^2 = N e^2 / \varepsilon_0 m^*$. One can see that even for early pump-probe delay times, the Drude model provides an excellent description of the experimental data. The extracted Drude parameters, the plasma frequency ω_p and the momentum scattering time τ, from these fits are shown in Fig. 17a and b, respectively. Photoexcitation of GaAs at 400 nm (3.1 eV) supplies enough excess energy to the electron to allow population of the X and L satellite valleys. Subsequent intervalley transfer back into the lower effective mass Γ-valley takes time due to the lower density of states of the final state, and this has been shown to last several picoseconds. The dynamics of this transfer is reflected in the delayed rise of the plasma frequency ω_p, increasing slowly over more than 2 ps due to a time-dependent decrease in the effective mass. The scattering time τ, however, is shown to increase steadily over a much longer time scale beginning as low as 15 fs immediately following pho-

toexcitation to 150 fs after 8 ps. This has also been observed in previous measurements [169], and is attributed to the hot LO phonon population created by highly energetic electrons as they emit large k-vector phonons via intervalley scattering in their transfer from satellite valleys to the Γ-valley, where they also relax primarily by LO phonon emission. This large population of hot phonons serves as a significant source of scattering that lowers the effective momentum relaxation time τ. The relaxation to the band minimum is hindered due to the nonequilibrium phonon population as electrons are likely to absorb as well as emit a phonon. This extends carrier relaxation to several picoseconds that is reflected in the dynamics of τ.

Figure 17c shows the dynamics of the dc conductivity given by $\sigma_{dc} = \omega_p^2 \varepsilon_0 \tau$, which illustrates the several picosecond delay of GaAs in reaching the maximum conductivity after photoexcitation by 400 nm light. It is further interesting to note that while the maximum σ_{DC} is obtained 5 ps after excitation, the 1D differential transmission dynamics reaches a peak only 3 ps after excitation. This illustrates the danger of assigning the dynamics of the $-\Delta T(t_p)/T_0$ scans to that of $\sigma_{DC}(t_p)$ when there is a significant time-dependent phase shift of the THz pulse. Indeed close inspection of the $\sigma_1(\omega, t_p)$ map in Fig. 16a and the Drude fits in (c) shows the dynamics of the conductivity depend specifically on the probe frequency. The differential transmission is effectively a frequency-weighted average of these dynamics, and so when conclusions are drawn solely from 1D scans they must be justified by full 2D scans.

This illustrates the power of TRTS in characterizing the picosecond kinetics of transport properties in semiconductors, where the effective mass, carrier density and scattering
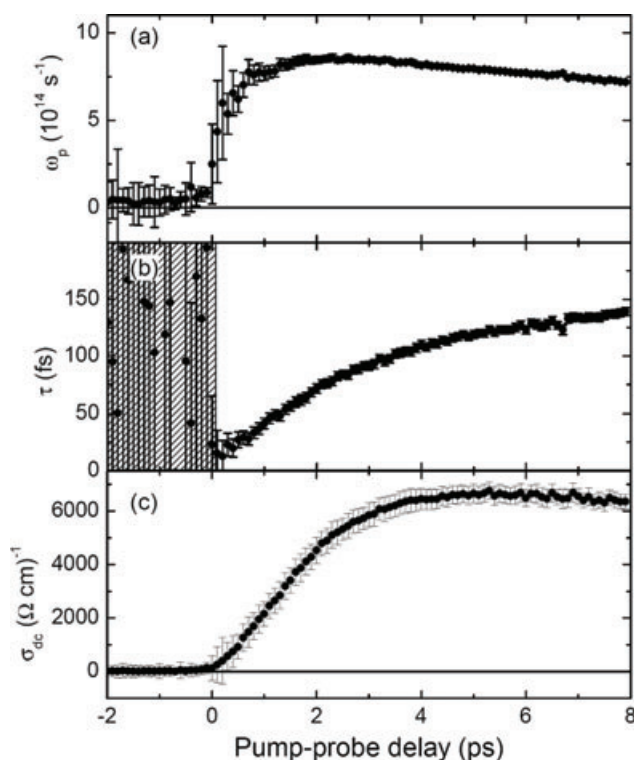
Figure 17 The dynamics of the (a) plasma frequency, (b) momentum scattering time and (c) dc conductivity given by $\sigma_{dc} = \omega_p^2 \varepsilon_0 \tau$ for GaAs photoexcited with 400 nm at a fluence of 30 μJ/cm^2.

rates can all be dynamic quantities. Picosecond photoconductive techniques measure the product of the carrier density and mobility so it is difficult to deconvolute these quantities, and must rely on other techniques to elucidate the individual contributions.

The above section shows how amazingly well the Drude model can describe the experimental data, despite the lack of a full band structure or an energy-dependent scattering rate being taken into account. In some situations, however, one has to turn to a full microscopic many-body theory; in particular for strong THz fields, exceeding 10 kV/cm where nonlinear optical effects can be observed [210–213]. It was recently pointed out that in such cases ponderomotive contributions, which arise from charged particles in a harmonic electromagnetic field, have to be considered to fully describe the experimental data [9, 203].

Deviations in a Drude response can also occur for dilute isovalent doping. Recently Cooke et al. used TRTS to determine the effects of isovalent doping in GaAs to form the ternary nitride and bismide compounds GaAs$_{1-x}$N$_x$ and GaAs$_{1-y}$Bi$_y$ [172]. These dopants are highly interesting due to the large bandgap-bowing effects induced by alloying to a small degree ($x, y < 2\%$), reducing the optical bandgap by several hundred meV, into the telecom bands. The authors demonstrated that the electron mobility of the bismide alloy remains relatively unchanged with isovalent doping to concentrations less than 1.4%. The nitride films, how-

ever, showed non-Drude conductivity with reduced electron mobility upon doping. This can be explained by the band bowing in the nitrides being due to a resonant interaction of a nitrogen state with the bottom of the conduction band, whereas in the bismides the interaction is with the valence band. Thus, the nitrides contribute heavily to impurity scattering in the conduction band and cluster potential-induced carrier localization manifesting a suppression of the low-frequency conductivity spectrum.

5. Scientific applications for static THz-TDS

### 5.1. Static THz-TDS of solid-state materials

Already in the early days of far-infrared spectroscopy it was realized that the THz range hosts a wealth of optical resonances in molecular crystals. As an example, the classical textbook from Möller and Rothschild [46] devoted a whole chapter to the description of lattice modes in polyatomic crystals, including a thorough discussion of the phonon mode at 2.2 THz in polyethylene (PE). In recent years the spectroscopic features in polyatomic crystals, and in particular crystals of organic molecules, have been subject to renewed interest. A major driving force behind this renewed interest has been the exciting potential of using THz radiation for stand-off chemical recognition of dangerous (explosive or poisonous) or illicit chemicals, made feasible by the new generation of compact and portable THz-TDS systems. Another more pragmatic driving force has been that the THz-TDS field to a large extent has grown out of the semiconductor research field, and therefore the knowledge base of far-infrared vibrational modes in molecular crystals had to be built up in the early years of applied THz-TDS.

In the following we will discuss the current understanding of the origin of the absorption features found in the THz range in many single-crystal, microcrystalline, and powder samples of organic molecules.

Covalent bonds, and in some situations also hydrogen bonds, are responsible for the intramolecular arrangement of the constituent atoms of a molecule. The intermolecular forces that hold the molecules together in the crystal lattice are typically hydrogen bonds or weaker forces such as van der Waals, stacking, dipole-dipole, or dispersion interactions. The detailed and complicated interplay between the intra- and intermolecular forces forms the THz absorption spectrum of the molecular crystal, whereas the higher-frequency modes are typically determined mainly by the intramolecular forces.

In the general case, for a crystal with N atoms in the unit cell there will be $3N - 3$ vibrational modes of the crystal with frequencies ranging from the low THz region to the near-infrared.

Although from a theoretical point of view there is no formal distinction between these various modes, it is in some cases instructive to make the distinction between internal modes of predominantly intramolecular nature and external modes of predominantly intermolecular nature. If we for the moment assume rigid molecules with no internal vibrations
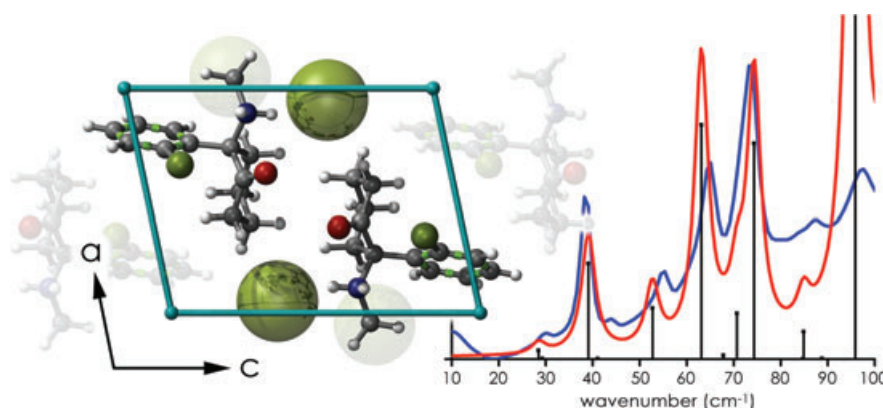
Figure 18 (online color at: www.lpr-journal.org) Comparison of the best-fit PW91/6-31G(d,p) simulation (red trace, black impulses) to the cryogenic experimental spectrum (blue trace) of (S)-(+)-ketamine hydrochloride. Adapted from Hakey et al. [231]

then the number of eigenmodes of the crystal is determined by the number of molecules Z in the unit cell, with a total of $6Z - 3$ modes, of which $3Z$ are translational modes and $3Z - 3$ are librational modes. These external modes will be located at low frequencies, whereas the intramolecular modes are found at higher frequencies.

Certain weakly bound molecular crystals are relatively well described by this distinction between internal and external modes [214]. However, in strongly bound crystals where the internal and intramolecular forces are comparable, the distinction between internal and external modes becomes less obvious, with strong mixing between intra- and intermolecular motion [215]. For this and other reasons, the calculation of the low-frequency vibrational spectrum of molecular crystals is a formidable theoretical and numerical task. In recent few years there has been a high activity and associated progress on the understanding of the nature of the distinct absorption bands observed in the THz range in solid-state materials. High-performance parallel computing with advanced modelling tools based on either density-functional theory (DFT), density-functional perturbation theory (DFPT) or molecular dynamics (MD), taking the periodic structure of the crystal lattice into account, is required for reliable prediction of the lowest vibrational modes in molecular crystals.

The most commonly used programs for the calculation of THz properties of solid-state materials are Gaussian [142], Dmol^3 [216], Crystal [65], CPMD [127], Castep [128, 217, 218], VASP [129], and CHARMM [219].

Siegrist et al. [220] investigated different crystalline forms of trianiline, and found that in contrast to the mid-IR range, the THz range spectral patterns depended strongly on the crystallisation, which the authors concluded was due to differences in the β-sheet structure and the hydration.

The Korter group has published an impressive series of papers describing in detail the THz-range vibrational spectra of a wide range of molecular crystals, with experimental spectra recorded on microcrystalline powders of the material. Their studies include energetic materials such as HMX (octahydro-1,3,5,7-tetranitro-1,3,5,7-tetrazocine) [221], PETN (pentaerythritol tetranitrate) [222], RDX (cyclotrimethylenetrinitramine) [223], and TATP (triacetone triperoxide, 3,3,6,6,9,9,12,12-octamethyl-1,2,4,5, 7,8-hexoxonane) [224], illicit or controlled substances

such as MDMA (3,4-methylenedioxymethamphetamine hydrochloride, ecstasy) [225], methamphetamine hydrochloride [226], ephedrine [227], and PCP (phencyclidine hydrochloride, or angel dust) [228]. In addition, material of biological relevance, including serine and cysteine [229], biotin and lactose monohydrate [13], and chiral (L) and (DL) serine [230], have been studied.

As an example of the accuracy of density-functional theory approach to the calculation of the THz spectra of molecular crystals, Fig. 18 shows the crystal structure (left) and (right) the measured absorption spectrum at liquid-nitrogen temperature (blue curve) of microcrystalline powder of S-(+)-ketamine hydrochloride, together with predicted vibrational frequencies (black, vertical bars) and simulated absorption spectrum with a $3.5 \, \text{cm}^{-1}$ FWHM Lorentzian linewidth [231].

Saito et al. have published a series of simulations of the vibrational spectrum of molecules in crystalline environments. They showed that the simulated THz spectrum of crystalline salicylic acid [232] has lattice modes at the lowest frequencies, intermolecular modes at intermediate frequencies, and intramolecular modes at the highest THz frequencies. They performed similar simulations on the organic salt DAST [233] with emphasis on the difference between isolated-molecule and solid-state simulation, and on lactose monohydrate with special emphasis on the role of crystal water [234], and on beta-D-glucopuranose [235].

Recently Zhang et al. went beyond the harmonic approximation which is otherwise commonly used for the determination of vibrational frequencies, in order to shed light on interactions in large, van-der-Waals-bonded biomolecular systems. Using a vibrational self-consistent field methodology, they compared simulated and measured THz spectra of different crystalline L-analine and L-valine (VA) dipeptide nanotube systems [15].

Here, we show examples of weakly bound molecular crystals and strongly bound crystals. As an example of a weakly bound molecular crystal structure, Fig. 19 shows the molecular and crystal structure of all-*trans* retinal. All-*trans* retinal forms a monoclinic crystal with space group $P2_1/n$ and 4 molecules in the unit cell [236]. The crystal structure consists of the linear molecules alternating oriented and held together by van der Waals forces. Other isomers of retinal, such as the 13-*cis* and 9-*cis* retinal, also form van der Waals
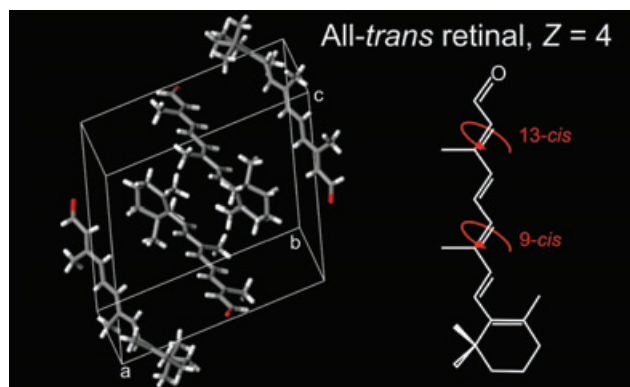
Figure 19 (online color at: www.lpr-journal.org) Molecular and crystal structure of all-*trans* retinal. The 9-*cis* and 13-*cis* isomers are obtained by rotation around the indicated bonds. The crystal structure is held together by van der Waals interactions.
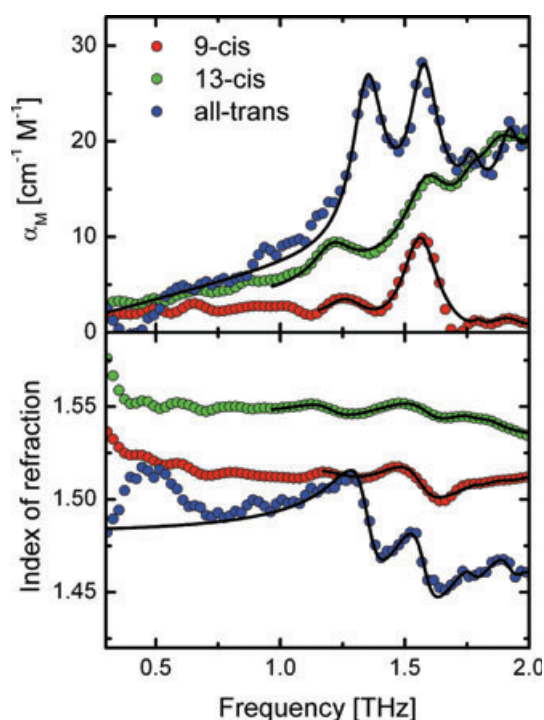
Figure 20 (online color at: www.lpr-journal.org) (a) Molar absorption coefficient and (b) index of refraction of all-*trans*, 9-*cis*, and 13-*cis* retinal in PE. Figure adapted from Walther et al. [214].

bonded crystals [237, 238]. The arrows superimposed on the chemical structure of all-*trans* retinal in Fig. 19 indicate the 9-*cis* and 13-*cis* isomerizations.

Figure 20 shows the molar absorption coefficient and index of refraction of all-*trans* (blue symbols), 9-*cis* (red symbols), and 13-*cis* (green symbols) retinal, recorded by THz-TDS with the sample material prepared as pellets composed of finely ground microcrystalline retinal powder carefully mixed with a polyethylene (PE) filler at a mass ratio of 1:1 and compressed into a pellet in a hydraulic press, using

a pressure of $4 \cdot 10^7$ Pa (corresponding to $400\,\mathrm{kg/cm^2}$) [214]. The sample pellets were kept at a nominal temperature of 10 K in a closed-cycle cryostat during the measurements.

The spectra of all three isomers of the retinal molecule reveal distinct absorption features. The full lines are fits to the experimental data by the Lorentz oscillator model,

$$\varepsilon(\nu) = \varepsilon_\infty + \sum_{j=1}^{N} \frac{S_j \nu_j}{\nu_j^2 - \nu^2 - \mathrm{i}\,\nu\Gamma_j} = (n + \mathrm{i}\,\kappa)^2, \qquad (47)$$

where the N oscillators have resonance frequencies ν_j, damping rates Γ_j and oscillator strengths S_j.

The possibility of a simultaneous fit of both absorption coefficient and index of refraction allows an accurate fitting even to relatively weak spectral signatures in the experimental data [214]. This shows an example of the importance of the capability of THz-TDS to measure both of these quantities directly.

Isolated-molecule calculations based on density-functional theory (DFT) [239] have shown good agreement with observed spectral features in all-*trans* retinal in Fig. 20. These DFT calculations suggested that the low-frequency vibrations are collective skeletal torsional or twisting modes delocalized over a large fraction of the retinal molecule, but still confined to certain fractions of the polyene chain or the ring structure. Comparison of the absorption spectra of the three different isomers of retinal shown in Fig. 20 gives the possibility of assigning the different vibrational frequencies to vibrations confined to specific regions of the retinal molecules [214].

As an example of a strongly bound molecular crystal, Fig. 21 shows the molecular and crystal structure of the hydrogen-bonded crystal of sucrose. Sucrose crystallizes in the $P2_1$ space group with 2 molecules in the unit cell [240]. In contrast to retinal, as discussed above, the sucrose crystal is held together by a strong, intermolecular hydrogen-bond network, as indicated by the blue connections in Fig. 21. The hydrogen-bond network results in strong interaction between the molecules in the crystal lattice, and thus a classification of vibrational modes as either inter- or intramolecular becomes very difficult.
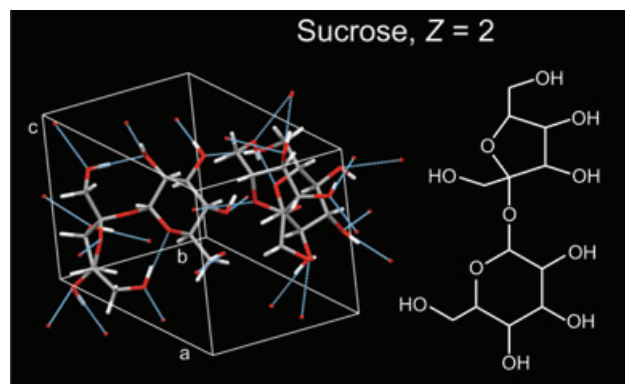
Figure 21 (online color at: www.lpr-journal.org) Molecular and crystal structure of sucrose. The blue, dashed lines indicate intra- and intermolecular hydrogen bonds.
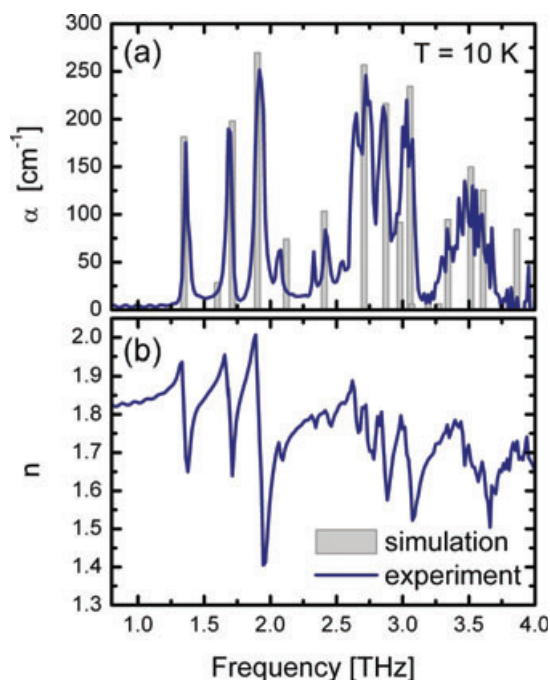
Figure 22 (online color at: www.lpr-journal.org) (a) Absorption coefficient and (b) index of refraction of sucrose. Gray bars indicate vibrational frequencies predicted by solid-state DFPT.

The solid, blue curve in Fig. 22 shows the measured absorption spectrum of microcrystalline sucrose [12], recorded on two different pellets pressed of finely ground sucrose powder mixed with different ratios of PE filler to adjust the absorption to match the dynamic range of the spectrometer over the full bandwidth. The measurements were carried out at 10 K nominal sample temperature.

Whereas the absorption signatures of retinal, discussed above, could be assigned to certain vibrational modes of the molecular structure, single-molecule calculations of the vibrational spectrum of sucrose fail completely to reproduce the observed spectral signatures of sucrose. The bars shown on top of the experimental data in Fig. 22 represent the calculated vibrational frequencies and intensities of the sucrose crystal structure [215], using density functional perturbation theory (DFPT) as implemented in the software package Castep [217, 218].

The comparison between experimentally recorded THz absorption spectra and simulated ones is only possible if the experimental spectra actually reveal all absorption lines of the sample material with high fidelity. Similar to FTIR spectroscopy, the spectral resolution Δf of a THz-TDS experiment is determined by the free scanning range T of the THz signal, $\Delta f = 1/T$. A 68-ps scan range as used in for the recording of the spectrum in Fig. 22 thus results in a frequency resolution of 15 GHz. Hence, in order to obtain a high spectral resolution it is important to be able to record the undistorted shape of the THz transient over a wide temporal window. Multiple reflections in the setup, and particularly in the sample material itself, may severely reduce the useful temporal window of a THz-TDS experiment or call for sophisticated data extraction algorithms [153, 154, 241].

Laman et al. recently explored the use of parallel-plate waveguides (PPWG) for sensitive high-resolution THz spectroscopy [242]. The development of the parallel-plate waveguide for THz frequencies has overcome some of the problems associated with the recording of absorption spectra with high spectral resolution. The development of the PPWG as a useful spectroscopic tool for the THz region was pioneered by Grischkowsky et al. [39, 243–247] and Mittleman et al. [149, 248, 250] In the following we will discuss the relevance of the PPWG for sensitive spectroscopy with high spectral resolution.

The PPWG geometry for spectroscopy is compared with that of conventional transmission spectroscopy in Fig. 23.
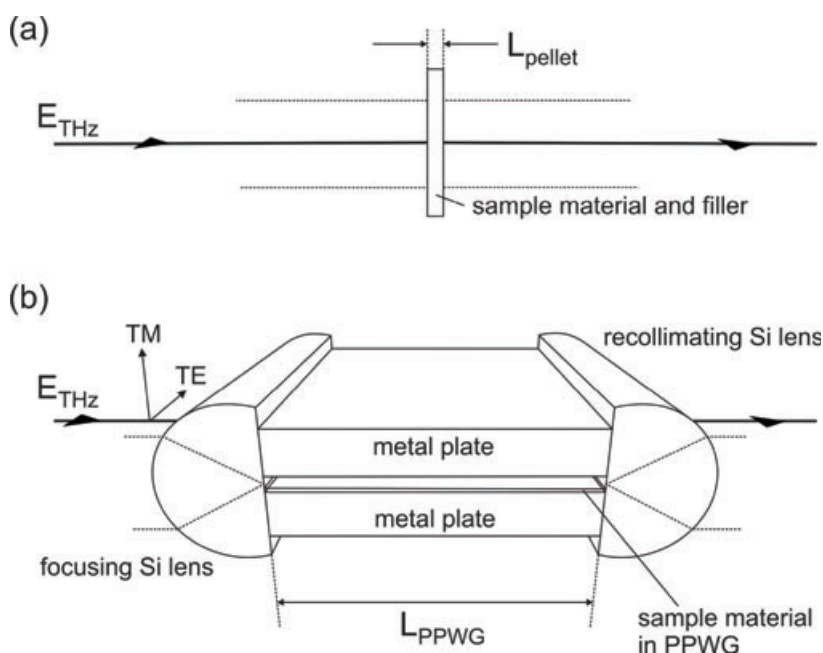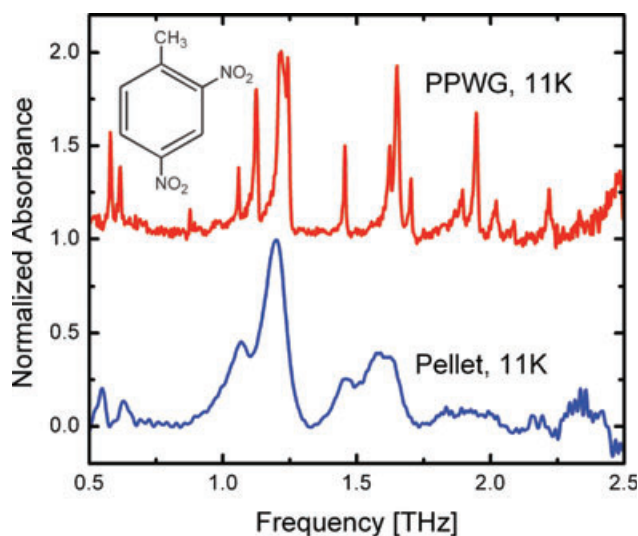

Figure 23 (a) THz-TDS on a pellet of thickness L_{pellet} and (b) THz-TDS in a parallel-plate waveguide (PPWG) of length L_{PPWG}. The THz field can be either TM or TE-polarized in each case.

The PPWG typically offers several centimeter interaction length L_{PPWG} between the THz field and the sample material, thus allowing a wide, distortion-free temporal window to be recorded. For a sample of thickness L and index of refraction n the first reflection appears at a time $\delta t \approx 2nL/c$ after the main pulse. Whereas the spectral resolution of a measurement on a free-standing pellet may be of the order of 0.05-0.1 THz for a sample of $L_{pellet} = 1$ mm thickness, the scan range made possible by the long interaction region in the PPWG allows an undisturbed spectral resolution of a few GHz (7.5 GHz for a 2-cm PPWG).

The lowest TM-mode (electric field lines perpendicular to the metal plates) of the PPWG has low propagation loss, in principle limited only by resistive losses in the surface layer of the metal plates [247]. Since there is no low-frequency cutoff of the lowest-order TM mode, the propagation is virtually dispersionless until the onset of the first higher-order mode at the frequency $f_c = c/2dn_{eff}$. There is little mode coupling in the PPWG, so even at frequencies well above the onset of higher-order modes distortion-free propagation is possible if the waveguide is excited in its fundamental mode.

The low-loss, dispersionless propagation characteristics of the PPWG have sparked significant interest in its use for spectroscopy in the THz region [38, 242, 246, 248, 251–258].

Figure 24 shows a direct comparison of the absorption spectrum of microcrystalline 2,4-dinitrotoluene recorded at a temperature of 11 K, published by Laman et al. [242]. The blue trace shows the absorption spectrum of a pressed pellet of a finely ground powder of the material, and the red trace shows the absorption spectrum of the same material, crystallized from solution on one of the plates of a PPWG. As is

clear from this comparison, the spectral features revealed by waveguide spectroscopy are much sharper and more well defined than those recorded at the same temperature on a thin pellet of the same material. In addition to the increased spectral resolution offered by the PPWG, other factors may influence the sharp appearance of the measured resonances. First, the crystallization from the liquid phase directly onto one of the plates in the PPWG will for some materials result in a better crystal quality than can be obtained in a microcrystalline powder. This could result in less broadening due to sample inhomogeneities arising from the large surface area of the powder. Secondly, the cold metal surface of the PPWG is in intimate contact with the thin layer of sample material, ensuring a uniform, cold temperature of the sample. In the case of a pressed pellet, the low thermal conductivity of the sample material and the small physical contact with the cold finger of the cryostat may prevent the sample from reaching the same low temperature as the cold finger. This will add a certain amount of thermal broadening to the resonances.

5.2. THz-TDS of water and aqueous solutions

Liquids form another class of condensed matter that has been studied extensively with THz spectroscopy. In contrast to a crystalline material, where long-range order determines its THz dielectric properties, the THz spectrum of a liquid is dominated by relaxation of either permanent dipoles in polar liquids (such as water) or collision-induced dipole moments in nonpolar liquids such as benzene, carbon tetrachloride, and cyclohexane [259–261]. The process of relaxation (or reorientation) of dipoles in liquids is important from a chemical and biological perspective since such relaxational processes on the femtosecond to picosecond time scale influence the rate of chemical reactions occurring in the liquid [262,263]. The vast majority of chemical reactions important for biological processes occur in an aqueous environment, and for that reason, most THz spectroscopic studies of liquids have been focused on water and aqueous solutions of salts, sugars and lower alcohols, as will be discussed below. A number of important studies of the THz-frequency dielectric properties of hydrated proteins and the relation to structure and function of the proteins have been performed, particularly by the Markelz group [19, 21, 264–268] and by the Havenith group [266, 269–272].

The accurate dielectric spectrum of water in the THz range at room temperature has been established by the Keiding group [145] and by the Schmuttenmaer group [146]. The general appearance of the room-temperature water spectrum at THz frequencies is shown in Fig. 8. In the frequency range from the low MHz range and up to a few THz the water spectrum is well described by two parallel Debye-type relaxational processes,

$$\varepsilon(\omega) = \varepsilon_\infty + \frac{\Delta\varepsilon_1}{1 - i\,\omega\tau_1} + \frac{\Delta\varepsilon_2}{1 - i\,\omega\tau}, \qquad (48)$$

where $\tau_1 \approx 8$ ps and $\tau_2 \approx 100 - 300$ fs are the relaxational time constants of the two processes, and $\Delta\varepsilon_1 \approx 70$ and $\Delta\varepsilon_2 \approx$

Figure 24 (online color at: www.lpr-journal.org) Normalized absorbance of 2,4-dinitrotoluene (2,4-DNT) as measured with the sample material crystallized in a parallel-plate waveguide (PPWG, upper red trace) and with identical sample material finely ground and pressed to a pellet, and measured with free-space THz-TDS (lower blue trace). Figure adapted from Laman et al. [242].

2 are the relaxational strengths of the two processes (values are given for room temperature).

The extraction of the parameters in Eq. (48) for the exact spectral shape of the dielectric response of liquid water is critically dependent on the spectral range used in the fitting procedure. The slow response $(\Delta\varepsilon_1, \tau_1)$ is best fitted to low-frequency data, as presented by Sato and Buchner [273]. However, accurate fitting of the fast response $(\Delta\varepsilon_2, \tau_2)$ requires better bandwidth coverage at higher frequencies. For instance, Sato and Buchner reported $\tau_2 = 0.39$ ps, $\Delta\varepsilon_2 = 2.14$, and $\varepsilon_\infty = 3.96$, using frequencies up to 0.089 THz, whereas the measurements of Rønne et al. [16] in the 0.1–2.0 THz range resulted in $\tau_2 = 0.17$ ps, $\Delta\varepsilon_2 = 1.9$, and $\varepsilon_\infty = 3.3$. This indicates, unsurprisingly, that the higher frequencies included in the fit to the THz-range data results in a better characterization of the fast process, effectively by moving spectral weight otherwise lumped into ε_∞ into the spectral region covered by the measurement. Yada et al. showed [164] that the intermolecular vibrational modes in the 5–10 THz range contributes to the dielectric function, and when this is accounted for in the curve fitting, the fast process is best characterized by $\tau_2 = 0.25$ ps and $\Delta\varepsilon_2 = 1.9$, and a lower value of $\varepsilon_\infty = 2.50$. Again, the higher spectral range available shifts spectral weight from ε_∞ into a specified process within the bandwidth of the measurement. This comparison shows that the highest possible bandwidth of the spectroscopic measurement is required for the complete characterization, and thus interpretation of the very broadband nature of dielectric relaxation in polar liquids. The frequency coverage should extend both to very low frequencies in order to detect the slow dynamics of the liquid, and extend to high frequencies in order to ensure overlap with the first vibrational modes of the liquid.

Both the slow and the fast relaxation processes depend strongly on temperature, and become significantly faster at elevated temperatures. The temperature dependence of the relaxational times holds important information about the physical mechanism responsible for the dielectric relaxational spectrum of water. Rønne et al. [16] showed that there is a linear dependence between the slow relaxational time constant τ_1 and the ratio of viscosity η and absolute temperature T, as predicted by the Einstein-Stoke-Debye relation $\tau_1 = 4\pi\eta R^3/k_B T$.

Rønne et al. [16, 274] also demonstrated that the temperature dependence of τ_1 for both protonated water (H_2O) and deuterated water (D_2O) follows a power law with a singularity (infinite relaxation time) deep in the supercooled regime (228 K for H_2O and 235 K for D_2O). This important observation indicated that the slow relaxation process in water is the structural relaxation process, related to the liquid as a whole. In contrast to this, the temperature dependence of the fast relaxation process measured by Rønne et al. [16] and Yada et al. [164] displayed no such power-law relation, and thus it is reasonable to assume that the fast relaxation is a process related to the individual water molecules.

The dielectric properties of water mixtures may differ significantly from those of pure water. In Fig. 25 we show an example of fitting a relaxational-vibrational model dielectric function to a combination of mm-wave and THz-range
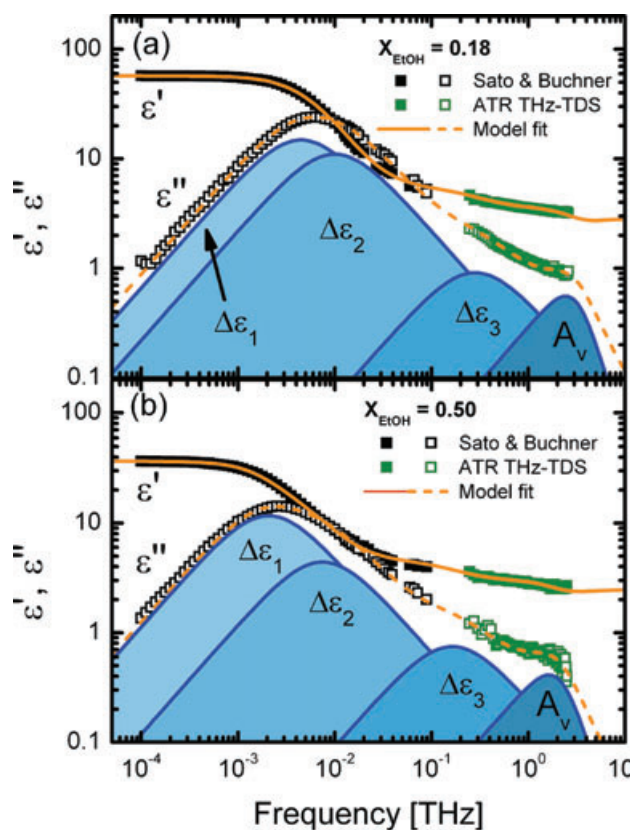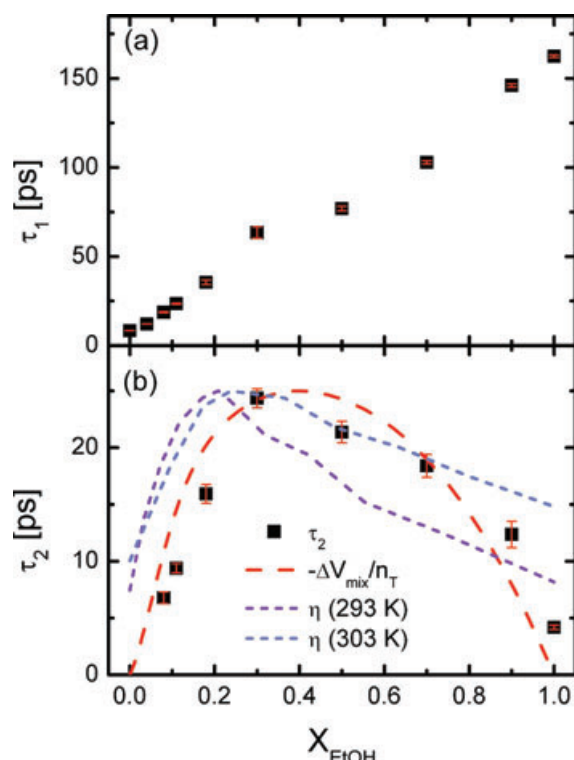

Figure 25 (online color at: www.lpr-journal.org) Combination of mm-wave data from Sato and Buchner (black symbols) and ATR THz-TDS data (green symbols) of the real and imaginary part of the dielectric function of water-ethanol mixtures with (a) $X_{EtOH} = 0.18$ and (b) $X_{EtOH} = 0.50$. The curves with blue shades of the fill color are the contributions to ε'' from the three relaxation processes and the vibrational modes, curves in orange show the model fit to the experimental data. Figure adapted from Møller et al. [149].

data of mixtures of water and ethanol [149]. The addition of larger molecules to water results in a more complex dielectric response, and it turns out that a third relaxation process must be considered in order to fit the experimental data with a relaxational model.

Figure 25 shows the combination of MHz-GHz dielectric data ($\hat{\varepsilon} = \varepsilon' + i\varepsilon''$) from Sato and Buchner [273] (black symbols) and THz data (green symbols) of water-ethanol mixtures with a molar fraction $X_{EtOH} = 0.18$ and $X_{EtOH} = 0.50$ in panels (a) and (b), respectively [149]. Together with the experimental data a simultaneous fit to the measured real and imaginary permittivity by a Debye-Lorentz model with three relaxational terms and a vibrational term is shown (orange curves). The contributions from each of these four terms to the dielectric loss (ε'') are shown as blue curves. Addition of ethanol reduces the concentration of hydrogen bonds in the solution, and thus the total relaxational strength of the mixtures is reduced, compared to pure water. In addition to the lowering of the overall dielectric strength, the relaxation processes are also slowed down by the addition of ethanol. Figure 26 shows the

Figure 26 (online color at: www.lpr-journal.org) (a) Relaxation time of the slowest process in water-ethanol mixtures at room temperature as a function of the molar fraction of ethanol, and (b) relaxation time of the intermediate process, shown together with the scaled differential mixing volume (red, dashed curve) and scaled viscosity at 293 K (violet, dashed curve) and 303 K (blue, dashed curve). Partly adapted from Møller et al. [149].

extracted slow and intermediate relaxation times of water-ethanol mixtures. Figure 26a shows that the time constant of the slow process increases in an approximately linear fashion with ethanol concentration. Figure 26b shows the time constant of the intermediate process initially increases with concentration, reaches a maximum near $X_{EtOH} \approx 0.3$, and then decreases on further increasing ethanol concentration. This behavior is correlated with the differential mixing volume (red, dashed curve) and the viscosity of the mixture (purple and blue curves for 293 and 303 K, respectively). This indicates that the intermediate process (and not the slow process) is related to the structural relaxation of the liquid mixture.

The shift in the relaxational dielectric strength to lower frequencies can also be used for characterization of the solvation shell of water molecules surrounding solutes in an aqueous solution. Water molecules within the solvation shell will interact with the solute in a manner that slows down their relaxational dynamics, and thus the contribution to the liquid dielectric response from the solvation shell will be found at lower frequencies than the response of the bulk water. The Tanaka group has applied Onsager local field theory to determine the size of the solvation shell surrounding a molecule in aqueous solution [17], and found specifically that 30 water molecules participate in the solvation shell

surrounding the two saccharides fructose and trehalose in dilute solution. They also showed that the solvation shell reduces in a linear fashion with increasing concentration of the saccharides. Interestingly, their results indicated that the effective volume taken up by a water molecule in the solvation shell is approximately 90% of that of a water molecule in the bulk, due to the slower relaxation dynamics.

By a similar approach, the same authors determined the hydration number of 2-butoxyethanol (2BE) in the form of monomers and micelles, as a function of temperature [165]. The temperature dependence of the hydration numbers showed that the micelle structure stabilises the solvation shell compared to 2BE monomers, indicating that the micelle surface facilitates strongly bound and self-organized water molecules.

5.3. TRTS of semiconductor nanostructures

Characteristic length scales such as the mean free path govern the transport properties of band semiconductors, which are typically 10s to 100s of nm in bulk systems at room temperature. As semiconductors are decreased in size to the point of being comparable to the mean free path, it is not surprising that the materials cease to behave like bulk matter. In the case of nanostructures, size effects contribute to an increased Drude scattering rate as barriers and interface fluctuations become significant sources of scattering. However, one of the fundamental assumptions in the Drude model, that momentum is isotropically randomized upon scattering, comes into question if the scattering occurs in a half-space with no accessible states on the opposite side. In this case, backscattering should be preferential and the Drude model should give way to models of carrier localization.

TRTS has made significant contributions to understanding carrier dynamics in semiconductor nanocrystals and quantum dots in recent years, and we will briefly review the progress here. Electrical connection to nanostructures is often difficult or even impossible without influencing the system under study, and so an all-optical conductivity probe is desirable. The length scales probed by an ac electromagnetic field of frequency ω can be estimated by $L_\omega = \sqrt{D/\omega}$, where D is the diffusion coefficient. For a typical $D = 10 \, cm^2/Vs$ and $\omega = 2\pi \times 10^{12} \, s^{-1}$, $L_\omega = 13 \, nm$. The ac response at THz frequencies is therefore a sensitive probe of nanoscale charge motion in semiconductors.

Heterostructured quantum dots formed by Stranski-Krastanow growth are coupled to one another through a continuum of higher-energy wetting layer and barrier states, and also potentially directly by tunneling if allowed. The resonances associated with intersubband transitions in these structures are typically at higher energies (100 meV) than the THz pulse bandwidth in a standard TRTS setup, and so the THz response is dominated by band conduction of carriers in wetting layers or barriers. The large change in conductivity of a charge carrier before and after it has become captured into a localized QD state makes TRTS ideally suited for determining carrier capture dynamics in the case

of nonresonant excitation [176, 275–279] and escape dynamics in the case of resonant excitation of localized QD states [279]. The same principle has also been applied to one-dimensional structures, including heterostructure quantum wires [181] and quantum posts [280] and free-standing GaAs wires [179, 281]. Recently, ultrabroadband TRTS has been applied to n-doped InAs/GaAs quantum dots with bandwidth spanning both the low-frequency Drude component of the uncaptured charges and also resonant intersublevel s→p transitions of both neutral and charged excitonic transitions in the QDs [282]. Thus, both free and bound charge dynamics, and their interplay, could be determined simultaneously.

Colloidal quantum dots and nanocrystals have been studied in the noninteracting limit, dispersed in solution to a concentration where particle interactions are negligible [174, 283, 284]. In this case, the low energy of the THz pulse is insufficient to resonantly excite electrons, since the quantized electron transitions are typically spaced by several hundreds of meV. The THz pulse energies can either be resonant with hole transitions, which are on the order of 10s of meV, or completely nonresonant depending on the level of confinement. Beard et al. investigated size-dependent intraparticle photoconductivity in CdSe quantum dots and found an r^4 behavior of the carrier mobility for nearly monodisperse CdSe QDs in the strong confinement regime with radius below the Bohr radius of 4.9 nm [174]. Effective medium theory was used to relate the observed THz spectra to the microscopic particle conductivity that was described by a Drude model. Wang et al. also later showed a purely instantaneous response of CdSe QDs of radius smaller than the Bohr radius, where the electric susceptibility was observed to be entirely real (i. e. purely imaginary conductivity) [283]. The polarizability of these strongly confined excitons also obeys an approximate r^4 law, completely consistent with Beard's findings although in a more appropriate language of excitonic transitions for particle sizes smaller than the Bohr radius. The total ground-state polarizability was treated as a summation of electron and hole contributions, with the hole contribution shown to dominate due to the larger effective mass and smaller transition energies. The sensitivity of the nonresonant THz response of CdSe quantum dots in the strong confinement regime to the polarizability of the lowest-energy hole state was subsequently used by Hendry et al., who combined TRTS with femtosecond luminescence measurements to determine interband recombination and hole cooling rates in photoexcited CdSe quantum dots [284]. By examining the dot-size dependence at a fixed excitation energy, the threshold for excitation into the first excited state was identified that coincided with a slow down of the dot luminescence rise time, determined by femtosecond luminescence upconversion. This indicated a slow down of the electron and/or hole relaxation dynamics. 1D TRTS measurements of the hole relaxation dynamics also showed a slow down coinciding at the same diameter quantum dots corresponding to the luminescent slow down. Thus, it was concluded that energy transfer from hot electrons to holes is responsible for the slow down of hole relaxation as they are re-excited by collisions with energetic electrons. This

was strong evidence for Auger relaxation processes being responsible for the bypassing of the so-called phonon bottleneck predicted in zero-dimensional systems.

Quantum dot and nanocrystal ensembles have been intensively studied with TRTS in recent years [5, 175, 177, 178, 183, 285], with a focus on the understanding of the conductivity spectrum and carrier dynamics when interparticle transport is possible. Photoinduced THz absorption in arrays of colloidal InP quantum dots, whereby the interdot distance was varied via surface ligands of different length [285], was found to depend strongly on interdot spacing, indicating that interparticle transport can be dominant over intraparticle polarizability provided there is significant wavefunction overlap. Here, electrons were assumed to be the dominant charge carrier, as the tunneling barrier is lowest for the smaller effective mass carrier. Cooke et al. have examined ensembles of silicon nanocrystals (Si-NCs) with controlled size and density, by thermal decomposition of SiO to form Si nanocrystals embedded in an insulating SiO_2 matrix, and compared their response to connected poly-nanocrystalline silicon films and bulk-like epitaxial silicon-on-sapphire [5, 178]. The Si-NC films were below the classical percolation threshold based on the volume of spherical conducting particles, and so the observed THz conductivity was attributed to intraparticle charge motion. The authors described the response by a classical Drude-Smith model that incorporates carrier backscattering into current response function through use of Poisson statistics. The frequency-dependent complex conductivity is described by

$$\tilde{\sigma}(\omega) = \frac{N e^2 \tau / m_{\text{eff}}}{(1 - i\,\omega\tau)} \left[1 + \sum_{n=1}^{\infty} \frac{c_n}{(1 - i\,\omega\tau)^n} \right], \quad (49)$$

where N is the carrier density, τ is the carrier scattering time, and c_n is defined as the carrier backscattering parameter for the nth collision [286]. Typically, it is only the first $n = 1$ term that is taken into account as an approximation and we drop the index. The model has the advantage of being fully Kramers-Kronig compatible and blending continuously from a simple Drude form ($c = 0$) to fully localized response ($c = -1$), equivalent to that of an overdamped oscillator.

This model has been applied by several THz groups in recent years, as it has been found to describe the THz conductivity spectrum of a wide variety of nanostructured and disordered conductors. Monte Carlo studies have recently shown that the conductivity response obtained by assuming reflection from the nanocrystal barriers reproduces the Drude-Smith form quite well with the probability of reflection corresponding approximately to the Drude-Smith backscattering parameter [287]. Figure 27 shows the THz conductivity spectrum for 400-nm photoexcited films of (a) epitaxial silicon on sapphire, (b) polynanocrystalline Si on glass with grain sizes of approximately 20 nm and (c) silicon nanocrystals embedded in insulating SiO_2 with average density, diameter and spacing of $1.7 \times 10^{18} cm^{-3}$, 7 nm, and 1.4 nm. The Drude-Smith model is capable of describing the entire range of THz conductivity as the sample morphology progresses through bulk to nanoscale, with the c
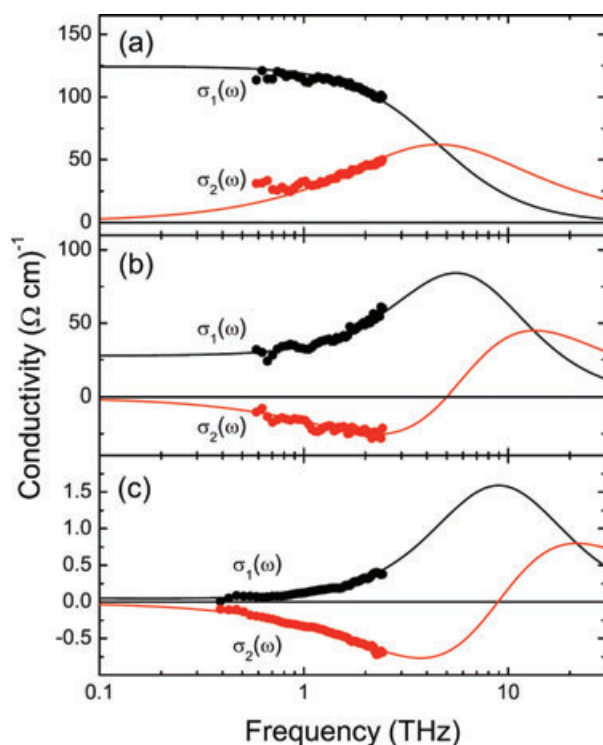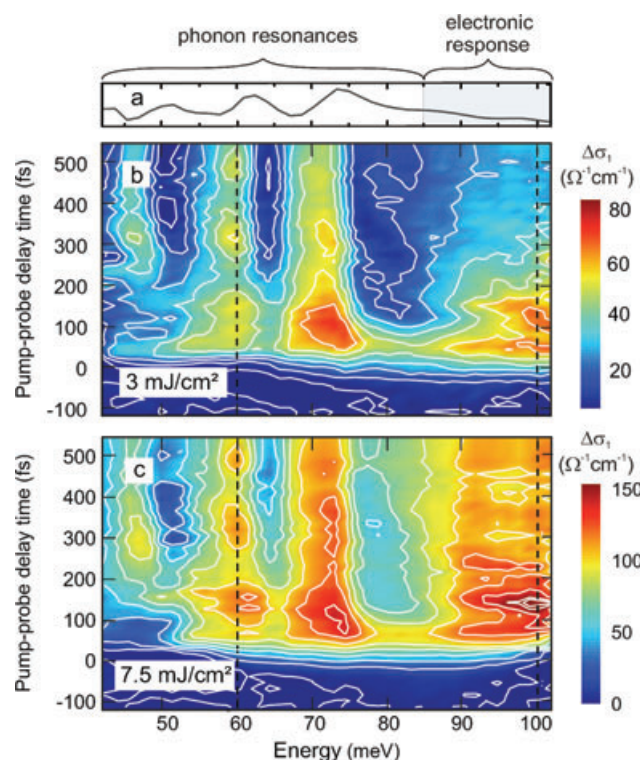
Figure 27 (online color at: www.lpr-journal.org) Complex conductivity spectra for 400 nm photoexcited films of (a) epitaxial silicon on sapphire, (b) polynanocrystalline silicon on fused silica, and (c) Si-nanocrystals embedded in glass. Curves are fits to the Drude-Smith model described in the text.

Figure 28 (online color at: www.lpr-journal.org) (a) THz conductivity spectra of the phononic and electronic regions. Two dimensional TRTS map of the real conductivity for the near-IR photoexcited VO_2 film (b) below and (c) above the critical excitation fluence Φ_c. Figure adapted from [200].

parameter varying from Drude form with $c = -0.007$ (bulk) to $c = -0.830$ (connected nanocrystals) and $c = -0.983$ for the nanocrystals separated by insulating barriers. In the Monte Carlo formulism presented by Nemec et al. [287] (Eq. (6)), this corresponds to a reflection probability of 85% and 95% for the polynanocrystalline silicon and Si-NCs, respectively, assuming a bulk mean free path of 40 nm for silicon. This also implies a dc conductivity in the Si-NC film, which was verified with traditional photoconductivity measurements [5].

5.4. TRTS of strongly correlated systems

A particularly interesting aspect of physics where TRTS has made a significant contribution is to our understanding of nonequilibrium and ultrafast phenomena in the area of strongly correlated electronic systems [199]. Vanadium dioxide (VO_2) is a prototypical example that undergoes an insulator-to-metal transition at a temperature of 340 K, accompanied by a structural transition from a monoclinic to a rutile phase. The subtle interplay between lattice and electronic degrees of freedom in VO_2 and the ability of TRTS to independently probe both components make it a subject of interest for the THz community [200, 288, 289].

One such study from the Konstantz group employed TRTS to examine the interplay between the charge and lattice degrees of freedom and their participation in the metal-to-insulator transition on ultrafast time scales after photoexcitation [200]. Figure 28 shows the photoinduced change of the multi-THz real part of the conductivity of vanadium dioxide (VO_2). Such a map demonstrates the rich, detailed and unique information that can be obtained using 2D TRTS, particularly when ultrabroadband THz pulses are employed spanning the spectral signatures of multiple elementary excitations. In this work, the authors studied the evolution of the THz conductivity of VO_2 following photodoping with a 12-fs optical excitation at temperatures in the vicinity of the metal-insulator transition. Figure 28b and c are the 2D differential real conductivity maps taken at a lattice temperature of 250 K and below and above the critical pump fluence $\Phi_c = 5.3 \, mJ/cm^2$ where the onset of a long-lived metallic component is observed, indicating the crossover to the metallic state. Such a map is derived from a $-\Delta E$ map similar to Fig. 15a.). The authors identify two spectral regions shown in the horizontal cut in Fig. 28, as the region for phonon signatures for energies below 85 meV (denoted as P) and above where there are no phonon resonances and only the broad Drude component of photoelectrons are present. Photoexcitation alters the polarizability of the phonon modes, producing a visible change in $\Delta\sigma_1$. Below Φ_c a persistent coherent modulation of all phonon modes along the pump-probe time axis is observed while the electronic component decays within 400 fs. Above Φ_c, the modulation is also observed in region P, but there also

exists an in-phase replica of the modulation observed in the electronic region E for pump probe delay times $\tau < 130$ fs. This modulation undergoes one in-phase oscillation with the lattice, after which no modulation is present and the conductivity settles to a near-constant value. A Fourier transform of this modulation corresponds to a mode at 6 THz, close to the ground state stretching and tilting modes of V-V dimers at 5.85 and 6.75 THz that map the monoclinic lattice to the rutile phase.

The authors propose that the origin of the modulation is that the photoexcitation of the ground state monoclinic phase removes an electron from the bonding orbital that then destabilizes the V-V dimer. The excited state of the lattice, which would normally be dissociative, has an energy minimum due to strong nearest-neighbor repulsion near the nuclear position of the rutile phase, approximately 0.2 Å greater than the monoclinic phase. The excited dimers then oscillate in this minimum potential at the 6-THz frequency. That the excited-state electronic replica of this modulation dies out after a single oscillation is an indication of the strongly correlated nature of this material, which implies a deviation from the Born-Oppenheimer approximation that the electron responds instantaneously with the lattice to one where the reaction becomes slower than a V-V vibrational period.

6. Practical applications for THz systems

Presently, a large variety of practical applications are discussed for THz systems. They range from body scanners through the monitoring of industrial production processes to THz communications. Here we restrict ourselves to optoelectronic THz spectroscopy systems and discuss only application scenarios associated with this class of systems. Many of those applications involve THz imaging. While the first image with a THz-TDS system was obtained in 1995 by Hu and Nuss [290] the first CW image obtained with a photomixer based system was reported in 2001 by Kleine-Ostmann et al. [57]. Since the work by Hu and Nuss many different variations of THz imaging have been explored, including near-field imaging [291–295], THz tomography [296–299], polarization imaging [300–303] dark-field imaging [304], single-pixel imaging [305], time reversal imaging [306], reciprocal imaging [307] and interferometric imaging [308]. A comprehensive review on these techniques was recently published by Chan et al. [309].

Simultaneously, many applications ranging from packaging inspection [310] over medical diagnosis [311–313], wafer inspection [314, 315] and plant physiology [310, 316] to dendrochronology [317] have been discussed. Yet, after some initial investigations and considering economic arguments some of these application fields turned out not to be too promising. One example is clinical diagnosis. Since THz waves cannot penetrate more than a few hundred micrometers of human tissue, their use is restricted to an investigation of the body surface. In a study it was shown that pulsed THz imaging can distinguish between basal cell carcinoma and other skin irregularities [312]. Unfortunately, and despite

the results of this study, the interest shown by dermatologists has remained low due to the high price of pulsed THz systems. The reality is that dermatology clinics and practices are not prepared to invest a large amount in a technology that only brings limited additional dermatological information. Yet, system cost is only one critical parameter, the other being the speed at which images can be obtained.

If it comes to objects to be imaged, two different classes of items should be distinguished. On the one hand there are objects that differ from sample to sample regarding shape or detailed composition. This class comprises a passenger's suitcase, cultural heritage and basically all biological specimens, such as skin cancer, wood or plant leaves. To obtain useful information on these kinds of samples one typically needs to collect and analyze a tremendous amount of THz data. Mostly, it is necessary to acquire a full THz waveform per pixel. Hence, it typically takes several minutes or longer for a scan of the entire item. Such long scanning times are acceptable for scientific applications when only a limited number of samples need to be investigated. They may also be tolerable if more information is required on individual pieces of luggage out of the luggage stream at an airport.

Yet, such long scan times are insufficient for the control of industrial production processes that produce one or several items every few seconds. Fortunately, most industrial products fall into the second class of objects, i.e. samples that are nominally identical from item to item. Much less data are required to evaluate if an individual item fulfills given fabrication tolerances. In many such cases the full waveform per pixel is not required. It may even be sufficient to scan the item at a fixed time delay, e.g. a delay that corresponds to a position within the rise of the falling edge of the main THz pulse. Thickness variations in a plastic part that lead to a temporal shift of the main pulse will then be easily identified [58]. This measurement scheme is at least two or three orders of magnitude faster than the scheme in which a full THz waveform is required per pixel. Hence, it may be fast enough for industrial purposes. To further increase the speed of the imaging process one can realize one-dimensional arrays of THz detectors and THz emitters. The item to be inspected is then scanned only in one dimension. An early attempt in this direction has been reported by Hermann and coworkers who used an array of eight photoconductive antennas [318]. In 2008 Pradarutti et al. demonstrated a line array of 16 elements coupled to a microlens array that generates 16 single spots from the exciting fs-laser beam [319]. Very recently, Picometrix demonstrated a hand-held, high-speed THz-TDS reflection line-scanner [320]. It scans a line that is 150 mm wide. By rolling the scanner over a surface, a two-dimensional image can be stitched together from the individual lines at a rate of 25–200 mm/s.

An alternative approach to one-dimensional [321, 322] and two-dimensional images [299, 323] uses electro-optic crystals and multichannel-balanced detection. It is very likely that the combination of these approaches and further advances will enable real-time imaging of industrial goods in real industrial environments.
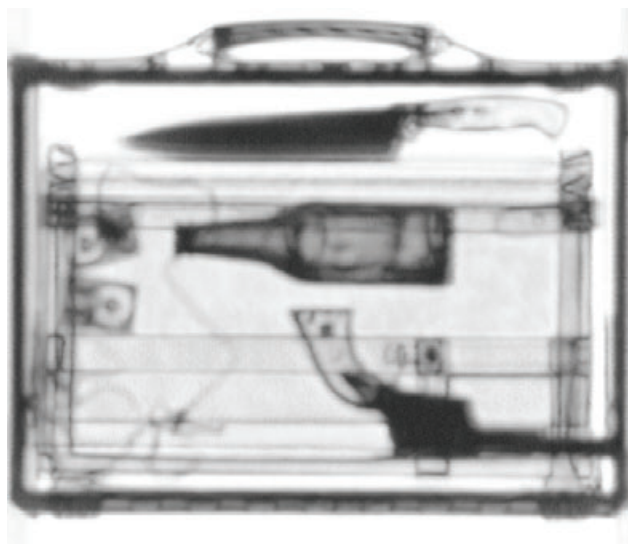
Figure 29 THz transmission image through an attaché case. A gun, a knife and a bottle are clearly identified (courtesy of Picometrix).

Figure 30 (online color at: www.lpr-journal.org) Cartoon that illustrates the use of a handheld THz scanner for the analysis of bottles carried by passengers.

6.1. Security applications

Considerable market potential for THz systems is foreseen in the field of security. The so-called body scanners that have been recently introduced in airports are mostly not THz scanners in a strict sense as most of them use radiation at a few tens of GHz. Yet, THz cameras that could detect concealed and suspicious objects on a fully clothed individual at a distance of 25 meters could work in the sub-THz frequency range. The distance of 25 meters provides a sufficiently large safety margin against potential terrorists carrying explosives. At present, several companies are intensively developing this type of security camera. Most of the THz receiver arrays under development are based on highly developed microwave technology at one or a few hundred GHz. As these devices do not fall into the class of optoelectronic THz systems we abstain from discussing them further in this paper.

Optoelectronic THz systems could be used for close-by-inspection of luggage or mail. As we have seen earlier in this paper molecular crystals show THz spectra that are rich in absorption peaks specific to the particular substance. Consequently, explosives or illicit drugs could be localized and unambiguously identified within an envelope [324], a parcel, a bag or a suitcase, whereby the level of difficulty rises in this order. Furthermore, dangerous metallic items like a gun or a knife become clearly visible by their silhouette [325].

Several demonstrations of mail and luggage inspection using THz waves have been reported so far [326, 327]. The most impressive of them was performed by Picometrix [326]. One of their THz images obtained on an attaché case in transmission geometry is shown in Fig. 29. Clearly a gun, a knife and a bottle are visible inside the case. The image was obtained with a speed of 66 pixels per second leading to a total scanning time of several 10s of minutes. Furthermore, Picometrix demonstrated that the attaché case can be analyzed layer by layer using reflection geometry, i. e. by THz tomography [326].

A scanning time of many minutes may be tolerable if THz imaging is used as a supplement to X-ray scanners to obtain more information on individual pieces of luggage that appear suspicious in an X-ray scan. Yet, it should be noted that an aluminum suitcase or other metallic packages are not transparent at all to THz waves. Hence, THz spectrometers are unlikely to replace X-ray scanners. Nevertheless, they can be used in addition to established techniques to obtain further information on mail or luggage.

In this context and for the sake of completeness it should be mentioned that Sasaki and coworkers developed a THz system that can detect concealed powders in postal mail [328]. The system, which is placed under a belt conveyer system and is ready to be used at airports, detects THz waves specifically scattered off powder targets. Suspicious envelopes are then removed from the mail system for further inspection.

The fortunately disrupted terrorist plot of bombing an aircraft with liquid explosives in London, August of 2006, again exposed breaches in the existing security systems for passengers and luggage control. Even very small amounts of a liquid explosive would be sufficient to inflict fatal damage on a plane. This group of materials is very hard to detect with existing devices installed in airports. In order to close this significant security breach, the THz groups in Marburg and at DTU are currently working independently towards a hand-held optoelectronic THz system for the detection of liquid explosives.

The goal is to develop a hand-held THz reflection spectrometer (Fig. 30), which consists of two components: a small fiber-coupled transceiver head with the size of a common flashlight as well as a compact control module, which incorporates a miniature femtosecond fiber laser as the optical pump source [80]. This head is held against the bottle or vessel to be inspected. A high degree of system integration will make it possible to carry the device similar to a photo bag. While bulk explosives like RDX have already

been spectroscopically analyzed in the terahertz frequency range [329, 330], the increasingly critical group of liquid explosives still needs to be characterized. As we have seen earlier in this article different liquids show different THz properties. Spectra of nitromethane, nitroethane, and hydrogen peroxide are shown in [149]. The general appearance of these spectra is rather similar (and in the case of hydrogen peroxide, identical) to the spectrum of water, indicating that in the general case, there is no guarantee that potentially dangerous liquids can be distinguished from harmless liquids by THz spectroscopic methods. However, it seems possible to distinguish between volatile liquids with low refraction and aqueous liquids with higher refraction due to the large index contrast typically found between these two classes of liquids, even when the liquid is placed inside a container with dielectric properties less well defined than a plane window with thoroughly characterized optical properties [146], confirmed also by unpublished results from the Koch group in Marburg.

All in all, it is expected that there is a considerable market potential for THz systems to supplement other established technologies like metal detectors or X-ray scanners.

6.2. Food industry

The detection of foreign bodies in eatables plays an important role in the food industry. Currently, metal detectors and X-ray systems are used for this purpose. Yet, while the former can only detect metallic contaminations the use of X-ray scanners is limited and not openly communicated as the industry fears that consumers may not feel comfortable with the idea of testing eatables with ionizing radiation. Consequently, THz systems may offer an alternative for the non-ionizing nature of THz waves. Unfortunately, most eatables contain considerable amounts of water and, hence, cannot be penetrated by THz radiation. Nevertheless, THz systems may have some applications for quality control. For instance, it was early shown that chocolate is very transparent to THz waves as it contains only little water and consists mostly of fat [311]. Therefore, THz systems could be used to detect of foreign bodies in chocolate products. Recently, Jördens and Koch [331] investigated different metallic and nonmetallic contaminations within chocolate bars with THz-TDS. They showed that it is possible to distinguish between foreign bodies and ingredients that belong in the product, such as nuts, by analyzing the shape of the temporal waveform. While a single pulse indicates pure chocolate or nuts, a double-pulse structure indicates a nonmetallic contamination like a stone, a piece of glass, or a plastic particle. The double-pulse structure arises from differences in the refractive index between chocolate and contaminations. However, since localized variations in the thickness of the chocolate bar may also lead to a double-pulse structure, the height profile of the chocolate must be measured and taken into account as well in the image-processing step. In the thickness-corrected delay image (the spatial variation of the arrival time of the THz signal across the image) it is then possible to detect a glass splinter within a chocolate bar containing hazelnuts [331].

Dry powders are also quite transparent to THz waves. Herrmann et al. [332] demonstrated the detection of foreign bodies in different powdered eatables. The list of powders included sugar and wheat flour; the list of detected items comprised an eggshell and different plastic pieces. Yet, the powdered samples were only 1 cm thick. It remains to be seen whether THz waves can penetrate thicker powder layers and, hence, can be practical for real-life cases.

6.3. Plastics industry

In the polymer industry several applications are discussed for THz systems. They include the inline monitoring of polymeric compounding processes [333,334], the quality control of plastic weld joints [335, 336], the determination of the moisture content [337], the fiber orientation [303, 338] and the glass-transition temperature of polymers [339]. In the following, we briefly illuminate two of these different applications.

## 6.4. Inline monitoring of polymeric compounding processes

Polymeric compounds are mixtures between polymeric base materials such as polyethylene, polypropylene, polyamide, and a few others and additives. Additives can be quite diverse in size, shape and material. Examples include pigments, glass fibers, carbon nanotubes and flame retardants. These particles are added to the base polymers in a process that is called polymeric compounding. The base polymer is heated above its melting temperature. To this hot polymer melt the additives are fed in defined quantities using a dosing unit. Subsequently, the mixture is homogenized in an extruder. The physical properties of the compounds are tailored and differ from that of the base polymers. In a later process plastic devices are fabricated out of this polymeric compound, mostly by injection molding. Yet, plastic devices, the physical properties of which vary from one end to the other, are undesired. Hence, it is important that the additive distribution is perfectly homogeneous. The homogeneity of the polymeric melt flow can be monitored with THz spectroscopy [334].

In many cases the refractive index of the polymeric compound varies linearly with the additive content [333]. Figure 31 shows four such examples. The shown material systems are polypropylene and chalk, polyethylene and $Mg(OH)_2$ (a flame retardant), polyamide and glass fibers and a wood-plastic composite (WPC). The data are obtained offline on a set of injection-molded samples. The dependencies between the additive content and the refractive index can be fit by a linear dependence. In all cases the correlation coefficient is close to unity.

However, some cases show more complex dependencies [340]. In any case, the additive concentration can be deduced from the measured refractive index.

To demonstrate inline monitoring of polymeric compounding processes Krumbholz et al. developed a rugged
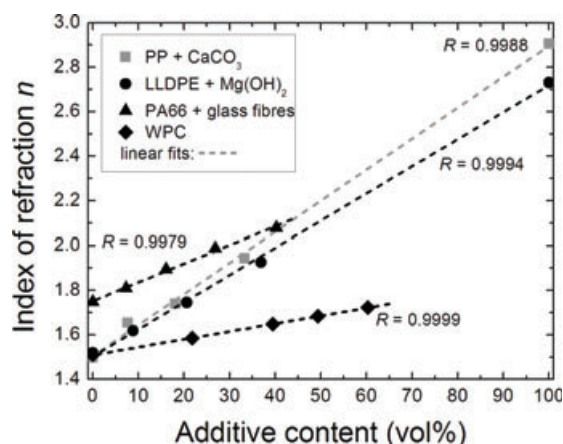
Figure 31 (a) Refractive index as a function of the volumetric additive content for different polymeric compounds. For the examples shown here one finds a linear dependence. Figure adapted from [333].
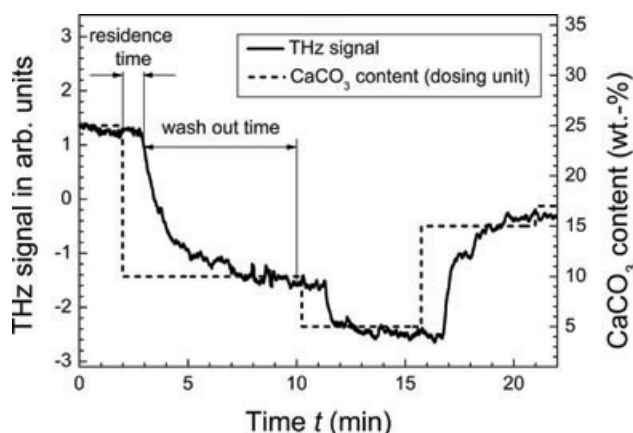
Figure 32 Nominal additive content (dashed curve) and THz signal obtained during an inline test on a polypropylene-chalk mixture. Figure adapted from [334].

and sealed fiber-coupled THz spectrometer. It operates in a rough industrial environment that contains dust, vibrations and heat. Details on this spectrometer can be found in [334]. Fortunately, this application does not require the acquisition of real-time images but involves a single-point measurement. Consequently, here the measurement speed is not a limiting issue.

Figure 32 shows THz data obtained during an inline test on a polypropylene-chalk ($CaCO_3$) mixture. The dashed curve with rectangular turns shows the nominal additive content of the compound. The black line displays the time evolution of the THz signal. In this case an entire waveform is not acquired but the THz signal for a fixed time delay between the incoming THz pulse and the optical pulse gating the detector antenna. The temporal position is located here on the falling edge of the THz pulse. A higher additive concentration causes the THz pulse to arrive somewhat later. Due to the temporal shift of the THz pulse the signal increases. Likewise, the signal drops if the additive concentration is reduced.

It can be seen that the THz signal follows the concentration with a delay of somewhat more than a minute. The reason for this is that the position at which the THz measurement is performed is downstream from the dosing unit. The polymer melt needs some time to be transported to the measurement spot. As the additive content is reduced the signal does not drop abruptly but rather shows an exponential decrease. This reflects the fact that the higher additive content is gradually washed out. In any case, this demonstration shows that THz spectroscopy is ready to monitor polymeric compounding processes.

6.5. Determination of the glass transition

But offline THz tests may also become useful in the polymer industry. Wietzke et al. recently showed that THz spectroscopy is ideally suited to determine the glass transition of polymers with high accuracy [339]. The glass transition, i. e. the transition between the glassy and the rubbery state in the amorphous phase of polymeric materials does not take place at a definite temperature as would be required by equilibrium thermodynamics, but rather in a temperature range. Therefore, the glass transition is a kinetic transition [341]. However, it is still subject to intense research and not fully understood.

Figure 33 shows a data set for polyoxymethylene (POM). Plotted is the temperature-dependent THz refractive index of the material. When extrapolating the slope of the refractive index change with temperature, T_g is determined by the crossover between the two linear regimes. The glass transition range determined by standard differential scanning calorimetry (DSC) is indicated by the grey coloured bar. Due to the highly crystalline sample (56–60%) it is only weakly pronounced in the DSC measurements. However, the inflection point of the calorimetric step coincides with
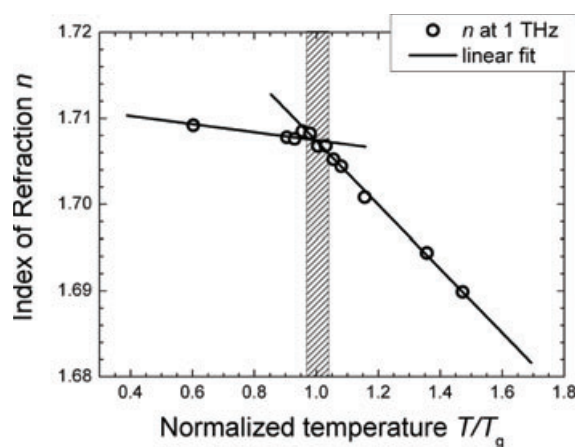
Figure 33 The temperature dependence of the THz refractive index reveals a glass transition of POM at $T_g = 199$ K as the intersection of two linear fits extrapolating the low- and the high-temperature regime. For comparison, the glass-transition temperature interval, obtained from DSC measurements, is indicated as the grey area. Figure adapted from [339].

the THz results for T_g. Moreover, THz-TDS clearly shows the glass transition also for other partly crystalline polymers (e. g. HDPE, LDPE, PVDF).

6.6. Paper industry

The paper business is another industrial branch that can profit from an inline control with THz-TDS systems. The task is to monitor the thickness and moisture content of the paper during the production process. Banerjee et al. recently demonstrated a quantitative method for determining the moisture content in paper based on extinction and phase measurements in the lower THz range with a spatial resolution in the mm range and scanning times below two minutes [342]. Mousavi and coworkers used a Bruggemann effective medium theory to look for a simultaneous determination of thickness and moisture content of paper sheets [343]. They demonstrated their technique on two different paper samples and obtained uncertainties that are comparable with existing sensor technology.

Although further studies are needed, these first experiments show that THz-TDS is promising for inline control of paper production processes. Yet, it may be that future commercial systems that satisfy the discussed needs of the polymer and paper industry for inline monitoring will, for cost issues, rely on THz quasi time-domain spectroscopy [344].

6.7. Pharmaceutical industry

The pharmaceutical industry has very high quality standards that are ensured by laboratory analysis. If the final product fails to meet the specification the entire batch is rejected. Hence, inline tests throughout the entire manufacturing process are highly desirable. The potential of THz systems in the pharmaceutical industry was recently explored by Teraview [345]. As discussed in Sect. 5.1 different isomers lead to different crystalline structures with different spectral fingerprints in the THz range. Hence, an organic compound, e. g. an agent can come in different polymorphic forms that typically differ in their physicochemical properties and ultimately in their pharmaceutical performance. Based on their spectral characteristics Taday and coworkers could distinguish between two polymorphic forms of ranitidine hydrochloride both in the pure form and in formulated tablets [346]. Furthermore, they showed that the concentration of substances in pharmaceutical mixtures can be reliably obtained [345] and that drug hydrate systems and dehydration processes can be studied by THz-TDS [347].

Another application in the pharmaceutical industry is in quality control of tablet coatings that are used to control the release of active pharmaceutical ingredients. In a recent study, Fitzgerald et al. [348] showed that it is possible to distinguish between two brands of over-the-counter ibuprofen tablets by their coating. A further study by Spencer et al. concerned the delayed release of the agent [349]. They first determined the coating thickness of a set of Ascol® tablets. Subsequently the tablets were dissolved and the

mean dissolution times were determined. They correlated with the average coating thicknesses. Altogether, the above-mentioned and further studies by Teraview indicate market potential for the quality control of pharmaceutical products.

6.8. Art conservation

Paintings and murals are valuable genuine pieces of evidence of the cultural heritage of mankind. They often consist of several layers of paint subsequently applied in the course of time. Every one of them is to be considered an artwork in itself that should be conserved. Up to now, nondestructive detection of images hidden below the top layers has been successful only in a few exceptional cases. For such purposes infrared or X-ray techniques have been used. Yet, the success of these techniques is inherently restricted by limits to resolution and penetration depth. Lately, initial steps have been taken to explore the potential of THz spectroscopy for art conservation.

The first THz investigation of a painting was performed by Köhler et al. who studied a painting on canvas in transmission [350]. The painting consisted of canvas, whiting, paint layers, and varnish, typical for 19th-century paintings. Figure 34b shows a THz image of the painting obtained by
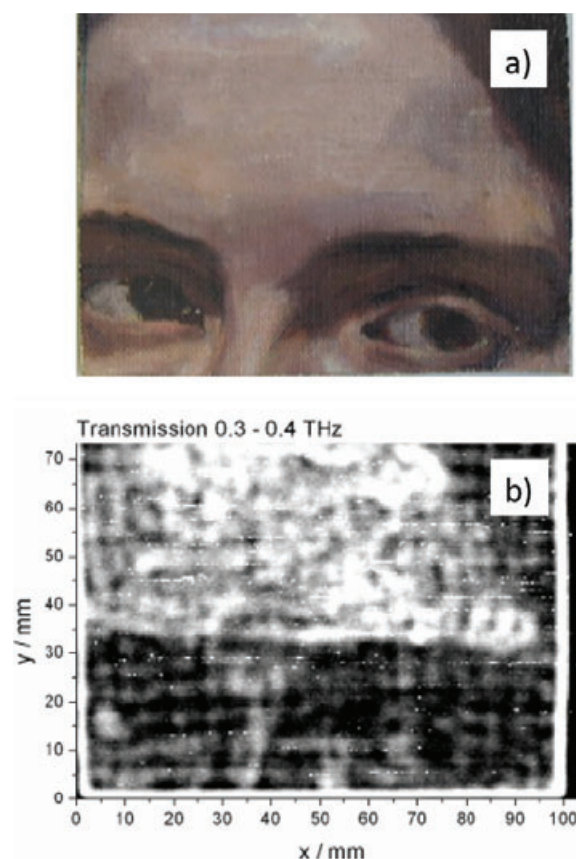
Figure 34 (online color at: www.lpr-journal.org) (a) Visual and (b) terahertz transmission image of a painting on canvas. Figure adapted from [350].

integrating the transmitted intensity in the frequency window from 0.3 to 0.4 THz. The corresponding visual image of the painting is shown in Fig. 34a. The contrast observed here arises from the different absorption strength of the paints employed. For the chosen frequency window THz waves have a wavelength that is somewhat smaller than one mm. This is already on the order of the structural dimensions of the canvas. Hence, the fabric of the canvas induces a texture in the THz image that is not visible for lower THz frequencies [350]. This preliminary study showed, however, that different paints can in principle be distinguished. A more comprehensive study was presented in 2007 by Fukunaga and coworkers [351]. Using a THz-FTIR spectrometer they generated a database on the THz properties of different pigments, binders and theirs mixtures. On the basis of this database they performed an impressive transmission analysis of a painting and a stained glass-like sample. Recently, they extended their investigations on a medieval manuscript using THz-FTIR and THz-TDS [352].

Moreover, Jackson et al. performed a first THz investigation of mural paintings [353]. They studied a graphite drawing through both paint and plaster overlayers using THz-TDS. Naturally, these measurements were performed in reflection geometry. In both cases the drawing was clearly recognizable. Yet, the studied case represents a very favorable situation as graphite is highly reflecting. It remains to be seen how practical THz spectroscopy turns out to be for real world cases that may offer a much lower contrast. Nevertheless, the work by Fukanaka et al. clearly demonstrated the potential of THz imaging for paintings studied in transmission.

In a further study Adam and coworkers compared THz reflection images of hidden paint layers in a painting on canvas [354]. The results were compared with the results obtained with X-ray radiography and infrared reflectography. The study showed that only THz imaging provides information on the thickness of the hidden paint layers. This finding underlines the potential of THz imaging for art historians, conservators and conservation scientists.

7. The future of THz spectroscopy

Since the pioneering work by Grischkowsky in the late 1980s terahertz spectroscopy has become an established tool for a still increasing number of research labs worldwide. Using this technique a tremendous amount of scientific information has been gained in the previously difficult to access terahertz spectral region. The coherent detection of these phase-locked pulses and the rejection of incoherent background radiation has enabled new science, including time-resolved studies of nonequilibrium phenomena. In addition, numerous variations from the simple one-emitter, one-detector transmission scheme have been devised. Both these variations as well as a large portion of the scientific results obtained on the different states of matter were reviewed in this article.

Although one should be cautious with forecasts there are things that one can safely say that seem likely directions for the future of THz science and technology. One can safely assume that a lot of exciting basic research experiments will be carried out in the future on all states of matter using THz spectroscopy, as source and detection technology are pushed to the limits of bandwidth, sensitivity and intensity. In particular, the interaction with intense THz field exceed tens of kV/cm will prove to be interesting, as table-top laser sources can now be used to reach THz field strengths that previously were only accessible by large user facilities such as free-electron lasers or synchrotrons [129, 355–357]. Such strong fields will, for instance, allow for the investigation of static and time-resolved ultrastrong light-matter interactions [358]. This enables nonlinear effects to be observed in the THz regime, and potentially used to develop new routes of commercial exploitation of the THz spectrum. These nonlinear interactions require us to go beyond our classical understanding of light-matter coupling, for example the observation of anharmonicities in the potentials of all kinds of bonds between atoms or molecules. Katayama and coworkers, for example, very recently observed the anharmonicity in the soft-mode potential of quantum-paraelectric $SrTiO_3$ thin films [359].

Together with the development of intense THz sources, there will be a need for further refinement of numerical tools for simulation of the interaction between THz radiation and solid-state matter. The development of precise *ab-initio* code for simulation of the THz-frequency dynamics of molecular crystals at finite temperatures, during interaction with an ultrabroadband THz pulse, is one example of a development that, if implemented, will advance our understanding of energy coupling in such systems, and help to pave the way towards nonlinear spectroscopy, and in particular 2D THz spectroscopy.

There is also a definite push towards the development of ultrabroadband terahertz spectroscopy, with the generation and detection of phase-locked pulses with spectral content spanning the entire THz range, and even into the mid-infrared [120]. Such large bandwidths are crucial, in particular, when determining the coupling between fundamental excitations and evaluating their role in the development of emergent phenomena. This requires a spectral bandwidth typically spanning not only the low-energy region in the vicinity of 1 THz, but also continuing upwards to the several 10s of THz as we have suggested is required in the study of transport in disordered semiconductors. Few-cycle femtosecond pulse lasers are now commercially available, and so the largest difficulty in attaining these high bandwidths is removed. We therefore see the proliferation of ultrabroadband THz spectroscopy as a natural step for scientific applications, with new techniques such as generation and detection in a dispersionless air plasma potentially replacing the use of ultrathin crystals or exotic organic crystals [360].

From a technological standpoint, there are now more than half a dozen companies worldwide that build and sell pulsed and continuous wave THz spectroscopy systems commercially. Customers are mainly research and government labs but also a few private companies. Yet, the market remains small as THz spectroscopy systems are still rather

costly, predominantly due to the high price of femtosecond lasers. Data-acquisition speeds still need to be further increased, in particular, if THz images are required. It is also safe to assume that the price of femtosecond lasers will further decrease in the future. This will of course increase the market potential of pulsed THz spectrometers.

Another prediction that is safe to assume is that the speed of the imaging process will further increase, which will benefit many of the applications discussed in chapter six. Consequently, THz spectroscopy will become an established technique in the field of nondestructive testing. With the increasing speed we will see first real industrial applications. Produced items will be inspected at line or even inline. Most likely the first industry that will make use of THz imaging is the plastics industry.

Another secure prediction is that future commercial THz systems will be all fiber-coupled, eliminating as many free-space parts behind the laser as possible, including the optical delay line. Such a system has recently been demonstrated [361]. It may even be that the delay line will become completely obsolete. THz spectroscopy without a delay line was demonstrated in 2005 independently by Yasui et al. [362] and Janke et al. [363]. They used two femtosecond lasers that are linked with a fixed repetition rate difference in order to perform high-speed asynchronous optical sampling (ASOPS). A related technique that relies on only one laser was recently demonstrated by Hochrein and coworkers [364]. This is based on the cross-correlation of an optical pulse with a subsequent pulse from the same laser. Temporal delay between these two pulses is achieved by varying the repetition rate of the laser. Consequently, the technique was termed 'optical sampling by laser cavity tuning'. Yet, the work described in [364] still relied on a mechanical delay stage positioned inside the laser cavity to tune the cavity length. In can be foreseen that it will not be long until lasers will be used of which the repetition rate can be tuned all-electronically. This would result in THz spectroscopy systems that use only one laser and operate without any mechanical delay stages.

A further reliable forecast is to assume that THz quasi-time-domain spectroscopy (THz-QTDS) [344] will boost the industrial operation of THz systems. In this scheme the costly femtosecond laser in a THz spectrometer is replaced by a multimode semiconductor laser that costs only a few Euros. Hence, the cost level of the entire THz system drops tremendously. Nevertheless, signals that are similar to those in a THz-TDS setup are observed and all data-extraction schemes developed for THz-TDS can be applied. The first system reported exhibits a bandwidth of only 600 GHz. Yet, this is sufficient for many of the THz-TDS application scenarios discussed in Sect. 6. In particular, it is conceivable that such systems will be applied to monitor polymeric compounding processes or to monitor the moisture and thickness of paper during its production. Over the entire length of the paper web three to five emitter-detector-units are needed. If one turns to THz-QTDS one could have three to five completely independent systems and still hold a price level that is affordable for small and medium enterprises.

Peter Uhd Jepsen received the M. Sc. in Physics and Chemistry in 1994 from Odense University, Denmark and the Ph. D. degree in Natural Sciences from Århus University, Denmark in 1996. He was at the University of Freiburg, Germany from 1996 to 2004, working with terahertz time-domain spectroscopy. From 2005 he was Associate Professor at the Technical University of Denmark (DTU), and since 2008 Professor for Terahertz Science and Technology and Head of the Terahertz Technologies and Biophotonics group at DTU. In 2008 he was Guest Professor at Osaka University. His research areas include photonics-based THz technology, broadband spectroscopy, ultrafast lasers, and time-resolved THz spectroscopy.

David G. Cooke received his B. Sc. Honours in Physics at St. Francis Xavier University, Antigonish, NS, Canada in 2001, and Ph. D. in Physics in 2006 from the University of Alberta, Edmonton, AB, Canada. He went on to do a postdoc in the group of Peter Uhd Jepsen at the Technical University of Denmark in 2007 and became Assistant Professor at DTU in 2008 and Associate Professor in 2009. He will join the Dept. of Physics at McGill University as an Assistant Professor in 2011. His research interests are in ultrafast terahertz spectroscopy of semiconductors and their nanostructures and the development of new measurement techniques and devices at THz frequencies.

Martin Koch received his Ph. D. degree in Marburg in 1995 with a thesis in the field of ultrafast spectroscopy of semiconductors. From 1995 to 1996 he was a postdoc in the Advanced Photonics Research Department at Bell Laboratories/Lucent Technologies in Holmdel, NJ. From 1996 to 1998 he worked as a scientific assistant in the Photonics and Optoelectronics group at the University of Munich, Germany. From 1998 to 2008 he was associate professor for terahertz systems technology at the electrical

engineering department of the Technical University Braunschweig, Germany. Since 2009 he is full professor in semiconductor physics at the physics department of the Philipps University Marburg, Germany.

References

[1] B. E. Cole, J. B. Williams, B. T. King, M. S. Sherwin, and C. R. Stanley, Nature **410**, 60 (2001).

[2] R. Huber, F. Tauser, A. Brodschelm, M. Bichler, G. Abstreiter, and A. Leitenstorfer, Nature **414**, 286 (2001).

[3] I. H. Libon, S. Baumgartner, M. Hempel, N. E. Hecker, J. Feldmann, M. Koch, and P. Dawson, Appl. Phys. Lett. **76**, 2821 (2000).

[4] S. Chatterjee, T. Grunwald, D. Köhler, K. Pierz, D. Golde, M. Kira, and S. W. Koch, Phys. Stat. Sol. C **6**, 453 (2009).

[5] D. G. Cooke, A. N. MacDonald, A. Hryciw, J. Wang, Q. Li, A. Meldrum, and F. A. Hegmann, Phys. Rev. B **73**, 193311 (2006).

[6] R. H. M. Groeneveld and D. Grischkowsky, J. Opt. Soc. Am. B **11**, 2502 (1994).

[7] R. A. Kaindl, M. A. Carnahan, D. Hagele, R. Lovenich, and D. S. Chemla, Nature **423**, 734 (2003).

[8] S. Leinß, T. Kampfrath, K. v. Volkmann, M. Wolf, J. T. Steiner, M. Kira, S. W. Koch, A. Leitenstorfer, and R. Huber, Phys. Rev. Lett. **101**, 246401 (2008).

[9] J. R. Danielson, Y.-S. Lee, J. P. Prineas, J. T. Steiner, M. Kira, and S. W. Koch, Phys. Rev. Lett. **99** 237401 (2007).

[10] M. C. Beard, G. M. Turner, and C. A. Schmuttenmaer, J. Phys. Chem. A **106**, 878 (2002).

[11] M. Schall, M. Walther, and P. U. Jepsen, Phys. Rev. B **64** 094301 (2001).

[12] M. Walther, B. M. Fischer, and P. U. Jepsen, Chem. Phys. **288**, 261 (2003).

[13] D. G. Allis, A. M. Fedor, T. M. Korter, J. E. Bjarnason, and E. R. Brown, Chem. Phys. Lett. **440**, 203 (2007).

[14] T. M. Korter and D. F. Plusquellic, Chem. Phys. Lett. **385**, 45 (2004).

[15] H. Zhang, K. Siegrist, D. F. Plusquellic, and S. K. Gregurick, J. Am. Chem. Soc. **130**, 17846 (2008).

[16] C. Rønne, L. Thrane, P. O. Åstrand, A. Wallqvist, K. V. Mikkelsen, and S. R. Keiding, J. Chem. Phys. **107**, 5319 (1997).

[17] T. Arikawa, M. Nagai, and K. Tanaka, Chem. Phys. Lett. **457**, 12 (2008).

[18] M. Nagai, H. Yada, T. Arikawa, and K. Tanaka, Int. J. Infrared Millim. Waves **27**, 505 (2006).

[19] S. E. Whitmire, D. Wolpert, A. G. Markelz, J. R. Hillebrecht, J. Galan, and R. R. Birge, Biophys. J. **85**, 1269 (2003).

[20] Y. F. He, P. I. Ku, J. R. Knab, J. Y. Chen, and A. G. Markelz, Phys. Rev. Lett. **101** 178103 (2008).

[21] A. G. Markelz, J. R. Knab, J. Y. Chen, and Y. F. He, Chem. Phys. Lett. **442**, 413 (2007).

[22] R. Kersting, G. Strasser, and K. Unterrainer, Electron. Lett. **36**, 1156 (2000).

[23] T. Kleine-Ostmann, P. Dawson, K. Pierz, G. Hein, and M. Koch, Appl. Phys. Lett. **84**, 3555 (2004).

[24] T. Kleine-Ostmann, K. Pierz, G. Hein, P. Dawson, and M. Koch, Electron. Lett. **40**, 124 (2004).

[25] C.-F. Hsieh, R.-P. Pan, T.-T. Tang, H.-L. Chen, and C.-L. Pan, Opt. Lett. **31**, 1112 (2006).

[26] R. Wilk, N. Vieweg, O. Kopschinski, and M. Koch, Opt. Express **17**, 7377 (2009).

[27] C. Winnewisser, F. Lewen, and H. Helm, Appl. Phys. A **66**, 593 (1998).

[28] M. Bozzi, L. Perregrini, J. Weinzierl, and C. Winnewisser, Opt. Eng. **39**, 2263 (2000).

[29] D. Turchinovich, A. Kammoun, P. Knobloch, T. Dobbertin, and M. Koch, Appl. Phys. A, Mater. Sci. Process. **74**, 291 (2002).

[30] W. Withayachumnankul, B. M. Fischer, and D. Abbott, Opt. Commun. **281**, 2374 (2008).

[31] S.-Z. A. Lo and T. E. Murphy, Opt. Lett. **34**, 2921 (2009).

[32] C. Jansen, S. Wietzke, V. Astley, D. M. Mittleman, and M. Koch, Appl. Phys. Lett. **96**, 111108 (2010).

[33] G. Gallot, S. P. Jamison, R. W. McGowan, and D. Grischkowsky, J. Opt. Soc. Am. B **17**, 851 (2000).

[34] Z. Jian, J. Pearce, and D. M. Mittleman, Semicond. Sci. Technol. **20**, S300 (2005).

[35] G. Diwa, A. Quema, E. Estacio, R. Pobre, H. Murakami, S. Ono, and N. Sarukura, Appl. Phys. Lett. **87**, 151114 (2005).

[36] K. Nielsen, H. K. Rasmussen, A. J. Adam, P. C. Planken, O. Bang, and P. U. Jepsen, Opt. Express **17**, 8592 (2009).

[37] C. Jördens, K. L. Chee, I. A. I. Al-Naib, I. Pupeza, S. Peik, G. Wenke, and M. Koch, J. Infrared Milli. Terahz. Waves **31**, 214 (2010).

[38] Z. P. Jian, J. Pearce, and D. M. Mittleman, Opt. Lett. **29**, 2067 (2004).

[39] Y. G. Zhao and D. R. Grischkowsky, IEEE Trans. Microw. Theory Tech. **55**, 656 (2007).

[40] E. Özbay, A. Abeyta, G. Tuttle, M. Tringides, R. Biswas, C. T. Chan, C. M. Soukoulis, and K. M. Ho, Phys. Rev. B **50**, 1945 (1994).

[41] A. Chelnokov, S. Rowson, J.-M. Lourtioz, L. Duvillaret, and J.-L. Coutaz, Electron. Lett. **33**, 1981 (1997).

[42] M. C. Wanke, O. Lehmann, K. Müller, Q. Wen, and M. Stuke, Science **275**, 1284 (1997).

[43] W. J. Padilla, A. J. Taylor, C. Highstrete, M. Lee, and R. D. Averitt, Phys. Rev. Lett. **96**, 107401 (2006).

[44] R. Singh, E. Smirnova, A. J. Taylor, J. F. O'Hara, and W. Zhang, Opt. Express **16**, 6537 (2008).

[45] E. V. Loewenstein, Appl. Opt. **5**, 845 (1966).

[46] K. D. M. Moeller and W. G. Rothschild, Far-infrared Spectroscopy (Wiley Interscience, New York, 1971).

[47] M. van Exter, C. Fattinger, and D. Grischkowsky, Opt. Lett. **14**, 1128 (1989).

[48] J. D. Kafka, M. L. Watts, and J. W. J. Pieterse, IEEE J. Quantum Electron. **28**, 2151 (1992).

[49] E. R. Brown, K. A. McIntosh, F. W. Smith, K. B. Nichols, M. J. Manfra, C. L. Dennis, and J. P. Mattia, Appl. Phys. Lett. **64**, 3311 (1994).

[50] S. Matsuura, M. Tani, and K. Sakai, Appl. Phys. Lett. **70**, 559 (1997).

[51] S. Verghese, K. A. McIntosh, S. Calawa, W. F. Dinatale, E. K. Duerr, and K. A. Molvar, Appl. Phys. Lett. **73**, 3824 (1998).

[52] I. S. Gregory, W. R. Tribe, C. Baker, B. E. Cole, M. J. Evans, L. Spencer, M. Pepper, and M. Missous, Appl. Phys. Lett. **86**, 204104 (2005).

[53] M. Breede, S. Hoffmann, J. Zimmermann, J. Struckmeier, M. Hofmann, T. Kleine-Ostmann, P. Knobloch, M. Koch, J. Meyn, M. Matus, S. W. Koch, and J. V. Moloney, Opt. Commun. **207**, 261 (2002).

[54] K. J. Siebert, H. Quast, R. Leonhardt, T. Löffler, T. Thomson, T. Bauer, H. G. Roskos, and S. Czasch, Appl. Phys. Lett. **80**, 3003 (2002).

[55] R. Wilk, A. Klehr, M. Mikulics, T. Hasek, M. Walther, and M. Koch, Electron. Lett. **43**, 108 (2007).

[56] M. Hyodo, M. Tani, S. Matsuura, N. Onodera, and K. Sakai, Electron. Lett. **32**, 1589 (1996).

[57] T. Kleine-Ostmann, P. Knobloch, M. Koch, S. Hoffmann, M. Breede, M. Hofmann, G. Hein, K. Pierz, M. Sperling, and K. Donhuijsen, Electron. Lett. **37**, 1461 (2001).

[58] R. Wilk, F. Breitfeld, M. Mikulics, and M. Koch, Appl. Opt. **47**, 3023 (2008).

[59] O. Morikawa, M. Tonouchi, and M. Hangyo, Appl. Phys. Lett. **76**, 1519 (2000).

[60] O. Morikawa, M. Tonouchi, and M. Hangyo, Appl. Phys. Lett. **75**, 3772 (1999).

[61] M. Tani, S. Matsuura, K. Sakai, and M. Hangyo, IEEE Microw. Guided Wave Lett. **7**, 282 (1997).

[62] M. Scheller and M. Koch, Opt. Express **17**, 17723 (2009).

[63] J. D. Jackson, Classical electrodynamics (John Wiley & Sons, New York, 1998).

[64] P. U. Jepsen, R. H. Jacobsen, and S. R. Keiding, J. Opt. Soc. Am. B **13**, 2424 (1996).

[65] S. E. Ralph and D. Grischkowsky, Appl. Phys. Lett. **59**, 1972 (1991).

[66] J. E. Pedersen, V. G. Lyssenko, J. M. Hvam, P. U. Jepsen, S. R. Keiding, C. B. Sorensen, and P. E. Lindelof, Appl. Phys. Lett. **62**, 1265 (1993).

[67] E. Castro-Camus, J. Lloyd-Hughes, and M. B. Johnston, Phys. Rev. B **71**, 195301 (2005).

[68] P. C. Upadhya, W. H. Fan, A. Burnett, J. Cunningham, A. G. Davies, E. H. Linfield, J. Lloyd-Hughes, E. Castro-Camus, M. B. Johnston, and H. Beere, Opt. Lett. **32**, 2297 (2007).

[69] M. Tani, S. Matsuura, and K. Sakai, J. Comm. Res. Lab. **43**, 151 (1996).

[70] K. Ezdi, B. Heinen, C. Jördens, N. Vieweg, N. Krumbholz, R. Wilk, M. Mikulics, and M. Koch, J. Eur. Opt. Soc., Rapid Pub. **4**, 09001 (2009).

[71] F. Miyamaru, Y. Saito, K. Yamamoto, T. Furuya, S. Nishizawa, and M. Tani, Appl. Phys. Lett. **96**, 211104 (2010).

[72] M. Ashida, Jpn. J. Appl. Phys. **47**, 8221 (2008).

[73] P. R. Smith, D. H. Auston, and M. C. Nuss, IEEE J. Quantum Electron. **24**, 255 (1988).

[74] A. C. Warren, J. M. Woodall, J. L. Freeouf, D. Grischkowsky, D. T. McInturff, M. R. Melloch, and N. Otsuka, Appl. Phys. Lett. **57**, 1331 (1990).

[75] S. Gupta, M. Y. Frankel, J. A. Valdmanis, J. F. Whitaker, G. A. Mourou, F. W. Smith, and A. R. Calawa, Appl. Phys. Lett. **59**, 3276 (1991).

[76] S. Gupta, J. F. Whitaker, and G. A. Mourou, IEEE J. Quantum Electron. **28**, 2464 (1992).

[77] I. S. Gregory, C. Baker, W. R. Tribe, M. J. Evans, H. E. Beere, E. H. Linfield, A. G. Davies, and M. Missous, Appl. Phys. Lett. **83**, 4199 (2003).

[78] J. Sigmund, C. Sydlo, H. L. Hartnagel, N. Benker, H. Fuess, F. Rutz, T. Kleine-Ostmann, and M. Koch, Appl. Phys. Lett. **87**, 252103 (2005).

[79] C. Baker, I. S. Gregory, W. R. Tribe, I. V. Bradley, M. J. Evans, E. H. Linfield, and M. Missous, Appl. Phys. Lett. **85**, 4965 (2004).

[80] R. Wilk, M. Mikulics, K. Biermann, H. Künzel, I. Z. Kozma, R. Holzwarth, B. Sartorius, M. Mei, and M. Koch, Conference on Lasers and Electro-Optics 2007, Baltimore, MA, USA, Technical Digest **1–5**, 1271 (2007).

[81] B. Sartorius, H. Roehle, H. Kunzel, J. Böttcher, M. Schlak, D. Stanze, H. Venghaus, and M. Schell, Opt. Express **16**, 9565 (2008).

[82] H. Roehle, R. J. B. Dietz, H. J. Hensel, J. Böttcher, H. Künzel, D. Stanze, M. Schell, and B. Sartorius, Opt. Express **18**, 2296 (2010).

[83] M. Suzuki and M. Tonouchi, Appl. Phys. Lett. **86**, 163504 (2005).

[84] M. Suzuki and M. Tonouchi, Appl. Phys. Lett. **86**, 051104 (2005).

[85] N. Chimot, J. Mangeney, L. Joulaud, P. Crozat, H. Bernas, K. Blary, and J. F. Lampin, Appl. Phys. Lett. **87**, 193510 (2005).

[86] M. Ashida, R. Akai, H. Shimosato, I. Katayama, T. Itoh, K. Miyamoto, and H. Ito, Conference on Lasers and Electro-Optics, San Jose 2008, Technical Digest **1–9**, 1734 (2008).

[87] T. A. Liu, M. Tani, M. Nakajima, M. Hangyo, and C. L. Pan, Appl. Phys. Lett. **83**, 1322 (2003).

[88] E. R. Brown, F. W. Smith, and K. A. McIntosh, J. Appl. Phys. **73**, 1480 (1993).

[89] E. R. Brown, Appl. Phys. Lett. **75**, 769 (1999).

[90] S. M. Duffy, S. Verghese, K. A. McIntosh, A. Jackson, A. C. Gossard, and S. Matsuura, IEEE Trans. Microw. Theory Tech. **49**, 1032 (2001).

[91] K. A. McIntosh, E. R. Brown, K. B. Nichols, O. B. McMahon, W. F. DiNatale, and T. M. Lyszczarz, Appl. Phys. Lett. **69**, 3632 (1996).

[92] I. S. Gregory, W. R. Tribe, B. E. Cole, M. J. Evans, E. H. Linfield, A. G. Davies, and M. Missous, Appl. Phys. Lett. **85**, 1622 (2004).

[93] S. Matsuura, G. A. Blake, R. A. Wyss, J. C. Pearson, C. Kadow, A. W. Jackson, and A. C. Gossard, Appl. Phys. Lett. **74**, 2872 (1999).

[94] J. W. Shi, S. W. Chu, M. C. Tien, C. K. Sun, Y. J. Chiu, and J. E. Bowers, Appl. Phys. Lett. **81**, 5108 (2002).

[95] H. Ito, F. Nakajima, T. Furuta, K. Yoshino, Y. Hirota, and T. Ishibashi, Electron. Lett. **39**, 1828 (2003).

[96] H. Ito, S. Kodama, Y. Muramoto, T. Furuta, T. Nagatsuma, and T. Ishibashi, IEEE J. Sel. Top. Quantum Electron. **10**, 709 (2004).

[97] H. Ito, F. Nakajima, T. Furuta, and T. Ishibashi, Semicond. Sci. Technol. **20**, S191 (2005).

[98] F. Nakajima, T. Furuta, and H. Ito, Electron. Lett. **40**, 1297 (2004).

[99] G. H. Döhler, F. Renner, O. Klar, M. Eckardt, A. Schwanhausser, S. Malzer, D. Driscoll, M. Hanson, A. C. Gossard, G. Loata, T. Löffler, and H. Roskos, Semicond. Sci. Technol. **20**, S178 (2005).

[100] S. Preu, F. H. Renner, S. Malzer, G. H. Döhler, L. J. Wang, M. Hanson, A. C. Gossard, T. L. J. Wilkinson, and E. R. Brown, Appl. Phys. Lett. **90**, 212115 (2007).

[101] I. S. Gregory, W. R. Tribe, M. J. Evans, T. D. Drysdale, D. R. S. Cumming, and M. Missous, Appl. Phys. Lett. **87**, 034106 (2005).

[102] P. Chen, G. A. Blake, M. C. Gaidis, E. R. Brown, K. A. McIntosh, S. Y. Chou, M. I. Nathan, and F. Wiliamson, Appl. Phys. Lett. **71**, 1601 (1997).

[103] F. Siebe, K. Siebert, R. Leonhardt, and H. G. Roskos, IEEE J. Quantum Electron. **35**, 1731 (1999).

[104] D. W. Faries, K. A. Gehring, P. L. Richards, and Y. R. Sheen, Phys. Rev. **180**, 363 (1969).

[105] D. W. Faries, P. L. Richards, Y. R. Shen, and K. H. Yang, Phys. Rev. A **3**, 2148 (1971).

[106] K. H. Yang, P. L. Richards, and Y. R. Shen, Appl. Phys. Lett. **19**, 320 (1971).

[107] L. Xu, X. C. Zhang, and D. H. Auston, Appl. Phys. Lett. **61**, 1784 (1992).

[108] A. Rice, Y. Jin, X. F. Ma, X. C. Zhang, D. Bliss, J. Larkin, and M. Alexander, Appl. Phys. Lett. **64**, 1324 (1994).

[109] Q. Wu and X. C. Zhang, Appl. Phys. Lett. **67**, 3523 (1995).

[110] P. U. Jepsen, C. Winnewisser, M. Schall, V. Schyja, S. R. Keiding, and H. Helm, Phys. Rev. E **53**, R3052 (1996).

[111] A. Nahata, D. H. Auston, T. F. Heinz, and C. J. Wu, Appl. Phys. Lett. **68**, 150 (1996).

[112] Q. Wu and X. C. Zhang, Appl. Phys. Lett. **68**, 1604 (1996).

[113] Q. Wu and X. C. Zhang, IEEE J. Sel. Top. Quantum Electron. **2**, 693 (1996).

[114] G. Gallot, J. Q. Zhang, R. W. McGowan, T. I. Jeon, and D. Grischkowsky, Appl. Phys. Lett. **74**, 3450 (1999).

[115] M. Schall, M. Walther, and P. U. Jepsen, Phys. Rev. B **64**, 094301 (2001).

[116] M. Schall and P. U. Jepsen, Appl. Phys. Lett. **77**, 2801 (2000).

[117] Q. Wu and X. C. Zhang, Appl. Phys. Lett. **70**, 1784 (1997).

[118] P. Y. Han and X. C. Zhang, Appl. Phys. Lett. **73**, 3049 (1998).

[119] R. Huber, A. Brodschelm, F. Tauser, and A. Leitenstorfer, Appl. Phys. Lett. **76**, 3191 (2000).

[120] C. Kübler, R. Huber, S. Tubel, and A. Leitenstorfer, Appl. Phys. Lett. **85**, 3360 (2004).

[121] R. W. Boyd, Nonlinear Optics (Academic Press, Amsterdam, 2008).

[122] H. J. Bakker, G. C. Cho, H. Kurz, Q. Wu, and X. C. Zhang, J. Opt. Soc. Am. B **15**, 1795 (1998).

[123] A. Leitenstorfer, S. Hunsche, J. Shah, M. C. Nuss, and W. H. Knox, Appl. Phys. Lett. **74**, 1516 (1999).

[124] G. Gallot and D. Grischkowsky, J. Opt. Soc. Am. B **16**, 1204 (1999).

[125] R. A. Kaindl, F. Eickemeyer, M. Woerner, and T. Elsaesser, Appl. Phys. Lett. **75**, 1060 (1999).

[126] A. Nahata, A. S. Weling, and T. F. Heinz, Appl. Phys. Lett. **69**, 2321 (1996).

[127] M. Jewariya, M. Nagai, and K. Tanaka, J. Opt. Soc. Am. B **26**, A101 (2009).

[128] M. Nagai, M. Jewariya, Y. Ichikawa, H. Ohtake, T. Sugiura, Y. Uehara, and K. Tanaka, Opt. Express **17**, 11543 (2009).

[129] K. L. Yeh, M. C. Hoffmann, J. Hebling, and K. A. Nelson, Appl. Phys. Lett. **90**, 171121 (2007).

[130] D. J. Cook and R. M. Hochstrasser, Opt. Lett. **25**, 1210 (2000).

[131] T. Löffler, F. Jacob, and H. G. Roskos, Appl. Phys. Lett. **77**, 453 (2000).

[132] J. Dai, X. Xie, and X. C. Zhang, Phys. Rev. Lett. **97** (2006).

[133] A. Sengupta, A. Bandyopadhyay, B. F. Bowden, J. A. Harrington, and J. F. Federici, Electron. Lett. **42**, 1477 (2006).

[134] J. M. Dai, J. Q. Zhang, W. L. Zhang, and D. Grischkowsky, J. Opt. Soc. Am. B **21**, 1379 (2004).

[135] C. Fattinger and D. Grischkowsky, Appl. Phys. Lett. **53**, 1480 (1988).

[136] C. Fattinger and D. Grischkowsky, Appl. Phys. Lett. **54**, 490 (1989).

[137] P. U. Jepsen and S. R. Keiding, Opt. Lett. **20**, 807 (1995).

[138] J. Van Rudd and D. M. Mittleman, J. Opt. Soc. Am. B **19**, 319 (2002).

[139] M. T. Reiten, S. A. Harmon, and R. A. Cheville, J. Opt. Soc. Am. B **20**, 2215 (2003).

[140] M. T. Reiten and R. A. Cheville, Opt. Lett. **30**, 673 (2005).

[141] Y. H. Lo and R. Leonhardt, Opt. Express **16**, 15991 (2008).

[142] D. Grischkowsky, S. Keiding, M. van Exter, and C. Fattinger, J. Opt. Soc. Am. B **7**, 2006 (1990).

[143] B. M. Fischer, M. Walther, and P. U. Jepsen, Phys. Med. Biol. **47**, 3807 (2002).

[144] P. U. Jepsen and B. M. Fischer, Opt. Lett. **30**, 29 (2005).

[145] L. Thrane, R. H. Jacobsen, P. U. Jepsen, and S. R. Keiding, Chem. Phys. Lett. **240**, 330 (1995).

[146] J. T. Kindt and C. A. Schmuttenmaer, J. Phys. Chem. **100**, 10373 (1996).

[147] H. Kitahara, T. Yagi, K. Mano, M. W. Takeda, S. Kojima, and S. Nishizawa, J. Korean Phys. Soc. **46**, 82 (2005).

[148] P. U. Jepsen, U. Møller, and H. Merbold, Opt. Express **15**, 14717 (2007).

[149] U. Møller, D. G. Cooke, K. Tanaka, and P. U. Jepsen, J. Opt. Soc. Am. B **26**, A113 (2009).

[150] L. Duvillaret, F. Garet, and J. L. Coutaz, IEEE J. Sel. Top. Quantum Electron. **2**, 739 (1996).

[151] L. Duvillaret, F. Garet, and J. L. Coutaz, Appl. Optics **38**, 409 (1999).

[152] L. Duvillaret, F. Garet, and J. L. Coutaz, J. Opt. Soc. Am. B **17**, 452 (2000).

[153] I. Pupeza, R. Wilk, and M. Koch, Opt. Express **15**, 4335 (2007).

[154] M. Scheller, C. Jansen, and M. Koch, Opt. Commun. **282**, 1304 (2009).

[155] W. Withayachumnankul, B. M. Fischer, and D. Abbott, Opt. Express **16**, 7382 (2008).

[156] M. Franz, B. M. Fischer, and M. Walther, Appl. Phys. Lett. **92**, 021107 (2008).

[157] C. Raman, Proc. Math. Sci. **29**, 381 (1949).

[158] T. I. Jeon and D. Grischkowsky, Appl. Phys. Lett. **72**, 3032 (1998).

[159] S. E. Ralph, S. Perkowitz, N. Katzenellenbogen, and D. Grischkowsky, J. Opt. Soc. Am. B **11**, 2528 (1994).

[160] H. Hirori, K. Yamashita, M. Nagai, and K. Tanaka, Jpn. J. Appl. Phys. 2, Lett. (Japan) **43**, L1287 (2004).

[161] U. Møller, Ph. D. Thesis, Technical University of Denmark, Kongens Lyngby (2009), p. 179.

[162] H. Hirori, M. Nagai, and K. Tanaka, Opt. Express **13**, 10801 (2005).

[163] H. Yada, M. Nagai, and K. Tanaka, Chem. Phys. Lett. **473**, 279 (2009).

[164] H. Yada, M. Nagai, and K. Tanaka, Chem. Phys. Lett. **464**, 166 (2008).

[165] T. Arikawa, M. Nagai, and K. Tanaka, Chem. Phys. Lett. **477**, 95 (2009).

[166] M. C. Nuss, D. H. Auston, and F. Capasso, Phys. Rev. Lett. **58**, 2355 (1987).

[167] C. A. Schmuttenmaer, Chem. Rev. **104**, 1759 (2004).

[168] M. C. Beard, G. M. Turner, and C. A. Schmuttenmaer, Phys. Rev. B **62**, 15764 (2000).

[169] M. C. Beard, G. M. Turner, and C. A. Schmuttenmaer, J. Appl. Phys. **90**, 5915 (2001).

[170] K. P. H. Lui and F. A. Hegmann, J. Appl. Phys. **93**, 9012 (2003).

[171] E. Hendry, M. Koeberg, J. Pijpers, and M. Bonn, Phys. Rev. B **75**, 233202 (2007).

[172] D. G. Cooke, F. A. Hegmann, E. C. Young, and T. Tiedje, Appl. Phys. Lett. **89**, 122103 (2006).

[173] M. Schall and P. U. Jepsen, Opt. Lett. **25**, 13 (2000).

[174] M. C. Beard, G. M. Turner, and C. A. Schmuttenmaer, Nano Lett. **2**, 983 (2002).

[175] G. M. Turner, M. C. Beard, and C. A. Schmuttenmaer, J. Phys. Chem. B **106**, 11716 (2002).

[176] R. P. Prasankumar, A. Scopatz, D. J. Hilton, A. J. Taylor, R. D. Averitt, J. M. Zide, and A. C. Gossard, Appl. Phys. Lett. **86**, 201107 (2005).

[177] J. B. Baxter and C. A. Schmuttenmaer, J. Phys. Chem. B **110**, 25229 (2006).

[178] D. G. Cooke, A. N. MacDonald, A. Hryciw, A. Meldrum, J. Wang, Q. Li, and F. A. Hegmann, J. Mater. Sci., Mater. Electron. **18**, S447 (2007).

[179] P. Parkinson, J. Lloyd-Hughes, Q. Gao, H. H. Tan, C. Jagadish, M. B. Johnston, and L. M. Herz, Nano Lett. **7**, 2162 (2007).

[180] M. C. Beard, J. L. Blackburn, and M. J. Heben, Nano Lett. **8**, 4238 (2008).

[181] D. G. Cooke, F. A. Hegmann, Y. I. Mazur, Z. M. Wang, W. Black, H. Wen, G. J. Salamo, T. D. Mishima, G. D. Lian, and M. B. Johnson, J. Appl. Phys. **103**, 023710 (2008).

[182] J. H. Strait, P. A. George, M. Levendorf, M. Blood-Forsythe, F. Rana, and J. Park, Nano Lett. **9**, 2967 (2009).

[183] H. Němec, P. Kužel, F. Kadlec, D. Fattakhova-Rohlfing, J. Szeifert, T. Bein, V. Kalousek, and J. Rathousky, Appl. Phys. Lett. **96**, 062103 (2010).

[184] R. A. Kaindl, D. Hägele, M. A. Carnahan, and D. S. Chemla, Phys. Rev. B **79**, 045320 (2009).

[185] J. Shan, F. Wang, E. Knoesel, M. Bonn, and T. F. Heinz, Phys. Rev. Lett. **90**, 247401 (2003).

[186] F. A. Hegmann, R. R. Tykwinski, K. P. H. Lui, J. E. Bullock, and J. E. Anthony, Phys. Rev. Lett. **89**, 227403 (2002).

[187] O. Ostroverkhova, D. G. Cooke, F. A. Hegmann, J. E. Anthony, V. Podzorov, M. E. Gershenson, O. D. Jurchescu, and T. T. M. Palstra, Appl. Phys. Lett. **88**, 162101 (2006).

[188] O. Ostroverkhova, D. G. Cooke, F. A. Hegmann, R. R. Tykwinski, S. R. Parkin, and J. E. Anthony, Appl. Phys. Lett. **89**, 192113 (2006).

[189] O. Ostroverkhova, D. G. Cooke, S. Shcherbyna, R. F. Egerton, F. A. Hegmann, R. R. Tykwinski, and J. E. Anthony, Phys. Rev. B **71**, 035204 (2005).

[190] O. Ostroverkhova, S. Shcherbyna, D. G. Cooke, R. F. Egerton, F. A. Hegmann, R. R. Tykwinski, S. R. Parkin, and J. E. Anthony, J. Appl. Phys. **98**, 033701 (2005).

[191] E. Hendry, J. M. Schins, L. P. Candeias, L. D. A. Siebbeles, and M. Bonn, Phys. Rev. Lett. **92**, 196601 (2004).

[192] P. D. Cunningham and L. M. Hayden, J. Phys. Chem. C **112**, 7928 (2008).

[193] H. Němec, H. K. Nienhuys, F. Zhang, O. Inganäs, A. Yartsev, and V. Sundström, J. Phys. Chem. C **112**, 6558 (2008).

[194] P. D. Cunningham, L. M. Hayden, H.-L. Yip, and A. K. Y. Jen, J. Phys. Chem. B **113**, 15427 (2009).

[195] E. Hendry, M. Koeberg, J. M. Schins, L. D. A. Siebbeles, and M. Bonn, Chem. Phys. Lett. **432**, 441 (2006).

[196] O. Esenturk, R. J. Kline, D. M. Deongchamp, and E. J. Heilweil, J. Phys. Chem. C **112**, 10587 (2008).

[197] T. Kampfrath, L. Perfetti, F. Schapper, C. Frischkorn, and M. Wolf, Phys. Rev. Lett. **95**, 187403 (2005).

[198] J. F. Federici, B. I. Greene, P. N. Saeta, D. R. Dykaar, F. Sharifi, and R. C. Dynes, Phys. Rev. B **46**, 11153 (1992).

[199] R. D. Averitt and A. J. Taylor, J. Phys., Condens. Matter **14**, R1357 (2002).

[200] C. Kübler, H. Ehrke, R. Huber, R. Lopez, A. Halabica, R. F. Haglund, Jr., and A. Leitenstorfer, Phys. Rev. Lett. **99**, 116401 (2007).

[201] H. Němec and F. Kadlec, and P. Kužel, J. Chem. Phys. **117**, 8454 (2002).

[202] G. L. Dakovski, B. Kubera, S. Lan, and J. Shan, J. Opt. Soc. Am. B **23**, 139 (2006).

[203] D. Golde, M. Wagner, D. Stehr, H. Schneider, M. Helm, A. M. Andrews, T. Roch, G. Strasser, M. Kira, and S. W. Koch, Phys. Rev. Lett. **102**, 127403 (2009).

[204] K. Iwaszczuk, D. G. Cooke, M. Fujiwara, H. Hashimoto, and P. Uhd Jepsen, Opt. Express **17**, 21969 (2009).

[205] K. Y. Kim, B. Yellampalle, J. H. Glownia, A. J. Taylor, and G. Rodriguez, Phys. Rev. Lett. **100**, 135002 (2008).

[206] R. E. Glover and M. Tinkham, Phys. Rev. **108**, 243 (1957).

[207] P. N. Saeta, J. F. Federici, B. I. Greene, and D. R. Dykaar, Appl. Phys. Lett. **60**, 1477 (1992).

[208] M. C. Beard and C. A. Schmuttenmaer, J. Chem. Phys. **114**, 2903 (2001).

[209] D. Côté, J. E. Sipe, and H. M. van Driel, J. Opt. Soc. Am. B **20**, 1374 (2003).

[210] M. C. Hoffmann and D. Turchinovich, Appl. Phys. Lett. **96**, 151110 (2010).

[211] L. Razzari, F. H. Su, G. Sharma, F. Blanchard, A. Ayesheshim, H.-C. Bandulet, R. Morandotti, J.-C. Kieffer, T. Ozaki, M. Reid, and F. A. Hegmann, Phys. Rev. B **79**, 193204 (2009).

[212] F. H. Su, F. Blanchard, G. Sharma, L. Razzari, A. Ayesheshim, T. L. Cocker, L. V. Titova, T. Ozaki, J.-C. Kieffer, R. Morandotti, M. Reid, and F. A. Hegmann, Opt. Express **17**, 9620 (2009).

[213] J. Hebling, M. C. Hoffmann, H. Y. Hwang, K.-L. Yeh, and K. A. Nelson, Phys. Rev. B **81**, 035201 (2010).

[214] M. Walther, B. Fischer, M. Schall, H. Helm, and P. U. Jepsen, Chem. Phys. Lett. **332**, 389 (2000).

[215] P. U. Jepsen and S. J. Clark, Chem. Phys. Lett. **442**, 275 (2007).

[216] D. Mittleman, (ed.), Sensing with terahertz radiation (Springer-Verlag, Berlin, 2003).

[217] S. J. Clark, M. D. Segall, C. J. Pickard, P. J. Hasnip, M. J. Probert, K. Refson, and M. C. Payne, Z. Kristallogr. **220**, 567 (2005).

[218] M. D. Segall, P. J. D. Lindan, M. J. Probert, C. J. Pickard, P. J. Hasnip, S. J. Clark, and M. C. Payne, J. Phys., Condens. Matter **14**, 2717 (2002).

[219] Guassian program, Gaussian, Inc.

[220] K. Siegrist, C. R. Bucher, I. Mandelbaum, A. R. H. Walker, R. Balu, S. K. Gregurick, and D. F. Plusquellic, J. Am. Chem. Soc. **128**, 5764 (2006).

[221] D. G. Allis, D. A. Prokhorova, and T. M. Korter, J. Phys. Chem. A **110**, 1951 (2006).

[222] D. G. Allis and T. M. Korter, Chem. Phys. Chem. **7**, 2398 (2006).

[223] D. G. Allis, J. A. Zeitler, P. F. Taday, and T. M. Korter, Chem. Phys. Lett. **463**, 84 (2008).

[224] J. Wilkinson, C. T. Konek, J. S. Moran, E. M. Witko, and T. M. Korter, Chem. Phys. Lett. **478**, 172 (2009).

[225] D. G. Allis, P. M. Hakey, and T. M. Korter, Chem. Phys. Lett. **463**, 353 (2008).

[226] P. M. Hakey, D. G. Allis, W. Ouellette, and T. M. Korter, J. Phys. Chem. A **113**, 5119 (2009).

[227] P. M. Hakey, D. G. Allis, M. R. Hudson, W. Ouellette, and T. M. Korter, Chem. Phys. Chem. **10**, 2434 (2009).

[228] P. M. Hakey, M. R. Hudson, D. G. Allis, W. Ouellette, and T. M. Korter, J. Phys. Chem. A **113**, 13013 (2009).

[229] T. M. Korter, R. Balu, M. B. Campbell, M. C. Beard, S. K. Gregurick, and E. J. Heilweil, Chem. Phys. Lett. **418**, 65 (2006).

[230] M. D. King, P. M. Hakey, and T. M. Korter, J. Phys. Chem. A **114**, 2945 (2010).

[231] P. M. Hakey, D. G. Allis, M. R. Hudson, W. Ouellette, and T. M. Korter, J. Phys. Chem. A **114**, 4364 (2010).

[232] S. Saito, T. M. Inerbaev, H. Mizuseki, N. Igarashi, and Y. Kawazoe, Jpn. J. Appl. Phys. 1, Regul. Pap. Short Notes Rev. Pap. **45**, 4170 (2006).

[233] S. Saito, T. M. Inerbaev, H. Mizuseki, N. Igarashi, R. Note, and Y. Kawazoe, Chem. Phys. Lett. **432**, 157 (2006).

[234] S. Saito, T. M. Inerbaev, H. Mizuseki, N. Igarashi, R. Note, and Y. Kawazoe, Jpn. J. Appl. Phys. 2, Lett. (Japan) **45**, L1156 (2006).

[235] S. Saito, T. M. Inerbaev, H. Mizuseki, N. Igarashi, R. Note, and Y. Kawazoe, Chem. Phys. Lett. **423**, 439 (2006).

[236] T. Hamanaka, M. Kakudo, T. Ashida, and T. Mitsui, Acta Crystallogr. Sect. B Struc. Crystallogr. Cryst. Chem. B **28**, 214 (1972).

[237] C. J. Simmons, R. S. H. Liu, M. Denny, and K. Seff, Acta Crystallogr. Sect. B, Struct. Commun. **37**, 2197 (1981).

[238] C. J. Simmons, A. E. Asato, M. Denny, and R. S. H. Liu, Acta Crystallogr. Sect. C, Cryst. Struct. Commun. **42**, 1558 (1986).

[239] F. L. Gervasio, G. Cardini, P. R. Salvi, and V. Schettino, J. Phys. Chem. A **102**, 2131 (1998).

[240] G. M. Brown and H. A. Levy, Acta Crystallogr. Sect. B, Struct. Commun. B **29**, 790 (1973).

[241] L. Duvillaret, F. Garet, and J.-L. Coutaz, IEEE J. Sel. Top. Quantum Electron. **2**, 739 (1996).

[242] N. Laman, S. S. Harsha, D. Grischkowsky, and J. S. Melinger, Opt. Express **16**, 4094 (2008).

[243] A. Bingham and D. Grischkowsky, Conference on Lasers and Electro-Optics, Baltimore 2005, Technical Digest **1–3**, 2281 (2005).

[244] A. L. Bingham and D. Grischkowsky, Opt. Lett. **33**, 348 (2008).

[245] P. A. George, C. Manolatou, F. Rana, A. L. Bingham, and D. R. Grischkowsky, Appl. Phys. Lett. **91**, 191122 (2007).

[246] S. S. Harsha, N. Laman, and D. Grischkowsky, Appl. Phys. Lett. **94**, 091118 (2009).

[247] R. Mendis and D. Grischkowsky, Opt. Lett. **26**, 846 (2001).

[248] R. Mendis, V. Astley, J. B. Liu, and D. M. Mittleman, Appl. Phys. Lett. **95**, 171113 (2009).

[249] R. Mendis and D. M. Mittleman, Opt. Express **17**, 14839 (2009).

[250] H. Zhan, R. Mendis, and D. M. Mittleman, Opt. Express **18**, 9643 (2010).

[251] J. S. Melinger, N. Laman, S. S. Harsha, and D. Grischkowsky, Appl. Phys. Lett. **89**, 251110 (2006).

[252] J. S. Melinger, N. Laman, S. S. Harsha, S. Cheng, and D. Grischkowsky, J. Phys. Chem. A **111**, 10977 (2007).

[253] J. S. Melinger, N. Laman, S. S. Harsha, S. Cheng, and D. Grischkowsky, J. Phys. Chem. A **111**, 10977 (2007).

[254] N. Laman, S. S. Harsha, D. Grischkowsky, and J. S. Melinger, Biophys. J. **94**, 1010 (2008).

[255] J. S. Melinger, N. Laman, and D. Grischkowsky, Appl. Phys. Lett. **93**, 011102 (2008).

[256] S. S. Harsha and D. Grischkowsky, J. Phys. Chem. A **114**, 3489 (2010).

[257] D. G. Cooke and P. U. Jepsen, Phys. Status Solidi A **206**, 997 (2009).

[258] D. G. Cooke and P. U. Jepsen, Appl. Phys. Lett. **94**, 241118 (2009).

[259] J. E. Pedersen and S. R. Keiding, IEEE J. Quantum Electron. **28**, 2518 (1992).

[260] B. N. Flanders, R. A. Cheville, D. Grischkowsky, and N. F. Scherer, J. Phys. Chem. **100**, 11824 (1996).

[261] S. R. Keiding, J. Phys. Chem. A **101**, 5250 (1997).

[262] R. Jimenez, G. R. Fleming, P. V. Kumar, and M. Maroncelli, Nature **369**, 471 (1994).

[263] M. Maroncelli, J. Chem. Phys. **94**, 2084 (1991).

[264] R. Balu, H. Zhang, E. Zukowski, J. Y. Chen, A. G. Markelz, and S. K. Gregurick, Biophys. J. **94**, 3217 (2008).

[265] J. Y. Chen, J. R. Knab, J. Cerne, and A. G. Markelz, Phys. Rev. E **72**, 040901 (2005).

[266] M. Heyden, E. Brundermann, U. Heugen, G. Niehues, D. M. Leitner, and M. Havenith, J. Am. Chem. Soc. **130**, 5773 (2008).

[267] A. G. Markelz, IEEE J. Sel. Top. Quantum Electron. **14**, 180 (2008).

[268] A. G. Markelz, A. Roitberg, and E. J. Heilweil, Chem. Phys. Lett. **320**, 42 (2000).

[269] B. Born, H. Weingartner, E. Brundermann, and M. Havenith, J. Am. Chem. Soc. **131**, 3752 (2009).

[270] S. Ebbinghaus, S. J. Kim, M. Heyden, X. Yu, M. Gruebele, D. M. Leitner, and M. Havenith, J. Am. Chem. Soc. **130**, 2374 (2008).

[271] U. Heugen, G. Schwaab, E. Brundermann, M. Heyden, X. Yu, D. M. Leitner, and M. Havenith, Proc. Natl. Acad. Sci. USA **103**, 12301 (2006).

[272] S. J. Kim, B. Born, M. Havenith, and M. Gruebele, Angew. Chem. Int. Ed. **47**, 6486 (2008).

[273] T. Sato and R. Buchner, J. Phys. Chem. A **108**, 5007 (2004).

[274] C. Rønne, P. O. Astrand, and S. R. Keiding, Phys. Rev. Lett. **82**, 2888 (1999).

[275] D. A. Yarotski, R. D. Averitt, N. Negre, S. A. Crooker, A. J. Taylor, G. P. Donati, A. Stintz, L. F. Lester, and K. J. Malloy, J. Opt. Soc. Am. B **19**, 1480 (2002).

[276] D. Turchinovich, K. Pierz, and P. U. Jepsen, Phys. Status Solidi C **0**, 1556 (2003).

[277] D. G. Cooke, F. A. Hegmann, Y. I. Mazur, W. Q. Ma, X. Wang, Z. M. Wang, G. J. Salamo, M. Xiao, T. D. Mishima, and M. B. Johnson, Appl. Phys. Lett. **85**, 3839 (2004).

[278] A. K. Azad, R. P. Prasankumar, D. Talbayev, A. J. Taylor, R. D. Averitt, J. M. O. Zide, H. Lu, A. C. Gossard, and J. F. O'Hara, Appl. Phys. Lett. **93**, 121108 (2008).

[279] H. P. Porte, P. U. Jepsen, N. Daghestani, E. U. Rafailov, and D. Turchinovich, Appl. Phys. Lett. **94**, 262104 (2009).

[280] D. Stehr, C. M. Morris, D. Talbayev, M. Wagner, H. C. Kim, A. J. Taylor, H. Schneider, P. M. Petroff, and M. S. Sherwin, Appl. Phys. Lett. **95**, 251105 (2009).

[281] P. Parkinson, H. J. Joyce, Q. Gao, H. H. Tan, X. Zhang, J. Zou, C. Jagadish, L. M. Herz, and M. B. Johnston, Nano Lett. **9**, 3349 (2009).

[282] T. Müller, W. Parz, K. Unterrainer, S. Sauvage, J. Houel, P. Boucaud, and A. Miard, and A. Lemaître, Phys. Rev. B **77**, 035314 (2008).

[283] F. Wang, J. Shan, M. A. Islam, I. P. Herman, M. Bonn, and T. F. Heinz, Nature Mater. **5**, 861 (2006).

[284] E. Hendry, M. Koeberg, F. Wang, H. Zhang, C. D. Donega, D. Vanmaekelbergh, and M. Bonn, Phys. Rev. Lett. **96**, 057408 (2006).

[285] M. C. Beard, G. M. Turner, J. E. Murphy, O. I. Micic, M. C. Hanna, A. J. Nozik, and C. A. Schmuttenmaer, Nano Lett. **3**, 1695 (2003).

[286] N. V. Smith, Phys. Rev. B **64**, 155106 (2001).

[287] H. Němec, P. Kužel, and V. Sundström, Phys. Rev. B **79**, 115309 (2009).

[288] P. U. Jepsen, B. M. Fischer, A. Thoman, H. Helm, J. Y. Suh, R. Lopez, and R. F. Haglund, Phys. Rev. B **74**, 205103 (2006).

[289] H. Zhan, V. Astley, M. Hvasta, J. A. Deibel, D. M. Mittleman, and Y.-S. Lim, Appl. Phys. Lett. **91**, 162110 (2007).

[290] B. B. Hu and M. C. Nuss, Opt. Lett. **20**, 1716 (1995).

[291] S. Hunsche, M. Koch, I. Brener, and M. C. Nuss, Opt. Commun. **150**, 22 (1998).

[292] Q. Chen, Z. Jiang, G. X. Xu, and X.-C. Zhang, Opt. Lett. **25**, 1122 (2000).

[293] J. F. Federici, O. Mitrofanov, M. Lee, J. W. P. Hsu, I. Brener, R. Harel, J. D. Wynn, L. N. Pfeiffer, and K. W. West, Phys. Med. Biol. **47**, 3727 (2002).

[294] H. T. Chen, R. Kersting, and G. C. Cho, Appl. Phys. Lett. **83**, 3009 (2003).

[295] J. R. Knab, J. L. Adam, M. Nagel, E. Shaner, M. A. Seo, D. S. Kim, and P. C. M. Planken, Opt. Express **17**, 15072 (2009).

[296] D. M. Mittleman, S. Hunsche, L. Boivin, and M. C. Nuss, Opt. Lett. **22**, 904 (1997).

[297] M. Brucherseifer, P. Haring Bolivar, H. Klingenberg, and H. Kurz, Appl. Phys. B: Lasers Opt. **72**, 361 (2001).

[298] B. Ferguson and X.-C. Zhang, Nat. Mater. **1**, 26 (2002).

[299] T. Yasuda, T. Yasui, T. Araki, and E. Abraham, Opt. Commun. **267**, 128 (2006).

[300] N. C. J. Van, der Valk, W. A. M. Van, der Marel, and P. C. M. Planken, Opt. Lett. **30**, 2802 (2005).

[301] F. Rutz, T. Hasek, M. Koch, H. Richter, and U. Ewert, Appl. Phys. Lett. **89**, 221911 (2006).

[302] C. Jördens, M. Scheller, M. Wichmann, M. Mikulics, K. Wiesauer, and M. Koch, Appl. Opt. **48**, 2037 (2009).

[303] C. Jördens, M. Scheller, S. Wietzke, D. Romeike, C. Jansen, T. Zentgraf, K. Wiesauer, V. Reisecker, and M. Koch, Compos. Sci. Technol. **70**, 472 (2010).

[304] T. Löffler, T. Bauer, K. J. Siebert, H. Roskos, A. Fitzgerald, and S. Czasch, Opt. Express **9**, 616 (2001).

[305] W. L. Chan, K. Charan, D. Takhar, K. F. Kelly, R. G. Baraniuk, and D. Mittleman, (eds.), Appl. Phys. Lett. **93**, 121105 (2008).

[306] T. Buma and T. B. Norris, Appl. Phys. Lett. **84**, 2196 (2004).

[307] J. Xu and X.-C. Zhang, Appl. Phys. Lett. **88**, 151107 (2006).

[308] J. L. Johnson, T. D. Dorney, and D. M. Mittleman, IEEE J. Sel. Top. Quantum Electron. **7**, 592 (2001).

[309] W. L. Chan, J. Deibel, and D. M. Mittleman, Rep. Prog. Phys. **70**, 1325 (2007).

[310] D. Mittleman, R. H. Jacobsen, and M. C. Nuss, IEEE J. Sel. Top. Quantum Electron. **2**, 679 (1996).

[311] D. Mittleman, M. Gupta, R. Neelamani, R. G. Baraniuk, J. V. Rudd, and M. Koch, Appl. Phys. B **68**, 1085 (1999).

[312] V. P. Wallace, A. J. Fitzgerald, S. Shankar, N. Flanagan, R. Pye, J. Cluff, and D. D. Arnone, Br. J. Dermatol. **151**, 424 (2004).

[313] E. Pickwell and V. P. Wallace, J. Phys. D, Appl. Phys. **39**, R301 (2006).

[314] D. M. Mittleman, J. Cunningham, M. C. Nuss, and M. Geva, Appl. Phys. Lett. **71** (1997).

[315] M. Herrmann, M. Tani, and K. Sakai, J. Appl. Phys. **91**, 1247 (2002).

[316] C. Jördens, M. Scheller, B. Breitenstein, D. Selmar, and M. Koch, J. Biol. Phys **35**, 255 (2009).

[317] M. Koch, S. Hunsche, P. Schumacher, M. C. Nuss, J. Feldmann, and J. Fromm, Wood Sci. Technol. **32**, 421 (1998).

[318] M. Herrmann, M. Tani, K. Sakai, and M. Watanabe, in: 2002 IEEE Tenth International Conference on Terahertz Electronics, Cambridge, UK, Technical Digest (2002), p. 28.

[319] B. Pradarutti, R. Mueller, W. Freese, G. Matthaeus, S. Riehemann, G. Notni, S. Nolte, and A. Tuennermann, Opt. Express **16**, 18443 (2008).

[320] D. Zimdars, G. Fichter, C. Megdanoff, J. Duquette, M. Murdock, I. Duling, J. White, and S. Williamson, in: Proceedings of the Conference on Lasers and Electro-Optics, San Jose 2010, Technical Digest (2010), p. CWO1.

[321] B. Pradarutti, R. Mueller, G. Matthaeus, C. Brueckner, S. Riehemann, G. Notni, S. Nolte, and A. Tuennermann, Opt. Express **15**, 17652 (2007).

[322] T. Yasui, K.-i. Sawanaka, A. Ihara, E. Abraham, M. Hashimoto, and T. Araki, Opt. Express **16**, 1208 (2008).

[323] Q. Wu, T. D. Hewitt, and X.-C. Zhang, Appl. Phys. Lett. **69**, 1026 (1996).

[324] K. Kawase, Y. Ogawa, Y. Watanabe, and H. Inoue, Opt. Express **11**, 2549 (2003).

[325] N. Karpowicz, H. Zhong, C. Zhang, K.-I. Lin, J.-S. Hwang, J. Xu, and X.-C. Zhang, Appl. Phys. Lett. **86**, 054105 (2005).

[326] D. Zimdars, J. S. White, G. Stuk, A. Chernovsky, G. Fichter, and S. Williamson, Insight **48**, 537 (2006).

[327] K. Baaske, M. Salhi, F. Rutz, T. Hasek, R. Wilk, H. Richter, and M. Koch, Terahertz for Military and Security Applications IV, in: Proceedings of the International Society for Optical Engineering Conference, San Diego 2006, Vol. 6212, edited by D. L. Woolard, R. J. Hwu, M. J. Rosker, and J. O. Jensen.

[328] H. Hoshina, Y. Sasaki, A. Hayashi, C. Otani, and K. Kawase, Appl. Spectrosc. **63**, 81–86 (2009).

[329] Y. C. Shen, T. Lo, P. F. Taday, B. E. Cole, W. R. Tribe, and M. C. Kemp, Appl. Phys. Lett. **86**, 241116 (2005).

[330] H.-B. Liu, Y. Chen, G. J. Bastiaans, and X.-C. Zhang, Opt. Express **14**, 415 (2006).

[331] C. Jördens and M. Koch, Opt. Eng. **47**, 037003 (2008).

[332] M. Herrmann, M. Tani, M. Watanabe, and K. Sakai, IEEE Proc. Optoelectron. **149**, 116 (2002).

[333] S. Wietzke, C. Jansen, F. Rutz, D. M. Mittleman, and M. Koch, Polym. Testing **26**, 614 (2007).

[334] N. Krumbholz, T. Hochrein, N. Vieweg, T. Hasek, K. Kretschmer, M. Bastian, M. Mikulics, and M. Koch, Polym. Testing **28**, 30 (2009).

[335] S. Wietzke, C. Jördens, N. Krumbholz, M. Koch, B. Baudrit, and M. Bastian, J. Eur. Opt. Soc. Rapid Public. **2**, 07013 (2007).

[336] C. Jansen, S. Wietzke, O. Peters, M. Scheller, N. Vieweg, M. Salhi, N. Krumbholz, C. Jördens, T. Hochrein, and M. Koch, Appl. Opt. **49**, E48 (2010).

[337] C. Jördens, S. Wietzke, M. Scheller, and M. Koch, Polym. Testing **29**, 209 (2010).

[338] F. Rutz, M. Koch, S. Khare, M. Moneke, H. Richter, and U. Ewert, Int. J. Infrared Millim. Waves **27**, 547 (2006).

[339] S. Wietzke, C. Jansen, T. Jung, M. Reuter, B. Baudrit, M. Bastian, S. Chatterjee, and M. Koch, Opt. Express **17**, 19006 (2009).

[340] M. Scheller, S. Wietzke, C. Jansen, and M. Koch, J. Phys. D, Appl. Phys. **42**, 065415 (2009).

[341] J. D. Menczel and R. B. Prime, Thermal analysis of polymers: fundamentals and applications (Wiley, Hoboken, 2009).

[342] D. Banerjee, W. v. Spiegel, M. D. Thomson, S. Schabel, and H. G. Roskos, Opt. Express **16**, 9060 (2008).

[343] P. Mousavi, F. Haran, D. Jez, F. Santosa, and J. S. Dodge, Appl. Opt. **48**, 6541 (2009).

[344] M. Scheller and M. Koch, Opt. Express **17**, 17723 (2009).

[345] P. F. Taday, Philos. Trans. R. Soc. Lond. A, Math. Phys. Eng. Sci. **362**, 351 (2004).

[346] P. F. Taday, I. V. Bradley, D. D. Arnone, and M. Pepper, J. Pharma. Sci. **92**, 831 (2003).

[347] J. A. Zeitler, K. Kogermann, J. Rantanen, T. Rades, P. F. Taday, M. Pepper, J. Aaltonen, and C. J. Strachan, Int. J. Pharm. **334**, 78 (2007).

[348] A. J. Fitzgerald, B. E. Cole, and P. F. Taday, J. Pharma. Sci. **94**, 177 (2004).

[349] J. A. Spencer, Z. Gao, T. Moore, L. F. Buhse, P. F. Taday, D. A. Newnham, Y. Shen, A. Portieri, and A. Husain, J. Pharma. Sci. **97**, 1543 (2008).

[350] W. Köhler, M. Panzner, U. Klotzbach, E. Beyer, S. Winnerl, M. Helm, F. Rutz, C. Jördens, M. Koch, and H. Leitner, Proceedings of the European Conference of Non-Destructive Testing, Berlin 2006, Technical Digest.

[351] K. Fukunaga and Y. Ogawa, S. i. Hayashi, and I. Hosako, IEICE Electron. Exp. **4**, 258 (2007).

[352] K. Fukunaga and Y. Ogawa, S. i. Hayashi, and I. Hosako, IEICE Electron. Exp. **5**, 223 (2008).

[353] J. B. Jackson, M. Mourou, J. F. Whitaker, I. N. Duling, S. L. Williamson, M. Menu, and G. A. Mourou, Opt. Commun. **281**, 527 (2008).

[354] A. J. L. Adam, P. C. M. Planken, S. Meloni, and J. Dik, Opt. Express **17**, 3407 (2009).

[355] A. Sell, A. Leitenstorfer, and R. Huber, Opt. Lett. **33**, 2767 (2008).

[356] F. Blanchard, L. Razzari, H.-C. Bandulet, G. Sharma, R. Morandotti, J.-C. Kieffer, T. Ozaki, M. Reid, H. F. Tiedje, H. K. Haugen, and F. A. Hegmann, Opt. Express **15**, 13212 (2007).

[357] K. Reimann, R. P. Smith, A. M. Weiner, T. Elsaesser, and M. Woerner, Opt. Lett. **28**, 471 (2003).

[358] G. Gunter, A. A. Anappara, J. Hees, A. Sell, G. Biasiol, L. Sorba, S. De Liberato, C. Ciuti, A. Tredicucci, A. Leitenstorfer, and R. Huber, Nature **458**, 178 (2009).

[359] I. Katayama, H. Aoki, J. Takeda, H. Shimosato, M. Ashida, R. Kinjo, I. Kawayama, M. Tonouchi, M. Nagai, and K. Tanaka, in: Proceedings of the Conference on Lasers and Electro-Optics, San Jose 2010.

[360] N. Karpowicz, X. F. Lu, and X. C. Zhang, J. Mod. Opt. **56**, 1137 (2009).

[361] N. Krumbholz, C. Jansen, M. Scheller, T. Müller-Wirts, S. Lübbecke, R. Holzwarth, R. Scheunemann, B. Sartorius, H. Roehle, D. Stanze, J. Beckmann, L. v. Chrzanowski, U. Ewert, and M. Koch, Millimetre Wave and Terahertz Sensors and Technology II, edited by K. A. Krapels and N. A. Salmon, in: Proceedings of the SPIE Security & Defense Berlin, 2009, Vol. 7485.

[362] T. Yasui, E. Saneyoshi, and T. Araki, Appl. Phys. Lett. **87**, 061101 (2005).

[363] C. Janke, M. Foerst, M. Nagel, H. Kurz, and A. Bartels, Opt. Lett. **30**, 1405 (2005).

[364] T. Hochrein, R. Wilk, M. Mei, R. Holzwarth, N. Krumbholz, and M. Koch, Opt. Express **18**, 1613 (2010).